

Section 3: Fracture and Damage Mechanics

Piezoelectric BEM for Fracture Analysis: Comparison of Crack Surface Electric Boundary Conditions

M. Denda and M. Mansukh

Rutgers University, Mech. & Aero. Engng. Dept.

Piscataway, NJ 08854-8058, U.S.A.

denda@rutgers.edu and mansukh@rutgers.edu

Keywords: Piezoelectric Fracture Analysis, Boundary Element Method, Crack Surface Electric Boundary Conditions, Singular Crack Element

Abstract. A comparison of the crack surface electric boundary conditions is made for the impermeable, permeable and semi-permeable cracks. Although the exact electric induction intensity factor (EIF) is given by the semi-permeable crack, its solution requires a nonlinear iterative procedure. An alternative, less complicated and linear, approach is proposed using the boundary element method (BEM) designed for the impermeable and permeable crack solutions, to get the upper and lower bounds for the EIFs for multiple piezoelectric cracks. The numerical Green's function for the multiple piezoelectric cracks is developed by the analytical integration of the continuous distribution of the generalized dislocation dipoles. The Green's function has the $1/\sqrt{r}$ generalized stress singularity and the generalized stress intensity factors are determined directly in the main processing, along with the unknown boundary displacements and tractions.

Introduction

The coupling of mechanical and electrical behaviors of the piezoelectric materials has found its applications to sensors (e.g., sonars), actuators (e.g., ultrasonic cleaners, ultra-precision positioners, ink jet print heads), signal transmitters (e.g., cellular phone, remote car opener), and surface acoustic wave devices to mention a few. The modern life style cannot be sustained without piezoelectric materials. However, they are plagued with the brittleness of the widely used piezoceramic materials. The lack of understanding and modelling tools of the piezoelectric fracture is limiting the further progress in the piezoelectric material based technology. This paper addresses issues on the crack surface electric boundary conditions and suggests the upper and lower bounds approach in the determination of the electric induction intensity factors using the boundary element method (BEM).

While the mechanical boundary condition (BC) on the crack surface is always traction-free, the electric boundary condition comes in different degrees of shielding the electric induction defined by the electric permeability. For a crack along the x_1 -axis, the permeable BC,

$$D_2^+ = D_2^-; \quad \Phi^+ - \Phi^- = 0, \quad (1)$$

does not shield the electric induction at all, where D_2 and Φ are the electric induction and the electric potential, respectively, with \pm indicating the upper and lower crack surfaces. Meanwhile, the impermeable BC,

$$D_2^+ = D_2^- = 0, \quad (2)$$

shields the electric induction completely. The permeable BC is correct if the crack is closed, while the impermeable BC is correct if the permittivity ε_c of the crack medium is zero. Since no medium has zero permittivity (the vacuum has the least permittivity $\varepsilon_0 = 8.854 \times 10^{-12} C/(Vm)$) and we consider open cracks, the both boundary conditions are not correct. Hao and Shen [1] proposed the semi-permeable BC,

$$D_2^+ = D_2^-; \quad D_2^+(u_2^+ - u_2^-) = -\varepsilon_c(\Phi^+ - \Phi^-), \quad (3)$$

which is the consistent BC. Note that the semi-permeable BC is reduced to the impermeable BC when $\varepsilon_c = 0$ and to the permeable BC when $u_2^+ - u_2^- = 0$ and that the impermeable and permeable BCs set the bounds for the semi-permeable BC. The majority of the earlier works adopted the impermeable

BC due to the convenience to obtain the analytical solution. This led to contradiction between the experimental results and the fracture prediction by the (negative) energy release rate [2]. Results predicted by the permeable BC are in much better agreement with the experimental results than those by the impermeable BC [3]. If the crack opening displacement is extremely small, the permeable BC may provide a good approximation despite its inconsistency. The shift toward the consistent semi-permeable BC was made gradually but slowly [4, 5].

While the solutions of the permeable and the impermeable cracks are linear, that of the semi-permeable crack is non-linear. Since the distribution of the electric induction on the crack surface, which is needed to determine the crack opening displacement and the electric potential jump across the crack, is unknown we need an iteration process to determine all unknowns. This is inherently a nonlinear process even though each step consists of the linear solver. This poses a serious difficulty for the complex multiple crack configurations that appear in the real life applications. Meanwhile, the analytical solution for the single semi-permeable crack suggests the electric induction intensity factor is bounded by those by impermeable and the permeable cracks. So even though we may not get the exact semi-permeable solution, we can still get the upper and lower bound solutions using the impermeable and permeable cracks.

While the FEM needs to model the entire domain surrounding a crack, the BEM only needs a single line to model the crack. It makes more sense to use the BEM for crack problems. As the demands for the analysis of more complicated crack configurations, such as multiple and curvilinear cracks, arise the advantage of the BEM over the FEM becomes clearly visible. We propose to use the BEM crack modelling strategy using the Green's function approach to multiple crack problems. The crack is modeled by the continuous distribution of the generalized dislocation dipoles with the \sqrt{r} crack tip behavior and the resulting integration is evaluated analytically using the complex variable theory. The resulting crack element, called the whole crack singular element, offers a collection of mutually independent crack opening modes each of which has the $1/\sqrt{r}$ crack tip stress singularity. It serves as the numerical Green's function for the crack since the magnitudes of each mode must be determined numerically to satisfy the crack surface boundary condition.

Piezoelectric Equations, Stroh Formalism and BEM

We consider the piezoelectric solids whose strain (ϵ_{ij}) and electric (E_i) fields in three-dimensions are related to the stress (σ_{kl}) and electric induction (D_k) fields by the equations

$$\epsilon_{ij} = s_{ijkl}\sigma_{kl} + g_{kij}D_k, \quad E_i = -g_{ikl}\sigma_{kl} + \beta_{ik}D_k, \quad (4)$$

where s_{ijkl} , g_{ikl} , β_{ik} are the elastic compliance, piezoelectric, and dielectric impermeability constants, respectively. We define the four dimensional generalized displacement vector by augmenting the electric potential ϕ to the three displacement components u_j . Similarly the generalized force vector is defined by adding the charge as its fourth component. The generalized traction are defined by adding the surface charge to the existing three components of the traction. Also define the generalized strain \mathcal{E}_{Ij} and stress Σ_{Ij} ,

$$\langle \mathcal{E}_{Ij}, \Sigma_{Ij} \rangle = \begin{cases} \langle \epsilon_{ij}, \sigma_{ij} \rangle & (I \equiv i = 1, 2, 3) \\ \langle E_j, D_j \rangle & (I = 4) \end{cases} \quad (5)$$

for $j = 1, 2, 3$. The upper (or lower) case Roman index ranges from 1 to 4 (or 3). The generalized traction T_I is related to the generalized stress by

$$T_I = \Sigma_{Ij}n_j, \quad (6)$$

where n_j is the unit normal component of the surface element.

In this paper we consider the plane piezoelectricity problem where the generalized displacement components depend only on two coordinates x_1 and x_2 . Using the fact that $e_3 = E_3 \equiv 0$ we can eliminate the stress and electric induction components σ_3 and D_3 from (4) to get the reduced generalized strain and stress relations (Denda and Lua [6] and Denda and Araki [7]).

In the generalized Stroh formalism for piezoelectricity the generalized displacement U_I and the stress function Φ_I are given by

$$U_I = 2\Re \sum_{J=1}^4 A_{IJ} f_J(z_K) \quad \text{and} \quad \Phi_I = 2\Re \sum_{J=1}^4 L_{IJ} f_J(z_K), \quad (7)$$

in terms of four functions $f_J(z_J)$ of the generalized complex variables $z_K = x_1 + p_K x_2$ ($K = 1, 2, 3, 4$) defined by the characteristic roots p_K of the problem and matrices A_{IJ} and L_{IJ} (Denda and Lua [6] and Denda and Araki [7]).

Consider the generalized line force in x_I direction at (η_1, η_2) . The resulting generalized displacement component in the x_J direction at (x_1, x_2) is given by

$$G_{JI}(x_1, x_2; \eta_1, \eta_2) = \Im \frac{1}{\pi} \sum_{K=1}^4 A_{JK} A_{IK} \ln(z_K - \xi_K), \quad (8)$$

where \Im is the imaginary part of a complex variable and $\xi_K = \eta_1 + p_K \eta_2$. Note that $I, J = 4$ corresponds to the electric charge. Consider the generalized line dislocation dipole, which is an infinitesimal segment $(d\eta_1, d\eta_2)$ of length ds over which a generalized displacement jump is prescribed. For a generalized line dislocation dipole at (η_1, η_2) in x_I direction the resulting displacement component in x_J direction at (x_1, x_2) is given by

$$G_{JI}^{(d)}(x_1, x_2; \eta_1, \eta_2) ds = -\Im \frac{1}{\pi} \sum_{K=1}^4 A_{JK} L_{IK} \frac{d\xi_K}{z_K - \xi_K}, \quad (9)$$

where $d\xi_K = d\eta_1 + p_K d\eta_2$. The basis of the direct formulation of the BEM is the physical interpretation of the generalized Somigliana's identity according to which distributions of the generalized line forces and line dislocation dipoles on the boundary are used (Denda and Lua [6]). In the BEM implementation the original boundary is approximated by a set of straight lines and the boundary displacement and traction are interpolated by the quadratic polynomial function. All the boundary integrals are evaluated analytically and there is no need to deal with the singular and the hypersingular integrals.

Numerical Green's Function for Piezoelectric Cracks

A crack L in an infinite body is represented by the generalized line dislocation dipole distribution with the magnitude δ_I . Consider a straight crack in the interval $(-1, +1)$ on the horizontal coordinate axis where $\xi_K = \eta_1$ for all values of K ($= 1, 2, 3, 4$) since $\eta_2 = 0$. We represent the generalized crack opening displacement δ_I by the continuous distribution of the generalized line dislocation dipoles

$$\delta_I(\eta_1) = \sqrt{1 - \eta_1^2} \sum_{m=1}^M \delta_I^{(m)} U_{m-1}(\eta_1), \quad (10)$$

where $U_{m-1}(\eta_1)$ is Chebyshev polynomial of the second kind. The resulting generalized displacement is obtained by integrating the product of the Green's function (9) and the distribution (10) analytically with the result

$$u_J^{(d)}(x_1, x_2) = -\Im \sum_{m=1}^M \sum_{K=1}^4 A_{JK} \sum_{I=1}^4 L_{IK} \delta_I^{(m)} R_m(z_K), \quad (11)$$

where

$$R_m(z_K) = \left(z_K - \sqrt{(z_K)^2 - 1} \right)^m \quad (m \geq 1). \quad (12)$$

Similarly, the stress function is given by

$$\phi_J^{(d)}(x_1, x_2) = -\Im \sum_{m=1}^M \sum_{K=1}^4 L_{JK} \sum_{I=1}^4 L_{IK} \delta_I^{(m)} R_m(z_K). \quad (13)$$

When the half-crack length is a , instead of 1, the formulas (11) and (13) still apply if we replace the arguments z_α by the normalized arguments $Z_\alpha = z_\alpha/a$, from which we can calculate the traction on the crack surface

$$(T_J)^\pm(X) = \pm \frac{1}{a} \Im \sum_{m=1}^M \sum_{K=1}^4 L_{JK} \sum_{I=1}^4 L_{IK} \delta_I^{(m)} m U_{m-1}(X) \quad (|X| \leq 1), \quad (14)$$

where $X = x_1/a$ and the superscripts $+$ and $-$ indicate limits from above and below the horizontal coordinate axis, respectively, and the stress intensity factors at $X = \pm 1$,

$$K_J(\pm 1) = \sqrt{\frac{\pi}{a}} \Im \sum_{m=1}^M (\pm)^{m+1} \sum_{K=1}^4 L_{JK} \sum_{I=1}^4 L_{IK} \delta_I^{(m)} m, \quad (15)$$

where $K_I = K_2$, $K_{II} = K_1$, $K_{III} = K_3$ and $K_{IV} = K_4$ are Mode I, II and III stress intensity factors and the electric induction (also defined as Mode IV) intensity factor, respectively. Notice that, for each mode m of the generalized crack opening displacement defined by (10), equations (11) and (13) give the Green's functions for the generalized displacement and stress function components. Both the generalized crack opening displacement and the stress singularity is built in the Green's function. These Green's functions have more flexibility than the traditional Green's functions for zero generalized crack face traction. Instead, given the arbitrary non-zero value of the generalized crack face traction, formula (14) is used to determine the magnitude $\delta_k^{(m)}$ of each Green's function that, when all Green's functions are superposed, produce the given generalized crack face traction value. Once the generalized COD is determined the formula (15) gives the SIFs in terms of $\delta_k^{(m)}$. This scheme can readily be extended to multiple cracks in the finite domain with the introduction of the boundary elements defining the finite demarcation of the domain.

The solution strategies for the impermeable and permeable cracks are summarized as follows. (1) For the impermeable crack all the crack surface generalized traction components are set to zero. (2) For the permeable crack set the electric potential jump $\delta_4^{(m)}$ to zero and solve the problem by only applying the traction zero boundary condition on the crack. Since $\delta_4^{(m)} = 0$ we only need three traction free boundary condition on the crack surface to determine three unknown crack opening displacement components. Both (1) and (2) are linear procedures and can be solved by the BEM for multiple crack problems.

Analytical Solution for the Semi-Permeable BC

Consider a single horizontal crack $(-a, a)$ along the x_1 -axis in an infinite piezoelectric domain with the remote loading $T_I^\infty = \Sigma_{I2}^\infty = (\sigma_{12}^\infty, \sigma_{22}^\infty, \sigma_{32}^\infty, D_2^\infty)$ and the crack surface loading $T_I^c = -\Sigma_{I2}^c = -(0, 0, 0, D_2^c)$. Using the superposition principle, the crack surface traction boundary condition is given by

$$(T_I)^+ = -(\Sigma_{I2}^\infty - \Sigma_{I2}^c), \quad (16)$$

where the left hand side is given by (14). The final solution is obtained by superposing the the solution of the loaded infinite plain without the crack. Using complex variable theory one can show that the generalize crack opening displacement δ_I ($I = 1, 2, 3, 4$) is given by

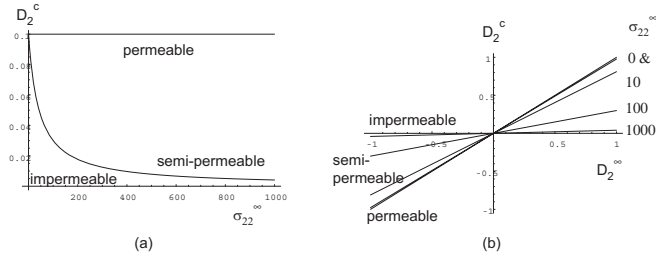
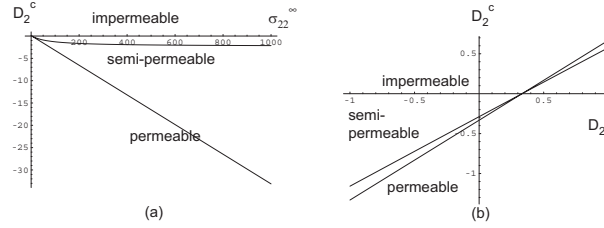
$$\delta_I = H_{IJ} (\Sigma_{J2}^\infty - \Sigma_{J2}^c) \sqrt{a^2 - x_1^2}, \quad (17)$$

where the compliance matrix H_{IJ} is defined by

$$H_{IJ} = -2\Im \left(A_{IK} L_{KJ}^{-1} \right), \quad (18)$$

where L_{KJ}^{-1} is the inverse of L_{KJ} . The values of D_2^c for the three electric boundary conditions are determined as follows. (1) For the impermeable BC, we simply get $D_2^c = 0$. (2) For the permeable BC, we set $\delta_4 = 0$ in (17) to obtain

$$D_2^c = D_2^\infty + \frac{H_{41}\sigma_{12}^\infty + H_{42}\sigma_{22}^\infty + H_{43}\sigma_{32}^\infty}{H_{44}}. \quad (19)$$


 Figure 1: The crack face electric induction D_2^c for BSN with $H_{24} = 0$.

 Figure 2: The crack face electric induction D_2^c for BSN with $H_{24} \neq 0$.

For the semi-permeable BC given by Equation (3) we get

$$D_2^c = -\varepsilon_c \frac{H_{41}\sigma_{12}^\infty + H_{42}\sigma_{22}^\infty + H_{43}\sigma_{32}^\infty + H_{44}(D_2^\infty - D_2^c)}{H_{21}\sigma_{12}^\infty + H_{22}\sigma_{22}^\infty + H_{23}\sigma_{32}^\infty + H_{24}(D_2^\infty - D_2^c)}. \quad (20)$$

Solving for D_2^c we get

$$D_2^c = \frac{\sum_{J=1}^4 H_{2J}\sigma_{2J}^\infty - \varepsilon_c H_{44} \pm \sqrt{(\sum_{J=1}^4 H_{2J}\sigma_{2J}^\infty - \varepsilon_c H_{44})^2 + 4\varepsilon_c H_{24} \sum_{J=1}^4 H_{4J}\sigma_{2J}^\infty}}{2H_{24}}, \quad (21)$$

when $H_{24} \neq 0$ and

$$D_2^c = -\varepsilon_c \frac{\sum_{J=1}^4 H_{4J}\sigma_{2J}^\infty}{\sum_{J=1}^4 H_{2J}\sigma_{2J}^\infty - \varepsilon_c H_{44}}, \quad (22)$$

when $H_{24} = 0$. In (21) we select the branch that gives the positive crack opening displacement δ_2 . Note that H_{24} is the measure of coupling between the crack opening δ_2 and the electric potential jump δ_4 and depends on the material constants.

Numerical Results and Conclusions

For Barium Sodium Niobate (BSN), if we select the coordinate axes x_i to coincide with the crystal axes a_i then $H_{24} = 0$. If we select $x_1 = a_2, x_2 = a_3, x_3 = a_1$, then $H_{24} \neq 0$. For the BSN with $H_{24} = 0$ under the remote loading σ_{22}^∞ and D_2^∞ , Figure 1 shows Variation of D_2^c ($\times 10^{-2} C/m^2$) (a) as the function of σ_{22}^∞ ($\times 10^7 N/m^2$) for fixed $D_2^\infty = 0.1 \times 10^{-2} C/m^2$ and (b) as the function of D_2^∞ for fixed $\sigma_{22}^\infty = (0, 1, 10, 100, 1000) \times 10^7 N/m^2$. Figure 2 shows the corresponding variation for the BSN with $H_{24} \neq 0$. (a) For fixed $D_2^\infty = 0.1 \times 10^{-2} C/m^2$ and (b) For fixed $\sigma_{22}^\infty = 10 \times 10^7 N/m^2$. These figures indicate that the impermeable and the permeable cracks set the bounds for the semi-permeable cracks. At higher and lower limits of the applied stress σ_{22}^∞ , the semi-permeable solution approaches to the impermeable and permeable solutions, respectively, while at the mid level it deviates from both of them.

Even though the impermeable and the permeable cracks are not correct, their upper and the lower bounds property can be exploited in the practical crack analysis if the semi-permeable crack solution is not available. Our objective is to identify these bounds for various multiple crack configurations. By simply specifying a line for each crack, virtually any multiple curvilinear crack configurations can

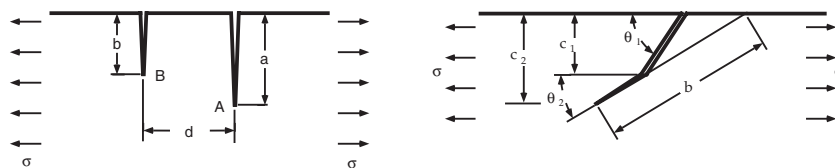


Figure 3: Some multiple/curvilinear crack configurations tested.

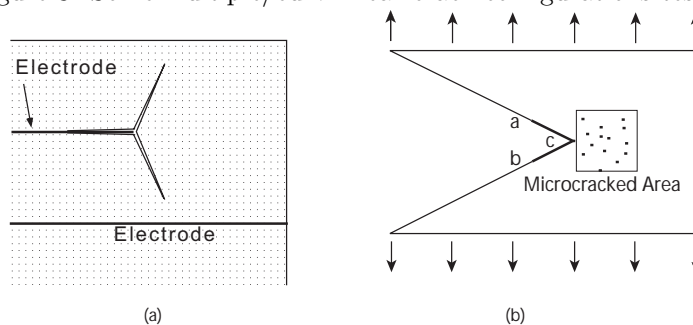


Figure 4: (a) Cracking pattern in the multilayer actuator. (b) Microcracks and a macrocrack interaction.

be analyzed; ranging from simple multiple collinear/parallel straight cracks and cracks in Figure 3 to cracks appearing in the multilayer actuators and a macro and microcracks interaction as shown in Figure 4. Numerical results for these crack configurations will be reported in the BETEQ2004 conference.

Acknowledgment

M. Mansukh was supported by Mechanical and Aerospace Engineering Department, Rutgers University.

References

- [1] T.H. Hao and Z.Y. Shen *Eng. Frac. Mech.*, **47**, 793–802 (1994).
- [2] P.B.Park and C.T. Sun *Int. J. Fract.*, **70**, 203–216 (1995).
- [3] F. Narita, Y. Shindo, and K. Horiguchi *Mechanics of Electromagnetic Material Systems and Structures* (Y. Shindo, editor), 89–101, WIT Press, Southampton (2002).
- [4] B.L. Wang and Y.W. Mai *Int. J. Eng. Sci.*, **41**, 633–652 (2003).
- [5] O. Gruebner, M. Kamlah, and D. Munz *Engng. Frac. Mech.*, **70**, 1399–1413 (2003).
- [6] M. Denda and J. Lua *Composites B*, **30**, 699–707 (1999).
- [7] M. Denda, Y. Araki, and Y. K. Yong *Int. J. Solids Struct.* (accepted).

T-Stress Solutions for a Radial Edge Crack in a Thick-Walled Cylinder by the Boundary Element Method

J. Li, C.L. Tan and X. Wang

Department of Mechanical & Aerospace Engineering
Carleton University, Ottawa, Canada K1S 5B6

Keywords: *T*-stress; Constraint effects; Contour integral.

Abstract

Elastic fracture mechanics analysis using the BEM is performed to determine the *T*-stress solutions for a radial crack in a thick-walled cylinder. The *T*-stress is increasingly being used as an additional parameter to the stress intensity factor for fracture assessment in engineering design. The numerical values are evaluated using Sladek's contour integral approach in the BEM analysis. A wide range of cylinder radius ratios and relative crack lengths is considered and the loading conditions treated include internal pressure loading as well as when the cylinder is subject to a steady-state radial temperature gradient. Results show that such a cracked cylinder under internal pressure loading, in particular, exhibits low crack-tip constraint characteristics. The results obtained will be of practical importance in the high-pressure vessel industry.

1. Introduction

In conventional failure assessment of crack problems using linear elastic fracture mechanics (LEFM), comparison is made of the calculated stress intensity factor with the fracture toughness of the material. The latter is usually measured from 'high constraint' standard test specimens, e.g. deeply cracked three-point bending specimen and compact tension specimen. Over the years, questions have arisen if the fracture toughness measured from these specimens can be applied to cracked structures with 'low constraint' characteristics, i.e. where there is low stress triaxiality in the vicinity of the crack tip. It is increasingly being recognised [1,2,3,4] that to provide a more reliable and accurate fracture assessment in situations where the crack-tip stress constraint is less severe, an additional stress field characterizing parameter to the stress intensity factor needs to be introduced. The additional parameter adopted is commonly referred to as the *T*-stress and it corresponds to the second term of the Williams' [5] eigenfunction series expansion for the stress field in the vicinity of the crack-tip. Bilby *et al* [6] showed that positive *T*-stress increases the level of crack tip stress triaxiality which leads to higher crack tip constraint; negative *T*-stress, conversely, reduces the level of crack tip stress triaxiality and relates to low crack tip constraint. The application of two-parameter failure assessment approach, using *T*-stress together with stress intensity factor, to include the constraint effect in the failure assessment procedure is becoming more well-established in design codes [7].

Failure of thick-walled pressurised cylinders (e.g. gun tubes and pressure vessels) is often due to the presence of internal or external cracks. A long internal single radial crack may be treated as a through-crack in two-dimensions and is commonly seen in such components. Generally, a cracked cylinder can be considered as a "low-constrained" geometry. Availability of accurate *T*-stress solutions for this component will thus provide a more reliable assessment of its failure by fracture. These solutions, to the authors' knowledge, have hitherto not been presented in the open literature.

Recently, Tan and Wang [8] have derived a simple formula to obtain *T*-stress from the computed crack face displacements using BEM; it is analogous to the displacement formula for the stress intensity factor solution in plane problems. It has been subsequently found in a more extensive study [9], however, that the accuracy of the numerical results for the *T*-stress can be relatively sensitive to the mesh discretisation at the crack-tip for some physical problems. Sladek *et al* [10] has also developed a contour integral formula to calculate the *T*-stress; the contour can be somewhat remote from the crack tip, thereby reducing the numerical errors in the near-tip field solution associated with the stress singularity. The aim of this paper is to obtain *T*-stress solutions for a thick-walled cylinder with a radial crack, using the BEM and the contour integral approach of Sladek *et al* [10]. The loading conditions treated include internal pressure as well as when the cylinder is subject to a radial steady state temperature gradient.

2. Contour Integral for T -stress Evaluation

The elastic stresses in the vicinity of a crack-tip under mode I load conditions can be expressed as, Williams [5]

$$\sigma_{ij} = \frac{K_I}{\sqrt{2\pi r}} F_{ij}(\theta) + T_{ij} \delta_{i1} \delta_{j1} + O(\sqrt{r}) \quad (1)$$

where (r, θ) and (x_1, x_2) are the polar and Cartesian coordinates, respectively, with the origin at the crack-tip; and T_{ij} is the T -stress whose magnitude varies only with the load and geometry of the cracked body. The corresponding displacement field, u_i , may be written, for plane strain conditions, as:

$$u_1 = \frac{K_I}{4\mu} \sqrt{\frac{r}{2\pi}} g_1(\theta) + (1-\nu^2) \cdot \frac{T \cdot r}{E} \cos \theta \quad (2a)$$

$$u_2 = \frac{K_I}{4\mu} \sqrt{\frac{r}{2\pi}} g_2(\theta) - \nu(1+\nu) \cdot \frac{T \cdot r}{E} \sin \theta \quad (2b)$$

where μ is the shear modulus, E is the Young's modulus and ν is the Poisson's ratio.

Consider a cracked isotropic, elastic domain R shown in Fig. 1 enclosed by the boundary S . Within this domain, a closed integration path composed of Γ_o , Γ_C^+ and Γ_C^- is considered. Consider next two (primed and unprimed) sets of equilibrium states of the sub-domain. Using Gauss's divergence theorem, Hooke's law and the strain-displacement relations, Betti-Rayleigh's reciprocal work theorem can be written as:

$$\int_{\Gamma} (t_i u_i' - t_i' u_i) \cdot d\Gamma = \int_{\Omega} (X_i u_i' - X_i' u_i) \cdot d\Omega \quad (3)$$

where X_i and X_i' are body forces in the two load states, respectively.

Because of the stress singularity at the crack-tip, a small circular region in its vicinity, of radius ε and bounded by Γ_ε , has to be excluded, as shown in Fig. 1. The contour $\Gamma = \Gamma_o + \Gamma_C^+ + \Gamma_C^- - \Gamma_\varepsilon$ is a closed integration path in the anticlockwise direction. With no loss of generality, assume that in eq.(3), the primed state corresponds to an auxiliary field. The non-primed state corresponds to the unknown field. Assume an auxiliary field where $t_i' = 0$ on the crack faces and body force $X_i' = 0$. For small equilibrium stress loads, it may be assumed that $t_i^+ = t_i^-$. Following the usual limiting process, eq.(3) can be written as:

$$\lim_{\varepsilon \rightarrow 0} \int_{\Gamma_\varepsilon} (t_i' u_i - t_i u_i') \cdot d\Gamma = \int_{\Gamma_o} (t_i' u_i - t_i u_i') \cdot d\Gamma - \int_{\Gamma_C^+} 2t_i^+ u_i' \cdot d\Gamma - \lim_{\varepsilon \rightarrow 0} \int_{\Omega - \Omega_\varepsilon} X_i u_i' \cdot d\Omega \quad (4)$$

Sladek, *et al* [10] suggested that a special auxiliary field be chosen such that eq(4) can be employed to obtain a non-vanishing contribution of the elastic T -stress, and at the same time, eliminate the contribution due to singular term in the integrand which contains the stress intensity factor. The auxiliary field chosen corresponds to that of a static point force, f , applied to the crack tip in the direction parallel to the crack plane (see Fig. 1) and is obtained by differentiating auxiliary field proposed by Kfoury [11], with respect to x_1 . They are as follows:

$$\begin{aligned} u_1'(r, \theta) &= -\frac{f}{\pi E r} (1-\nu^2) \cdot \left(\cos \theta - \frac{1}{1-\nu} \sin^2 \theta \cos \theta \right) \\ u_2'(r, \theta) &= -\frac{f}{2\pi E r} (1+\nu) \cdot (1-2\nu - \cos 2\theta) \cdot (-\sin \theta) \\ \sigma_{11}'(r, \theta) &= \frac{f}{\pi r^2} \cos^2 \theta \cdot (\cos^2 \theta - 3\sin^2 \theta) \\ \sigma_{12}'(r, \theta) &= \frac{f}{\pi r^2} \sin 2\theta \cdot \cos 2\theta \\ \sigma_{22}'(r, \theta) &= \frac{f}{\pi r^2} \sin^2 \theta \cdot (3\cos^2 \theta - \sin^2 \theta) \end{aligned} \quad (5)$$

Substituting the auxiliary field solutions and the singular term of Williams' series expansion into the left hand side of eq. (4), gives a vanishing contribution as:

$$\lim_{\varepsilon \rightarrow 0} \int_{\Gamma_\varepsilon} (t_i' u_i^S - t_i^S u_i') \cdot d\Gamma = 0 \quad (6)$$

where t_i^S and u_i^S are the singular field parameters and they correspond to first terms of eq.(1) and eq.(2), respectively. On the other hand, the substitution of the auxiliary field solution and the second term of Williams series expansion into the left hand side of eq.(4), gives:

$$\lim_{\epsilon \rightarrow 0} \int_{\Gamma_\epsilon} (t_i' u_i^T - t_i^T u_i') \cdot d\Gamma = \frac{1-\nu^2}{E} T \cdot f \tag{7}$$

where t_i^T and u_i^T are the non-singular field parameters which correspond to the second terms of eq.(1) and eq.(2), respectively. By further substituting eq.(6) and eq.(7) into eq.(4), the integral representation of T -stress can finally be derived as follows for zero body forces:

$$T = \frac{E}{f(1-\nu^2)} \int_{\Gamma_o} (t_i' u_i - t_i u_i') \cdot d\Gamma - \frac{2E}{f(1-\nu^2)} \int_{\Gamma_\epsilon} t_i^+ u_i' \cdot d\Gamma \tag{8}$$

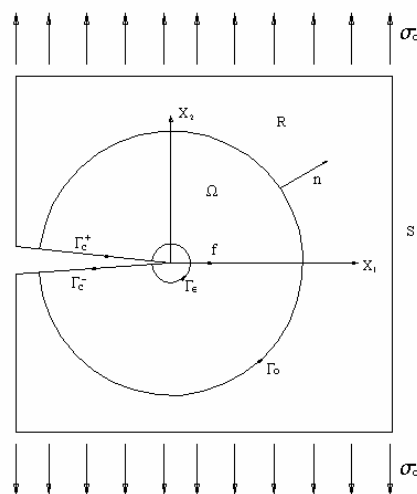


Fig. 1 A cracked elastic domain under mode I loading.

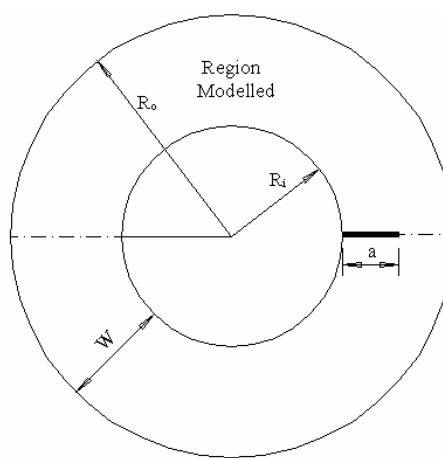


Fig. 2 A thick-walled cylinder with a single edge radial crack

It can be proved that for mode I cracked problems, even with non-zero crack face traction in the x_2 direction, the second integral term of eq.(8) is always zero. So the general contour integral formula for T -stress, in the absence of body force, can then be expressed as:

$$T = \frac{E}{f(1-\nu^2)} \int_{\Gamma_o} (t_i' u_i - t_i u_i') \cdot d\Gamma \tag{9}$$

The integral in eq. (9) can be numerically evaluated by using simple Gaussian quadrature. The corresponding nodal parameters u_i and t_i along the integration path can be obtained from BEM analysis. In this study, the quadratic isoparametric formulation is employed together with the usual quarter-point crack-tip elements. The BEM approach for T -stresses has been validated [9] by comparing the results obtained using the BEM with the exact solutions [12], finite element solutions [3] and Sladek's solutions [10] for an infinite plate and three different test specimens; excellent agreement with discrepancies of less than 2 percent were generally obtained.

3. Numerical Results

Figure 2 shows a thick-walled cylinder with an internal single edge radial crack considered in this study. The geometry of the cracked cylinder is defined by the relative crack length a/W and $k = R_o/R_i$ ratio, where $W = R_o - R_i$; and plane strain end conditions were assumed. The radius ratios investigated were $R_o/R_i = 1.5, 1.75, 2.0, 2.25$ and 2.5 ; and for each of these ratios, a range of relative crack sizes, $a/W = 0.1$ to 0.6 , were treated. The analysis was first carried out for internal uniform pressure loading, p , separately for when it acts on just the circumferential surface and then on just the crack faces. The results will thus be applicable to those cases when the internal fluid pressure does not act on the crack faces (such as when a thin liner is present), and

when it does. Next, results were obtained for the case when there is a steady state radial temperature gradient across the wall thickness.

For the thermal loading, the T -stress was obtained simply by the superposition of two cases. The first was the T -stress for the same cracked component loaded by the crack face pressure $\sigma(x)$, corresponding to the stress field at the prospective crack plane in the un-cracked component due to the thermal gradient. The second case was the T -stress at the crack-tip position in the un-cracked component under the stress field due to the thermal loading. This can be expressed as follows:

$$T_{\text{temperature loading}} = T_{\text{crack face loading}} + T_{\text{uncracked}} \quad (10)$$

The stress field in a plane un-cracked cylinder in plane strain when subject to a radial temperature gradient is given as follows [13]:

$$\begin{aligned} \sigma_{\theta\theta}(x) &= C_o \left[1 - \ln \frac{R_o}{r} - \frac{\ln k}{k^2 - 1} \left(1 + \frac{R_o^2}{r^2} \right) \right] \\ \sigma_{rr}(x) &= C_o \left[-\ln \frac{R_o}{r} - \frac{\ln k}{k^2 - 1} \left(1 - \frac{R_o^2}{r^2} \right) \right] \end{aligned} \quad (11)$$

where $C_o = E \cdot \alpha (T_i - T_o) / [2 \cdot (1 - \nu) \cdot \ln k]$; α is the coefficient of linear expansion; and, T_i and T_o are the temperatures on the inner and outer radii of the cylinder, respectively. The $T_{\text{crack face loading}}$ part is obtained by applying a pressure load corresponding to the above hoop stress distribution at the crack face. The $T_{\text{uncracked}}$ part in eq.(10) can be easily shown to be:

$$T_{\text{uncracked}} = (\sigma_x - \sigma_y) \Big|_{x=a, y=0} = (\sigma_{rr} - \sigma_{\theta\theta}) \Big|_{r=a, \theta=0} = C_o \left[-1 + \frac{2 \cdot \ln k}{k^2 - 1} \cdot \frac{R_o^2}{r^2} \right] \quad (12)$$

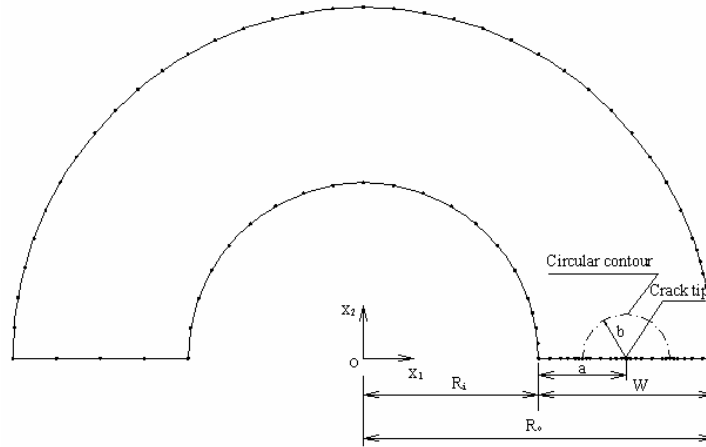


Fig. 3 Typical boundary element mesh for thick-walled cylinder

Figure 3 shows a typical BEM mesh employed, where only one-half of the physical domain needs to be modeled, by virtue of symmetry. Also shown in the figure is the contour integration path for T -stress evaluation, Γ_o , which is circular, with b/a taken to be 0.5 throughout. It should be noted that stress intensity factors for the problems treated were also obtained; they all showed excellent agreement (generally, less than 1.5 percent discrepancy) with those in the literature [14].

The T -stress solutions obtained in the analysis were normalized as T^* , where $T^* = T / \sigma_o$; with σ_o being equal to the applied internal pressure p for pressure loading cases, and is equal to the maximum hoop stress, $\hat{\sigma}_{\theta\theta}$, occurring at the bore of the cylinder, as obtained from eq. (11) in the thermal loading cases. The results for the internal pressure load cases are shown in Fig. 4 and Fig 5, the former being for situations when the internal pressure acts on the inner circumferential surface only, while the latter are for situations when only the crack faces are subjected to the pressure p . Superposition of the two sets of results will yield solutions for the case when the internal pressure acts on both the inner circumference and the crack faces. It can be seen that for these load conditions, the computed T -stress solutions all have negative values, confirming the widely accepted notion that this cracked configuration is one of low crack-tip constraint. Thus a two-

parameter approach, using the stress intensity factor and the T -stress, would provide a more appropriate and less conservative fracture assessment of the component. The normalized results of the T -stress when the cylinder is under a steady-state temperature gradient are shown in Fig. 6. The signs of their absolute values will evidently depend on whether $T_i > T_o$, or *vice versa*. Of interest to note is that for a given radius ratio, the state of crack-tip stress triaxiality may be enhanced or reduced by the thermal load, as the crack increases in size.

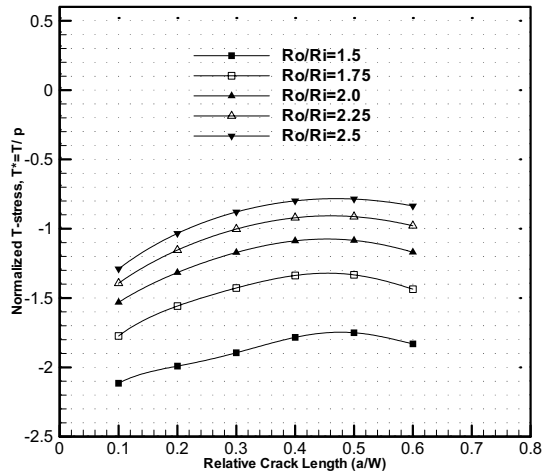


Fig. 4 BEM T -stress solutions under internal pressure loading

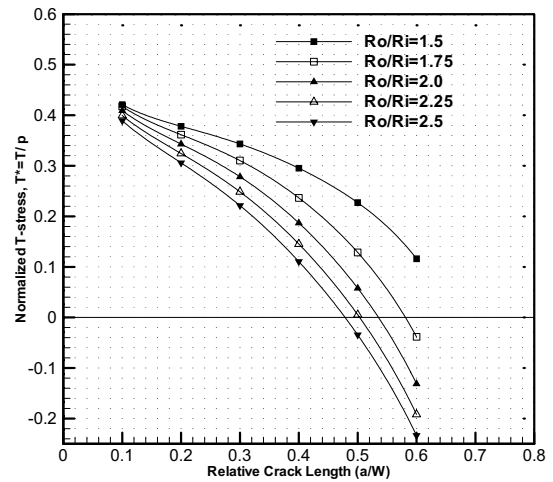


Fig. 5 BEM T -stress solutions under uniform crack face pressure loading

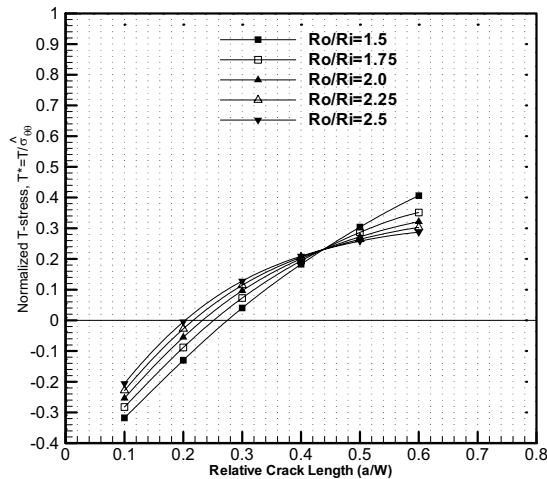


Fig. 6 BEM T -stress solutions under steady temperature gradient loading

4. Conclusion

The BEM and Sladek *et al* [10] contour integral approach have been employed to obtain T -stress solutions for a thick-walled cylinder with a radial crack. Results have been presented for cylinder radius ratios k ranging from 1.5 to 2.5, and relative crack lengths ranging from 0.1 to 0.6. Internal pressure and thermal loading cases were considered. The results confirmed that the cracked cylinder under internal pressure loading exhibits “low-constraint effects” at the crack-tip. These numerical results have not been previously available in the literature and can be used for a more reliable failure assessment by fracture of the component.

Reference

- [1] Larsson, S.G. and Carlsson, A.J. *Journal of Mechanics and Physics of Solids*, **21**, 263-277 (1973).
- [2] Rice, J.R. *Journal of Mechanics and Physics of Solids*, **22**, 17-26. (1974)
- [3] Wang, X. *Engineering Fracture Mechanics*. **69**, 1339-1352. (2002)
- [4] Du, Z.Z. and Hancock, J.W. *Journal of Mechanics and Physics of Solids*. **39**, 555-567. (1991)
- [5] Williams, M.L. *ASME Journal of Applied Mechanics*. **24**, 109-114. (1957)
- [6] Bilby, B.A., Cardew, G.E. , Goldthorpe, M.R. and Howard, I.C. *Size Effects in Fracture*. 37-46. *Mechanical Engineering Publications Limited*. (1986).
- [7] Ainsworth, R.A., Sattari-Far, I., Sherry, A.H., Hooton, D.G. and Hadley, I. *Engineering Fracture Mechanics*. **67**, 563-571. (2000).
- [8] Tan C.L. and Wang X. *Engineering Fracture Mechanics*. **70**, 2247-2252 (2003).
- [9] Li, J., *M.A.Sc. Dissertation*, Carleton University (2003)
- [10] Sladek, J., Sladek, V. and Fedelinski, P. *Theoretical and Applied Fracture Mechanics*. **27**, 115-127. (1997).
- [11] Kfourri, A.P. *International Journal of Fracture*. **20**, 301-315. (1986).
- [12] Chen, Y.Z. *International Journal of Solid Structure*. **37**, 1629-1637. (2000).
- [13] Timonshenko, S.P. and Goodier, J.N. *The Theory of Elasticity*. McGraw Hill, New York. (1956).
- [14] Andrassic, C.P. and Parker, A.P., *Engineering Fracture Mechanics*, **58**, 104-110

Nonlinear Analysis of a Reinforced Panel undergoing Large Deflection

C.Di Pisa¹, M.H.Aliabadi¹, A.Alaimo²

¹Department of Engineering, Queen Mary, University of London, UK.

London E1 4NS, UK. C.DiPisa@qmul.ac.uk,

M.H.Aliabadi@qmul.ac.uk

²Facolta' di Ingegneria Aeronautica,

Universita' di Palermo, Italy.

Keywords: Large Deflection, Stiffened Panel, Fracture Mechanics

Abstract. In this paper a boundary element method using a multi-region formulation for assembled cracked plate structures is presented. The formulation is developed by coupling the boundary element formulation for Reissner's plate and generalized plane stress. Large deflection effects have been included following an incremental load procedure. A new code has been developed and applied to analyse a reinforced panel under transverse shear load. The panel and the reinforcing elements are modelled as assembled plate structures. Damage in the structure has been included using the Dual Boundary Element Method and the Stress Intensity Factors evaluated with the crack opening displacement method. The results are in good agreement with FEM.

Introduction

The search for a better structural efficiency in modern aerospace structures requires more sophisticated tools to perform stress analyses. The effect of large deflection upon large thin panels under transverse shear load is investigated here. A new boundary element code has been developed following the formulation developed by Wen, Aliabadi & Young [3] adapted to assembled plate structures. The presence of a crack has been considered as well the stress resultant intensity factors have been evaluated using the crack opening method.

Large Deflection Theory

The basic assumption of classical plate theory is that the deflection w_3 of the plate is small compared to the plate thickness. This assumption is no longer valid when the deflection can be of the same order as the plate thickness. In this case the linear elastic strain-displacement equations are replaced by:

$$\begin{aligned}\varepsilon_{\alpha\beta} &= \frac{1}{2}(u_{\alpha,\beta} + u_{\beta,\alpha}) + \frac{1}{2}(w_{\alpha,\beta} + w_{\beta,\alpha})z + \frac{1}{2}(w_{3,\alpha}w_{3,\beta}) \\ \varepsilon_{\alpha 3} &= \frac{1}{2}(w_{\alpha} + w_{3,\alpha})\end{aligned}\quad (1)$$

Using eq.(1) the stress resultants stresses are expressed in terms of displacements as follows:

$$\begin{aligned}
N_{\alpha\beta} &= \frac{1-\nu}{2}B \left(u_{\alpha,\beta} + u_{\beta,\alpha} + \frac{2\nu}{1-\nu}u_{\gamma,\gamma}\delta_{\alpha,\beta} \right) \\
&\quad + \frac{1-\nu}{2}B \left(w_{3,\alpha}w_{3,\beta} + \frac{\nu}{1-\nu}w_{3,\gamma}w_{3,\gamma}\delta_{\alpha,\beta} \right) \\
&= N_{\alpha\beta}^l + N_{\alpha\beta}^n \\
M_{\alpha,\beta} &= \frac{1-\nu}{2}D \left(w_{\alpha,\beta} + w_{\beta,\alpha} + \frac{2\nu}{1-\nu}w_{\gamma,\gamma}\delta_{\alpha,\beta} \right) \\
Q_\alpha &= \frac{5}{6}Gt(w_\alpha + w_{3,\alpha}) + N_{\alpha\beta}w_{3,\beta}
\end{aligned} \tag{2}$$

where $B = Eh/(1 - \nu^2)$ is the tension stiffness and $D = Eh^3/12(1 - \nu^2)$ is the flexural rigidity.

Because of the deflection derivatives in the in-plane stress resultants expression, the bending and the membrane behaviour of the plate are no more independent.

The equilibrium equations can be rewritten as follows:

$$\begin{aligned}
N_{\alpha\beta,\beta} + f_\alpha &= 0 \\
M_{\alpha\beta,\beta} - Q_\alpha &= 0 \\
Q_{\alpha,\alpha} + N_{\alpha\beta}(w_{3,\alpha})_{,\beta} + q_3 &= 0
\end{aligned} \tag{3}$$

Modifications of the basic theory to allow for large deflections result in the inclusion of extra non-linear terms in classical Reissner's type boundary element equations[1]. The corresponding boundary integral equations are then of the form:

$$\begin{aligned}
&c_{\alpha\beta}(x')u_\beta(x') + \int_\Gamma T_{\alpha\beta}(x', x)u_\beta(x)d\Gamma(x) - \int_\Gamma U_{\alpha\beta}(x', x)t_\beta(x)d\Gamma(x) \\
&= \int_\Sigma U_{\alpha\beta}(x', X) \left(f_\beta(X) + N_{\beta\gamma,\gamma}^n(X) \right) d\Sigma(X) \\
&\quad - \int_\Gamma U_{\alpha\beta}(x', x)N_{\beta\gamma,\gamma}^n(x)d\Gamma(x)
\end{aligned} \tag{4}$$

$$\begin{aligned}
&c_{ik}(x')w_k(x') + \int_\Gamma P_{ik}(x', x)w_k(x)d\Gamma(x) - \int_\Gamma W_{ik}(x', x)p_k(x)d\Gamma(x) \\
&= \int_\Sigma W_{i3}(x', X) \left(q_3(X) + (N_{\alpha\beta}w_{3,\beta}(X))_{,\alpha} \right) d\Sigma(X)
\end{aligned} \tag{5}$$

where u_α are in-plane displacements, w_j are the rotations in x and y , t_α in-plane tractions, p_j are the bending moments and the shear tractions, q_3 is the internal pressure. $T_{\theta\alpha}(x', x)$ and $U_{\theta\alpha}(x', x)$ represent the Kelvin fundamental solutions for plane stress elasticity, while $P_{ij}(x', x)$, $W_{ij}(x', x)$ are the Reissner plate fundamental solutions [1]. Greek indices vary from 1 to 2, Roman indices from 1 to 3. For crack problems, the classical Reissner's type traction equations[1] include extra non-linear terms analogous to those in eq.(4) and (5). All the domain integrals are transferred to the boundary using the Dual Reciprocity Method[1].

Once the system has been built for each plate, compatibility and equilibrium equations are enforced along the joining lines [4] accounting for the effects due to the non-linear stress resultants.

Incremental Load Approach

The system of non-linear equations generated from eq.(4) and eq.(5) is solved using an incremental load approach. Following [3] the load is divided into several quasi-linear steps, in which the new integrals containing the non-linear terms are considered as an additional load to be computed from the previous step. In matrix form it can be written as:

$$\begin{aligned}Hu^k - Gt^k &= F(f + (N_{\beta\gamma,\gamma}^n)^{k-1}) + (Gt^n)^{k-1} \\Pw^k - Wp^k &= F(q_3 + ((N_{\alpha\beta}w_{3,\beta}(X)),_\alpha)^{k-1})\end{aligned}\quad (6)$$

$k=\text{current step}$

where H, G, P, W are boundary element influence matrices, F is a domain integral matrix to be multiplied by the domain loads (f, q_3) and the non-linear additional quantities are evaluated from the solution at the step $k - 1$.

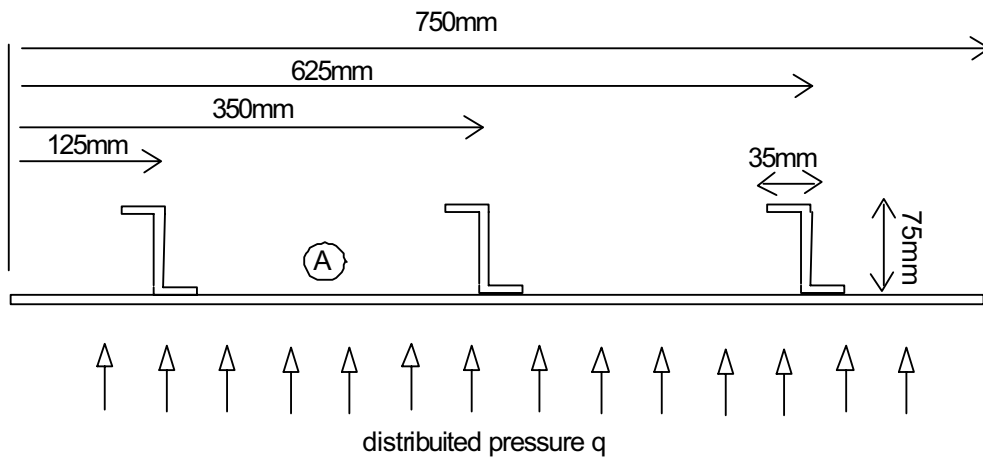
The Stress Resultant Intensity Factors for plate membrane and bending are evaluated using the COD method analogously to the linear cases [2], and then related to the classical SIF.

Reinforced Panel under transverse shear load

A flat square panel reinforced with three Z-stringers (from the wing box of the B-52 Strato-fortress) as shown in Fig.1. is subjected to the transverse load $q = 0,06MPa$ and it is considered to be simply supported on all sides. The material is aluminium 7075-T6 of Young Modulus $E = 71016MPa$ and Poisson's ratio $\nu = 0.33$. The panel and the stringers are modelled with 13 thin plates in total. Each plate is divided into 32 quadratic elements. In Fig.2. the maximum deflection for the BEM and FEM in large deflection are compared with the FEM and BEM linear elastic solutions. In Fig.3. and Fig.4. the deflection contours for the BEM and the FEM models are compared. The agreement is found to be very good.

A central crack of size $c = 32.25mm$ is then placed in plate (A). In this case the load had is reduced to $q = 0,045MPa$; the crack-points are very sensitive to the effects of large deflection. The load increment has been taken as $\delta q = 0,001MPa$. The mode I Stress Resultant Intensity Factor for membrane (K_I^m) and for bending (K_I^b) are evaluated using the COD method. The maximum mode I Stress Intensity Factor (K_I^{max}) is then calculated for each load step as: $K_I^{max} = K_I^m/h + |K_I^b| \times 6/h^2$. In Fig.5. the K_I^{max} is plotted against the correspondent linear. The increase in the K_I^{max} is probably because of the arising of the membrane I SIF due to the coupling between bending and in-plane stresses. It can be seen that while in small deflection theory the K_I^{max} is well below the critical value ($K_I^{crit} \cong 30MPa\sqrt{m}$ for panels $\cong 2.5mm$ thick, made of Aluminium 7075-T6. [5]), in large deflection it approaches the critical value. The contours of the deflection for the cracked model is presented in Fig.6.

Panel Cross Section



Skin Thickness = 2.5mm
 Z-Stiffener Thickness = 5mm

(A) Cracked Panel

Figure 1: Z-Stiffened Panel Geometry: Cross Section

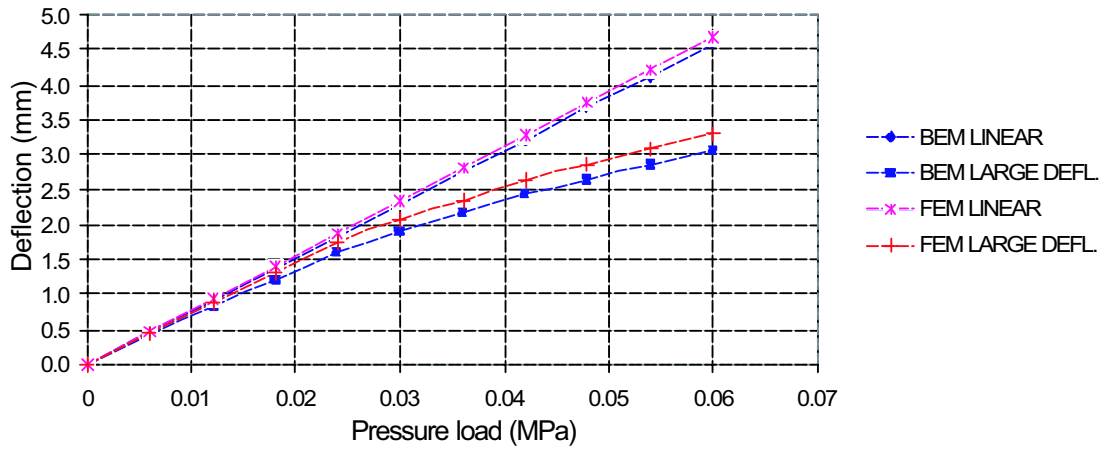


Figure 2: Maximum Deflection

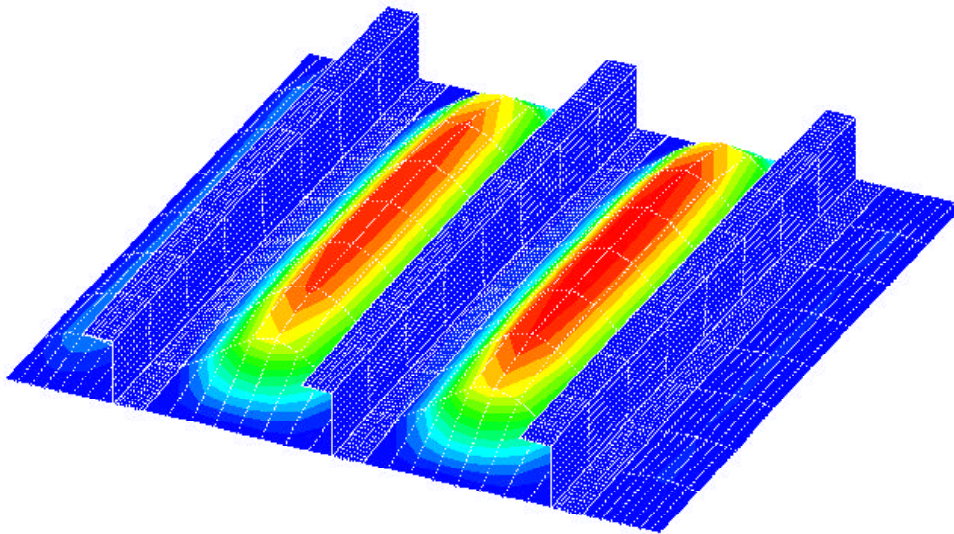


Figure 3: BEM model: Deflection contours

Summary

In this paper a practical application of a new boundary element formulation involving assembled plates and large deflection in presence of cracks has been investigated. The results obtained for the un-damaged model are in good agreement with finite element. The cracked model has not yet been compared with a similar geometry, but the results are in agreement with what would be expected from the theory. The BEM formulation for assembled plate structures has shown its versatility to be applied not only to large plates but also to thin structural element such as stringers. The formulation will provide an effective tool for the analysis of complex aircraft structures.

References

- [1] M.H.Aliabadi *The Boundary Element Method, vol II: application to solids and structures* Wiley (2002).
- [2] T.Dirgantara and M.H.Aliabadi *Engineering Fracture Mechanics*, **69**, 1465-1486 (2002).
- [3] Wen, P.H., Aliabadi, M.H., Young, A., *Large Deflection Analysis of Reissner Plate by Boundary Element Method.*(to appear)
- [4] T.Dirgantara and M.H.Aliabadi *Commun.Numer.Meth.Engng*, **17**, 749-760 (2001).
- [5] M.C.Y.Niu *Airframe Structural Design*, Hong Kong Conmilt Press LTD (1997)

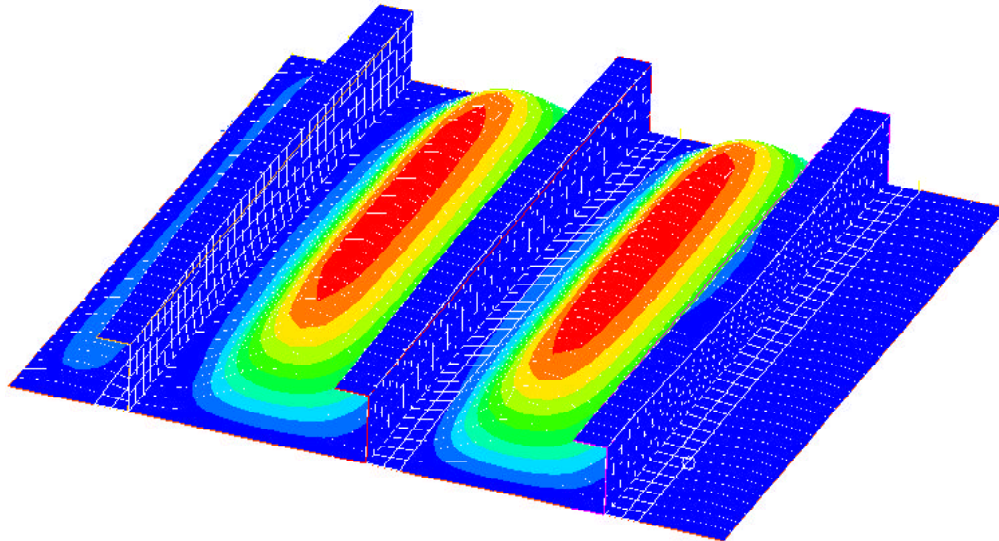


Figure 4: FEM model: Deflection contours

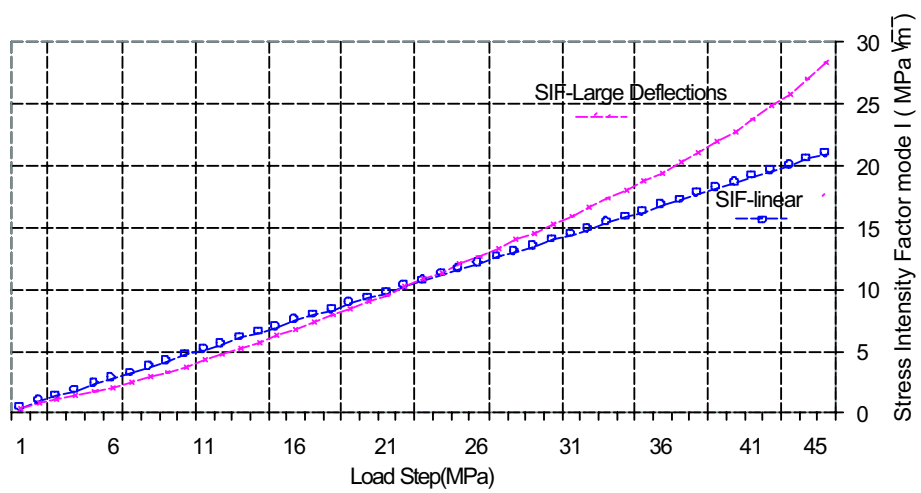


Figure 5: Stress Intensity Factor mode I

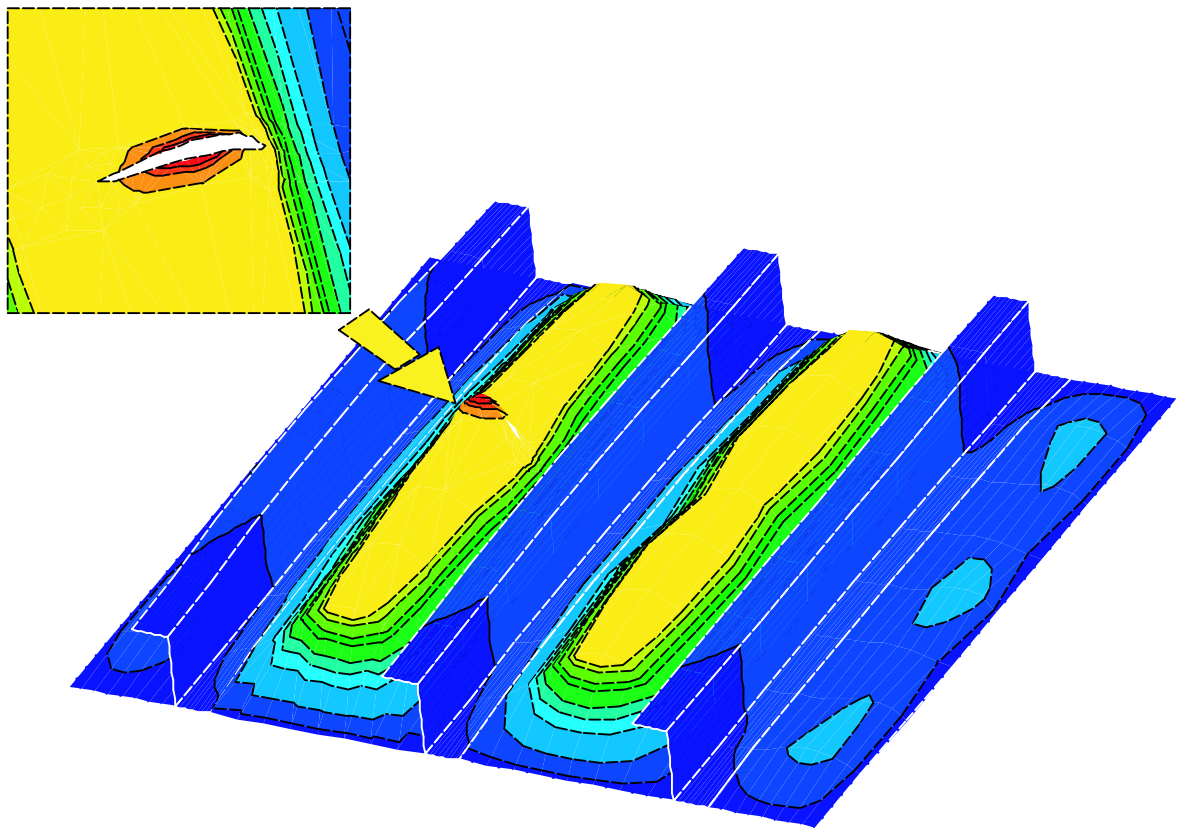


Figure 6: Cracked Panel: Deflection contour

Localisation analysis by BEM in damage mechanics

V. Mallardo

Department of Architecture – via Quartieri 8 – 44100 Italy – mlv@unife.it

Keywords: Damage, BEM, softening

Abstract. In this paper a thermodynamically consistent damage mechanic model is presented in the context of a boundary element formulation. In particular, the damage model of Lemaitre is considered. The boundary element method (BEM) is applied by introducing convenient inelastic strains which account for the irreversibly degeneration of the mechanical properties due to a diffused microcracking in the structure. The theoretical background of the model as well as the boundary element formulation are presented. The governing relations are first derived by the free energy potential fully complying with thermodynamic principles, then the flaw laws are obtained by assuming the existence of a damage activation function and under the hypothesis of generalised associative damage behaviour, finally numerical results are obtained by coupling suitably the BEM with the arclength methods.

Introduction

Quasibrittle materials, such as concrete, rock, tough ceramics, are characterised by the development of nonlinear fracture process zones, which can be macroscopically described as regions of highly localised strains. Continuum-based modelling of the progressive growth of microcracks and their coalescence requires constitutive laws with strain softening. Damage models are known to describe the accumulation of continuum damage, the initiation of micro cracks, and their coalescence to macro cracks as a function of the loading process. One of the most commonly used damage models, more phenomenologically based, was first introduced by Kachanov. An additional damage variable is introduced in the constitutive equations in order to describe the portion of the structure which is still able to carry load. After this original work, an impressive research activity has been carried out aimed both at the development of models suitable for describing a large number of materials and at solving the problems connected with softening behaviour, non-unique solutions and unstable paths.

In this paper the BEM is applied to the model initially proposed by Kachanov and then developed by [1]. Numerical results are shown in order to discuss the post-peak behaviour of such model. In the context of standard continuum damage mechanics, in fact, softening leads to serious mathematical and numerical difficulties. The boundary value problem becomes ill-posed, and the numerical solution exhibits a pathological sensitivity to the computational discretisation. As a remedy, regularisation techniques enforcing a mesh-independent profile of localised strains are used. The governing relations of the damage model are derived by introducing a free energy potential which fully complies with thermodynamic principles; the state laws are written on the basis of the intrinsic dissipation at a given point and finally the flaw laws are obtained by assuming the existence of a damage activation function and under the hypothesis of generalised associative damage behaviour.

A similar boundary integral formulation, as obtained by [2], can be derived by introducing an additional domain integral which represents the nonlinear damage behaviour of the material. For softening localisation phenomena, it must be underlined that the nonlinear term tends to localise into a small region of the solid, therefore the advantage of BEM in reducing the number of unknowns by discretising only the boundary and the subregion in which the nonlinearity occurs is still valid. The BEM/arclength procedure for general material nonlinear problems presented in [3] is applied. The boundary element initial stress approach is coupled with the arclength constraint in order to deal with possible snap-back behaviours.

Numerical solutions are presented both for linear and for quadratic damage.

The damage model

In what follows a simple damage model is described. Damage may be interpreted at the microscale as the creation of microsurfaces of discontinuities: breaking of atomic bonds and plastic enlargement of microcavities. At the mesoscale, the number of broken bonds or the pattern of microcavities may be approximated in any plane by the area of the intersections of all the flaws with that plane. This area is scaled by the size of the representative volume element (RVE). The damage can be quantified by means of a scalar parameter d which, in any point, given the direction of a plane, represents the ratio between the effective area of the intersection of all microcracks lying in the plane and the area of the intersection of the plane with the RVE. The damage is assumed to be isotropic, i.e. d is assumed not to vary with the direction of the plane. The formulation is confined to the case of small induced strains. Let the Helmholtz free energy be of the form:

$$\Psi(\varepsilon, d, \xi) = \frac{1}{2} \varepsilon : f(d) \mathbf{C}^e : \varepsilon + \frac{1}{2} h \xi^2 \quad (1)$$

where the first term is the damage elastic strain energy and second term is the part of energy stored in the micro-structure related to the change of the material internal properties. ξ is a scalar kinematic internal variable which describes the damage hardening state. The dissipative irreversible mechanism associated to the damage is governed by the couple of variables \dot{d} and $\dot{\xi}$ which appear in the expression of the intrinsic dissipation:

$$\dot{D} = \sigma : \dot{\varepsilon} - \dot{\Psi} \geq 0 \quad (2)$$

The expression of the free energy rate can be obtained by differentiating equation (1):

$$\dot{\Psi}(\varepsilon, d, \xi) = \varepsilon : f(d) \mathbf{C}^e : \dot{\varepsilon} + \frac{1}{2} \varepsilon : \frac{\partial f(d)}{\partial d} \mathbf{C}^e : \varepsilon \dot{d} + h \xi \dot{\xi} \quad (3)$$

By introducing this relation into (2), and reminding the inequality must hold for any admissible deformation mechanism, either nondissipative elastic or irreversible damaging one, the following state laws are obtained:

$$\sigma = f(d) \mathbf{C}^e : \varepsilon \quad (5a)$$

$$Y := -\frac{1}{2} \frac{\partial f(d)}{\partial d} \varepsilon : \mathbf{C}^e : \varepsilon \quad (5b)$$

$$\chi := h \xi \quad (5c)$$

The existence of a damage activation function $\phi(Y, \chi)$ is now assumed. Under the hypothesis of generalised associative damage behaviour, the damage activation function can be written in the following form:

$$\phi(Y, \chi) = Y - Y_0 - \chi \leq 0 \quad \dot{\lambda} \geq 0 \quad \dot{\lambda} \phi = 0 \quad \text{in } \Omega \quad (6)$$

where $\dot{\lambda}$ is the damage multiplier. Consequently the flaw laws read:

$$\dot{d} = \frac{\partial \phi}{\partial Y} \dot{\lambda} = \dot{\lambda}, \quad \dot{\xi} = -\frac{\partial \phi}{\partial \chi} \dot{\lambda} = \dot{\lambda} \quad \text{in } \Omega \quad (7)$$

Now the material response to an assigned strain rate field $\dot{\varepsilon}(\mathbf{x})$ is investigated. If Ω_d is the part of the body which is damaged, the response at \mathbf{x} is locally elastic if $\mathbf{x} \notin \Omega_d$, whereas at the points $\mathbf{x} \in \Omega_d$ the response is elastic-damaging and the following relations must hold:

$$\dot{\phi}(Y, \chi) \leq 0 \quad \dot{d} = \dot{\xi} = \dot{\lambda} \geq 0 \quad \dot{\phi} \dot{\lambda}_d = 0 \quad \text{in } \Omega_d \quad (8)$$

Expanding the damage activation function in its rate form leads to:

$$\dot{\phi}(Y, \chi) = \frac{\partial \phi}{\partial Y} \dot{Y} + \frac{\partial \phi}{\partial \chi} \dot{\chi} = \dot{Y} - \dot{\chi} \leq 0 \quad \dot{\lambda} = \dot{d} = \dot{\xi} \geq 0 \quad \dot{\phi} \dot{\lambda} = 0 \quad (9)$$

where:

$$\dot{Y} = -\frac{1}{2} \frac{\partial^2 f(d)}{\partial d^2} \varepsilon : \mathbf{C}^e : \varepsilon \dot{d} - \frac{\partial f(d)}{\partial d} \varepsilon : \mathbf{C}^e : \dot{\varepsilon} \quad \dot{\chi} = h \dot{\xi} \quad (10)$$

By introducing relations (10) into relation (9) the complete incremental damage problem can be stated as follows:

$$\dot{\phi}(Y, \chi) = -\frac{1}{2} \frac{\partial^2 f(d)}{\partial d^2} \varepsilon : \mathbf{C}^e : \varepsilon \dot{d} - \frac{\partial f(d)}{\partial d} \varepsilon : \mathbf{C}^e : \dot{\varepsilon} - h \dot{\xi} \leq 0 \quad (11a)$$

$$\dot{\lambda} = \dot{d} = \dot{\xi} \quad \dot{\phi} \dot{\lambda} = 0 \quad \text{in } \Omega_d \quad (11b)$$

The BEM in damage analysis

Applications of BEM to localisation phenomena can be found in [4-6]. The main limit of these approaches is the incapability to fully cope with problems involving snap-back behaviours, typically related to the localisation of the strains. In this contribution the coupling procedure BEM/arclength for physically nonlinear problems proposed in [3] will be adopted. Without loss of generality, the explicit version of the initial stress approach will be implemented within the context of the small strain theory. In order to keep a unified notation, these equations will be presented in rate form. In the absence of body forces, the displacement boundary integral equation can be written as

$$c_{ij}(\xi) \dot{u}_j(\xi) + \int_{\Gamma} t_{ij}^*(\xi, \mathbf{x}) \dot{u}_j(\mathbf{x}) d\Gamma(\mathbf{x}) = \int_{\Gamma} u_{ij}^*(\xi, \mathbf{x}) \dot{t}_j(\mathbf{x}) d\Gamma(\mathbf{x}) + \int_{V_d} \varepsilon_{ijk}^*(\xi, \mathbf{x}) \dot{\sigma}_{jk}^d(\mathbf{x}) d\Omega(\mathbf{x}) \quad (12)$$

and the stress in any internal point is given by:

$$\dot{\sigma}_{ij}(\mathbf{X}) = \int_{\Gamma} U_{ijk}^*(\mathbf{X}, \mathbf{x}) \dot{t}_k(\mathbf{x}) d\Gamma(\mathbf{x}) - \int_{\Gamma} T_{ijk}^*(\mathbf{X}, \mathbf{x}) \dot{u}_k(\mathbf{x}) d\Gamma(\mathbf{x}) + \int_{V_d} \Xi_{ijkl}^*(\mathbf{X}, \mathbf{x}) \dot{\sigma}_{kl}^d(\mathbf{x}) d\Omega(\mathbf{x}) + g_{ij}(\dot{\sigma}^d(\mathbf{X})) \quad (13)$$

where Γ is the boundary of the domain of volume Ω , $\dot{\mathbf{u}}$ and $\dot{\mathbf{t}}$ are, respectively, displacement and traction increment fields on the boundary, and the expression of the fundamental solution t_{ij}^* , u_{ij}^* , ε_{ijk}^* , T_{ijk}^* , U_{ijk}^* , Ξ_{ijkl}^* and g_{ij} are given for instance in [7]. In the equations (12-13) ξ and \mathbf{x} belong to the boundary and are usually referred as source and field point, respectively, \mathbf{X} is an internal point. The nonlinear term σ^d , appearing in the above equations, can be considered utterly equivalent to the plastic stress. In fact:

$$\sigma = f(d) \mathbf{C}^e : \varepsilon = \mathbf{C}^e : \varepsilon - \sigma^d = \sigma^{el} - \sigma^d \quad (14)$$

By discretising both the boundary Γ in continuous quadratic elements and the part of Ω in which the damage is expected to occur in quadratic quadrilateral internal cells, by applying the Dirichlet/Neumann boundary conditions and by collocation technique, the equation (12) can be re-written as:

$$\mathbf{A} \dot{\mathbf{x}} = \dot{\mathbf{f}} + \mathbf{Q} \dot{\sigma}^d \quad (15)$$

whereas the internal and boundary stresses can be collected in:

$$\dot{\sigma}^{el} = -\mathbf{A}' \dot{\mathbf{x}} + \dot{\mathbf{f}}' + (\mathbf{Q}' + \mathbf{E}' + \mathbf{I}) \dot{\sigma}^d = -\mathbf{A}' \dot{\mathbf{x}} + \dot{\mathbf{f}}' + \bar{\mathbf{Q}} \dot{\sigma}^d \quad (16)$$

The stress rate in any boundary point is obtained by special relations depending on traction rates and numerical tangential derivative of the displacement.

The evolution problem for a finite time step Δt and for any given strain increment $\Delta \varepsilon = \varepsilon_{s+1} - \varepsilon_s$ is considered. The iterative incremental procedure is based on a special coupling of the equations (15-16) with the arclength constrain. Furthermore a return-mapping algorithm, i.e.:

$$\Delta d = \frac{Y_{s+1} - \phi_s}{h} \quad \text{linear damage} \quad \Delta d = \frac{(1-d)Y_{s+1} - \phi_s}{h + Y_{s+1}} \quad \text{quadratic damage} \quad (17)$$

The increment of the nonlinear term σ^d , which is necessary at every step of the iterative procedure, can be easily obtained:

$$\Delta \sigma^d = d \mathbf{C}^e : \Delta \varepsilon + \Delta d \mathbf{C}^e : \varepsilon_s \quad \text{linear damage} \quad (18a)$$

$$\Delta \sigma^d = 2d (\mathbf{C}^e : \Delta \varepsilon - \Delta d \mathbf{C}^e : \varepsilon) - d^2 \mathbf{C}^e : \Delta \varepsilon + 2d \mathbf{C}^e : \varepsilon \quad \text{quadratic damage} \quad (18b)$$

The arclength methods represent the only alternative to classical load/displacement control algorithms which is able to pass critical limit point (i.e. snap-back or snap-through). The main idea is to consider the load increment as a variable: a new equation requiring that the new equilibrium point is searched on an arc of fixed radius and the center set in the previous equilibrium state is added.

In [3] the arclength constraint is introduced into a typical BEM iterative procedure for physically nonlinear problems. The resulting nonlinear system of equations is discussed and solved. In the generic time step, such procedure furnishes the following additive corrections to be evaluated sequentially:

$$\delta \mathbf{x} = -\mathbf{A}^{-1} \mathbf{R}_o + \mathbf{A}^{-1} \mathbf{f} \delta \lambda = \delta \mathbf{x}^I + \delta \lambda \delta \mathbf{x}^{II} \quad (19a)$$

$$\delta \lambda = -\frac{\Delta \mathbf{x}_o^T \delta \mathbf{x}^I}{\Delta \mathbf{x}_o^T \delta \mathbf{x}^{II}} \quad (19b)$$

$$\delta \sigma^{el} = -R'_o - \mathbf{A}' \delta \mathbf{x} + \mathbf{f}' \delta \lambda \quad (19c)$$

The subscript o indicates old, i.e. $(\cdot)_n = (\cdot)_o + \delta(\cdot)$, whereas R_o and R'_o are related to the error of the previous iteration step.

Numerical analyses

In all the numerical examples here presented a rectangular plate $1000 \times 1250 \text{ mm}^2$ in plane stress and loaded on the horizontal top line by a constant load $p = 2.0 \text{ N/mm}^2$ is considered. The following values of the material properties are used: $E = 20000 \text{ N/mm}^2$, $\nu = 0.30$, $Y_0 = 1.0E - 04 \text{ N/mm}^2$ and $h = 8.0E - 04 \text{ N/mm}^2$. Three different internal meshes are used to evaluate the domain integral: 4×5 , 8×10 and 12×15 . The load-displacement diagrams describe graphically the relationship between the vertical displacement of the central point of the top horizontal line and the load factor λ .

The first example has the purpose to check the accuracy of the proposed procedure. Both linear damage and quadratic damage present good results: the uniform stress

field is captured properly by the model. Figure 1 presents the results for the three meshes considered. It must be underlined that, in the case of linear damage, the instability appears for every mesh, i.e. a lack of convergence at $\lambda = 0.9$ in the post peak branch occurs.

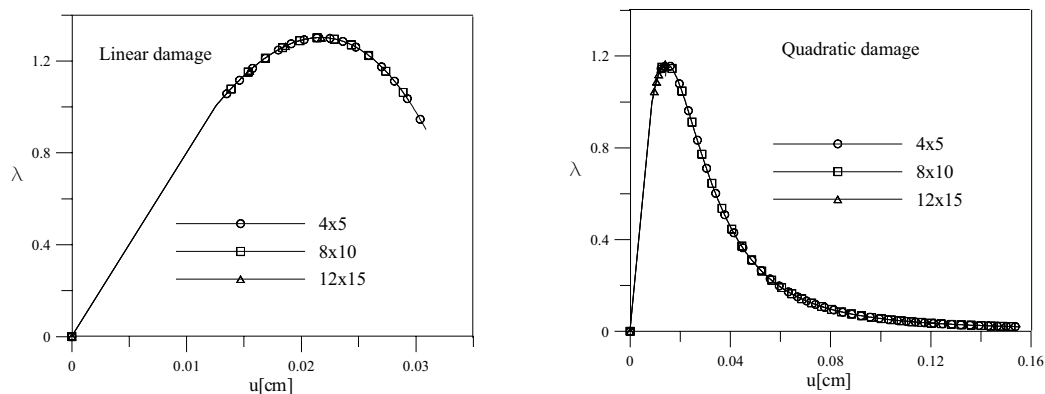


Fig. 1 – Load parameter versus top displacement – Uniform strength

On the other hand, in case of quadratic damage the load-displacement curve has no stop due to the lost of convergence, but the finest mesh cannot pass the peak point. Figure 2 shows the increasing of the damage parameter. Only in the case of quadratic damage the maximum value $d = 1$ is reached.

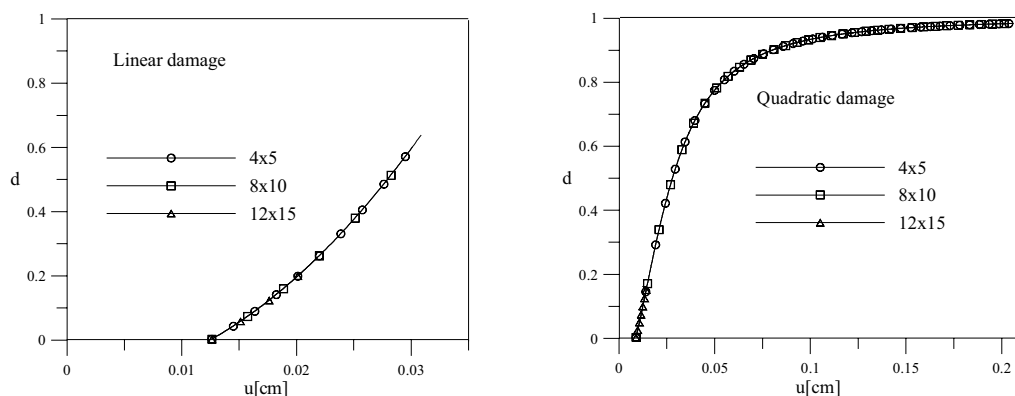


Fig. 2 – Damage parameter versus top displacement – Uniform strength

The second example is able to point out the constitutive instability due to the locality of the model. The initial value of Y_0 in the domain cell in the bottom-left corner of the plate is taken 5% lower than the value in the remaining domain cells. This is done in order to trigger the localisation of the damage and to show the pathological mesh dependence in the numerical results. Figure 3, infact, shows that the post-peak response is captured, with great numerical difficulties, only in the case of quadratic damage. Besides, both for linear and for quadratic damage, the numerical response is dependent on the internal mesh.

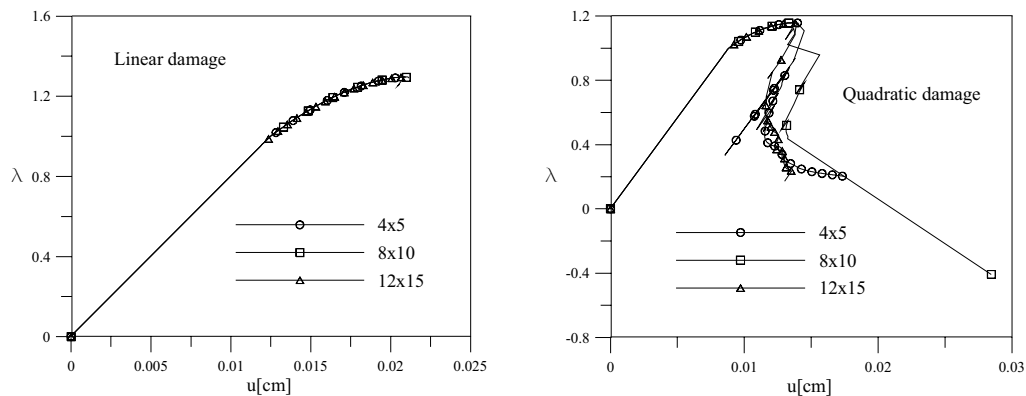


Fig. 3 – Load parameter versus top displacement – Weakened strength

Summary

A nonlinear Boundary Element procedure has been proposed for damage models. In order to pass critical limit points, the algorithm has been combined with the arclength methods. Constitutive instability has been highlighted in two simple numerical examples. The strain softening is source of theoretical and computational difficulties for continuum based structural modelling, which are substantially originated by constitutive instability matters as pointed out by many researchers. A non-local BEM formulation of integral type is developed in [5], whereas a gradient approach with an implicit boundary element formulation is proposed in [6]. Both papers deal with the classical plasticity. Numerical analyses are still in progress: some more work need to be done in order to implement regularised damage models and to obtain numerical results in more complex situations.

References

- [1] J.A.Lemaitre *A Course on Damage Mechanics*, Springer-Verlag (1992).
- [2] S. Rajgelj, C. Amadio, A. Nappi *Boundary Element Technology VII*, ed. C.A. Brebbia & M.S. Ingber, Elsevier Applied Science, London, 1992, pp.617-634.
- [3] V.Mallardo, C. Alessandri *Engineering Analysis with Boundary Elements*, **28**(6), 547-559, (2004).
- [4] C. Alessandri, V. Mallardo, A. Tralli, *Advances in Computational Engineering & Sciences Vol. II, Int. Conf. on Computational Engineering Science*, ICES 2000, Los Angeles, pp. 1293-1298, (2000).
- [5] J. Sládek, V. Sládek, Z. P. Bažant, *International Journal for Numerical Methods in Engineering*, **57**, 417-424, (2003).
- [6] A. Benallal, C.A. Fudoli, W.S. Venturini, *International Journal for Numerical Methods in Engineering*, **53**, 1853-1869, (2002).
- [7] M.H. Aliabadi *The Boundary Element Method, Vol2: Applications in Solids and Structures*, Wiley (2002).

Acoustic scattering by multicrocks using a boundary finite element method

Carlos J. S. Alves

CEMAT - Department of Mathematics, Instituto Superior Técnico
Av. Rovisco Pais 1, 1049-001 Lisboa, Portugal
e-mail: Carlos.Alves@math.ist.utl.pt

Keywords : Boundary Element Method, Finite Elements, Acoustic Scattering, Crack Detection, Multicrocks.

Abstract. The numerical simulation of crack scattering is an exterior problem where the use of boundary element methods is recommended. However when considering Neumann boundary conditions in the crack, difficulties connected to the hypersingularity in double layer potential kernel arise. The use of a boundary variational formulation on the boundary allows to overcome this difficulties. This was introduced in Nédélec [14] for the Laplace equation, and developed by Hamdi [9] for the case of acoustic scattering. The case of flat cracks has been addressed by Ha Duong [8]. In the case of a single flat cracks this method has been applied [1] with robust results also in the elastic crack scattering framework. In [3] the method was extended to non-planar cracks and here we present the multicrock case, showing simulations for the convergence of the method and we discuss some results concerning crack identification.

Introduction

The numerical simulation of acoustic and elastic scattering by cracks has been associated with several applications, namely the control and detection of imperfections in some materials. Some of the first numerical studies considered scattering by flat simple shaped cracks, such as the penny-shaped crack (eg. Bouwkamp [6], Jones [11]), where a solution was possible using special coordinate systems. This exterior problem was suitable to boundary element method approach, but it had a major difficulty arising from the hypersingularity in the kernel of the associated first kind boundary integral equation. The integral could only be defined in a weak sense and some of the first successful methods used a truncated series expansion (cf. [12]). More recently some techniques with regularization have been applied to the standard collocation boundary element method (eg. [5], [13]). On the other hand, since the works of Nédélec [14] and [10] the introduction of a finite element method associated to the variational formulation of the boundary integral equation gave new possibilities to the boundary element method. This technique has been applied in the case of acoustic scattering (cf. Hamdi [9]), and in the particular case of plane cracks coercivity was proven (cf. Ha Duong [8]). The numerical simulation for acoustic and elastic plane flat cracks was presented in [1], showing the good performance of this technique compared to previous ones. In [3] simulations for the more general case of acoustic scattering by a non flat crack have been presented. In this work we show some numerical simulations applying the method to multicrocks, analysing the convergence of the method and presenting some preliminary simulations that may lead to criteria showing the influence of the multicrock framework on crack detection as in [2].

Acoustic Scattering by Cracks

We consider the general setting for time-harmonic acoustic scattering by cracks, which is modelled by the Helmholtz equation, and we will be mainly interested in wavelenghts that are comparable to the dimensions of the crack. Scattering models for short or long wavelenghts can be simpler using asymptotic expansions (e.g. [4]). We will denote by Γ the set of c surfaces describing the cracks $\Gamma_1, \dots, \Gamma_c$, each one considered as a part of regular boundary (piecewise C^1) of a bounded domain of \mathbb{R}^3 . Thus, the set Γ has c connected components, each surface describing a crack, and we assume that each surface is orientable, excluding not only some exhotic surfaces like the Möbius strip, but also crack bifurcations.

In the homogeneous medium we assume that the constant propagation speed is unitary, and therefore the wavenumber $k > 0$ coincides with the frequency.

The amplitude of the scattered wave u verifies the Helmholtz equation in the domain $\mathbb{R}^3 \setminus \Gamma$,

$$\Delta u + k^2 u = 0 \quad \text{in } \mathbb{R}^3 \setminus \Gamma$$

and on the crack surface the Neumann boundary condition is considered,

$$\partial_n u = -\partial_n u^{inc} \quad \text{on } \Gamma.$$

Here will be mainly interested in plane incident waves

$$u^{inc}(x) = e^{ikx \cdot d},$$

with propagation direction $d \in S^2$ (here S^2 represents the unitary sphere). Thus we obtain the following problem

$$\begin{cases} \Delta u + k^2 u = 0 & \text{in } \mathbb{R}^3 \setminus (\cup_{m=1}^c \Gamma_m) \\ \partial_n u = -\partial_n u^{inc} & \text{on } \Gamma \\ \partial_r u - ik u = o(r^{-1}) & \text{when } r = |x| \rightarrow \infty, \end{cases}$$

where the last condition is the *Sommerfeld radiation condition*, that allows to establish the uniqueness of the problem. This a well posed problem (cf. [7]) and furthermore the asymptotic behavior of the scattered wave can be described by the relation

$$u(x) = \frac{e^{ikr}}{r} u_\infty(\hat{x}) + o\left(\frac{1}{r}\right),$$

where $\hat{x} = \frac{x}{|x|} \in S^2$, and u_∞ is an analytic function on S^2 , known as the *far field*. The far field determines completely the scattered wave (a Theorem by Rellich).

We consider the multicrack framework where $\Gamma = \Gamma_1 \cup \dots \cup \Gamma_c$, and each Γ_m is a connected component of Γ . The solution of this problem can be described through the double layer potential (e.g. [8])

$$\begin{aligned} u(x) &= \int_{\Gamma} \partial_{n_y} \Phi(x-y) \varphi(y) ds_y, \quad (x \in \mathbb{R}^3 \setminus \Gamma) \\ &= \sum_{m=1}^c \int_{\Gamma_m} \partial_{n_y} \Phi(x-y) \varphi_m(y) ds_y \end{aligned} \quad (1)$$

where Φ is the 3D fundamental solution of the Helmholtz equation, given by

$$\Phi(x) = \frac{e^{ik|x|}}{4\pi|x|}, \quad \text{with } |x|^2 = x_1^2 + x_2^2 + x_3^2$$

where $\varphi_m \in H_{00}^{1/2}(\Gamma_m)$ is a density function determining the jump in the crack Γ_m known as the *crack opening displacement*. The jump is defined by the difference between the two traces of the solution in Γ_m , that is, $\varphi = [u] = u^- - u^+$.

On the other hand, the normal trace of the double layer potential is given by

$$-\partial_{n_x} u^{inc}(x) = \partial_{n_x} \int_{\Gamma} \partial_{n_y} \Phi(x-y) \varphi(y) ds_y, \quad (2)$$

leading to an integral equation of the first kind. The boundary element method presents now a difficulty related to the hypersingularity in the integral kernel, since

$$\partial_{n_x} \partial_{n_y} \Phi(x-y) = O\left(\frac{1}{|x-y|^3}\right)$$

is not integrable in the usual sense.

The boundary variational formulation obtained by Hamdi (cf. [9]) is now applied to non planar cracks. The variational problem consists in the determination of the density function $\varphi \in H_{00}^{1/2}(\Gamma)$ such that

$$\begin{aligned} &\int_{\Gamma} \int_{\Gamma} \Phi(x-y) (\mathbf{rot}_{\Gamma} \varphi(x) \cdot \mathbf{rot}_{\Gamma} \bar{\psi}(y) - \\ &- k^2 \mathbf{n}_x(x) \cdot \mathbf{n}_y(y) \varphi(x) \bar{\psi}(y)) ds_y ds_x = - \int_{\Gamma} \partial_n u^{inc}(x) \bar{\psi}(x) ds_x, \end{aligned} \quad (3)$$

for any test function $\psi \in H_{00}^{1/2}(\Gamma)$. The differential operator \mathbf{rot}_Γ is the surface rotational given by

$$\mathbf{rot}_\Gamma \varphi(x) = \mathbf{n}_x \times \nabla \tilde{\varphi}(x).$$

This way we circumvent the problem of integrating an hypersingular kernel, since the double derivation of the kernel given by the fundamental solution $\Phi(x-y)$ is transferred in the weak formulation to the derivative of the crack opening displacement density and to the derivative of the test function.

Boundary Finite Element Method

The boundary finite element method combines the discretization with boundary elements with the finite element approach. We will use \mathcal{P}_1 basis functions defined on those boundary elements. The greater difficulty of the method consists in the approximation of the double integration since the kernel defined by the fundamental solution remains weakly singular.

In the case of multicracks $\Gamma = \Gamma_1 \cup \dots \cup \Gamma_c$, each of the surfaces Γ_m will be represented by the graph of a function f_m defined on plane surface Q_m (for instances, an \mathbb{R}^2 rectangle), that is $\Gamma_m = f_m(Q_m)$,

$$\Gamma_m = \{(x^*, f_m(x^*)), \text{ com } x^* \in Q_m \subset \mathbb{R}^2\}.$$

The regularity of the function f establishes the regularity of the surface Γ_m . Then each surface Γ_m is discretized with triangles

$$T_k = \bigcup_{i=1}^3 (x_{k_i}^*, f_m(x_{k_i}^*))$$

where $x_{k_i}^*$ are points in a bidimensional mesh defined on Q_m , and k_i is a representation of the node i of the triangle k in the global numeration.

With this procedure the multicrack is approximated by the union of piecewise triangular cracks, ie. $\Gamma_h = \cup_k T_k$ approximates Γ , denoting h the diameter of the triangles T_k . One should notice that the meshes of Q_m do not transfer directly their properties to the discretized surface $\tilde{\Gamma}_m$. For instance, a function f_m with high gradient might transform a triangle τ_k on Q_m into an almost degenerated triangle $T_k = f_m(\tau_k)$.

Associated to the triangulation we consider Lagrange finite elements \mathcal{P}_1 vanishing on the border of each Γ_m , which is an appropriated continuous approximation $\varphi_m \in H_{00}^{1/2}(\Gamma_m)$,

$$H_{00}^{1/2}(\Gamma_m) = \{\phi \in H^{1/2}(\Gamma_m) : \rho^{-1/2} \phi \in L^2(\Gamma_m)\}.$$

where ρ is equivalent to the distance to the border, ie. $\text{dist}(\cdot, \partial\Gamma)$. In Fig. 1 we present an example of triangulation for a double crack with non planar components. The triangulation is made in such a way that each interior node is associated with six adjacent triangles.

Having obtained the mesh we calculate the double integral in the sesquilinear form as the sum of double integrations over the element triangles, taking into account two different situations:

- (i) Non adjacent triangles \mapsto we consider numerical integration for both integrals using interior Gauss points.
- (ii) Adjacent triangles \mapsto we consider numerical integration in the first integral on a triangle T_i and for each Gauss point y_g we need to consider an analytical integration (cf. [1])

$$\int_{T_j} \Phi(x-y_g) (\mathbf{rot}_\Gamma \varphi(x) \cdot \mathbf{rot}_\Gamma \bar{\psi}(y_g) - k^2 \mathbf{n}_x(x) \cdot \mathbf{n}_y(y_g) \varphi(x) \bar{\psi}(y_g)) ds_x.$$

Note that φ and ψ basis functions of the discrete space. Since we consider interior Gauss points, there are only integration singularities when $T_i = T_j$. In the other situations we may proceed with numerical integration. The analytic calculation of the integral is what consumes most part of the computational time.

Through the resolution of the linear system associated to the discretization of the variational formulation, we obtain coefficients that define the approximation of φ as a linear combination of the basis functions. This way we may calculate an approximation of the far field amplitude through the formula

$$u_\infty(\hat{x}) = \frac{1}{4\pi} \sum_{m=1}^c \int_{\Gamma_m} \partial_{n_y} e^{-ik\hat{x}\cdot y} \varphi_m(y) ds_y,$$

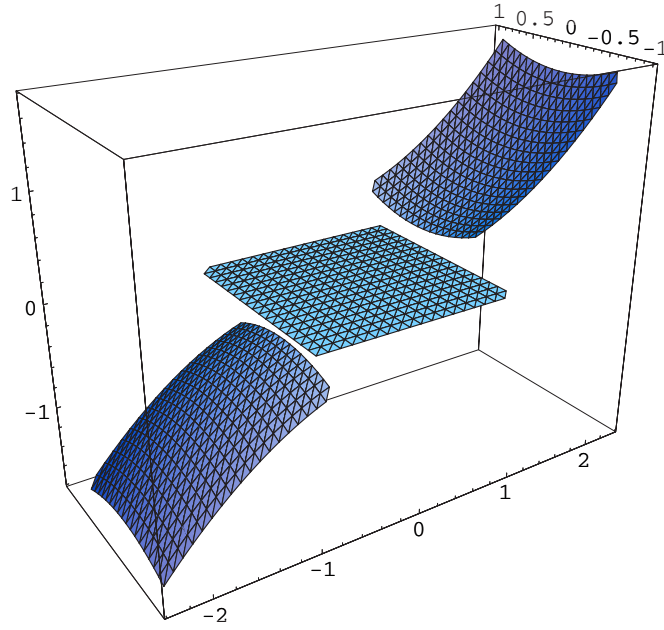


Figure 1: A mesh with 49 interior nodes, for each one of the three cracks.

using the integration rule with the Gauss points defined in each triangle approximating Γ_m .

Error Estimate

In $H_{00}^{1/2}(\Gamma)$ the norm is defined by

$$\|\phi\|_{1/2,00}^2 = \|\phi\|_{1/2}^2 + \|\rho^{-1/2}\phi\|_0^2$$

and in the plane crack case we may establish an $O(h^{3/2})$ convergence using Lagrange finite elements \mathcal{P}_1 .

In fact, considering a triangulation \mathcal{T}_h , let Π_h be the projection operator in the finite dimensional space defined by Lagrange finite elements of order k . Thus, $\Pi_h\phi$ is the interpolating function for $\phi \in H^{k+1}(\Gamma)$, and applying an interpolation inequality between $L^2 = H^0$ and H^1 Sobolev spaces we get

$$\|\phi - \Pi_h\phi\|_{1/2}^2 \leq C\|\phi - \Pi_h\phi\|_0\|\phi - \Pi_h\phi\|_1.$$

Using the interpolation estimates for Lagrange finite elements of order k

$$\|\phi - \Pi_h\phi\|_0 \leq Ch^{k+1}\|\phi\|_{k+1}, \quad \|\phi - \Pi_h\phi\|_1 \leq Ch^k\|\phi\|_{k+1},$$

we derive the estimate

$$\|\phi - \Pi_h\phi\|_{1/2} \leq Ch^{k+1/2}\|\phi\|_{k+1}.$$

In our case, since we are using \mathcal{P}_1 finite elements then $k = 1$, and without going through more technical details, this partially justifies the $O(h^{3/2})$ rate of convergence, when we have a regular setting and $\varphi \in H^2$, in particular for plane incident waves. This rate of convergence obtained for the density is then inherited by the calculations of the far field amplitude.

In the non planar crack case, such rate of convergence is diminished by the geometry approximation, since we are approaching the regular surfaces by piecewise triangular surfaces. Thus can expect a decrease of about $\frac{1}{2}$ in the convergence order, leading to an $O(h)$ approximation.

Numerical Simulations

We first present some numerical simulations concerning the convergence rate of the method. Calling $F(h)$ the evaluated far field amplitude with an h size mesh, the rate of convergence is evaluated numerically using three tests, using different h_{n-1}, h_n, h_{n+1} . Assuming that $E(h) = F - F(h) \approx Ch^p$, we obtain a value p approximated by p_n , the solution of the nonlinear equation

$$\frac{\|F(h_{n-1}) - F(h_n)\|}{\|F(h_n) - F(h_{n+1})\|} = \frac{h_{n-1}^{p_n} - h_n^{p_n}}{h_n^{p_n} - h_{n+1}^{p_n}} \tag{4}$$

and we obtain an approximated C by the value

$$C_n = \frac{\|F(h_{n-1}) - F(h_n)\|}{h_{n-1}^{p_n} - h_n^{p_n}}. \tag{5}$$

As a test we considered a plane wave with direction $d = (0, 0, -1)$, frequency $k = 2$ incident on three cracks, two of them not flat, as shown in Fig. 1. The cracks Γ_m are obtained as the graphs of $f_m(x, y) = (m - 2)\frac{1}{4}(1 + x^2 + y^2)$, for $(x, y) \in \alpha_m Q_m$ with $Q_m = [\frac{3}{2}(m - 2) - 1, \frac{3}{2}(m - 2) + 1] \times [-1, 1]$ and $\alpha_1 = \alpha_3 = 0.8, \alpha_2 = 1$.

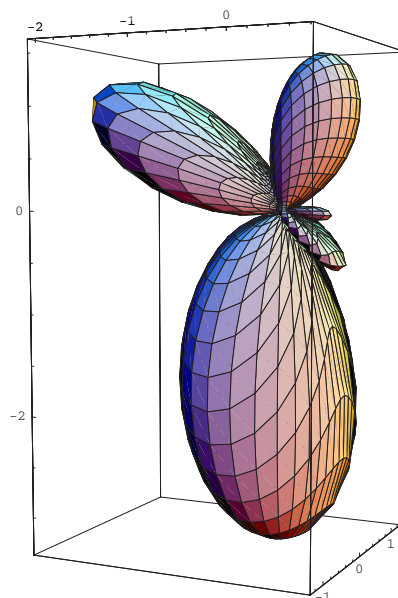


Figure 2: Modulus of the far field pattern generated by the 3 cracks with $d = (0, 0, -1)$ and $k = 2$.

The 3D plot of the far field modulus is presented in Fig. 2, and in Fig. 3 we present a cut of the 3D plots showing the convergence pattern using $M = 36$ observation points. Using those values, we obtained the estimates in Table 1.

Table 1. Convergence results.

n	h_n^Q	N	h_n	$\ F(h_n)\ _\infty$	$\frac{1}{M}\ F(h_n) - F(h_{n+1})\ _{l^2}$	p_n	C_n
1	0.5	26	0.782049	2.65687	0.0301858		
2	0.3333	74	0.533796	2.95359	0.0124467	1.680	0.947
3	0.25	146	0.405093	3.07630	0.00683649	1.432	0.923
4	0.2	242	0.326373	3.14346	0.00434551	1.301	0.888
5	0.1667	362	0.273261	3.18596	0.00301303	1.230	0.858
6	0.1429	506	0.235013	3.21532	0.00221712	1.177	0.831
7	0.125	674	0.206155	3.23685	0.00170128	1.146	0.812
8	0.1111	866	0.183609	3.25332			

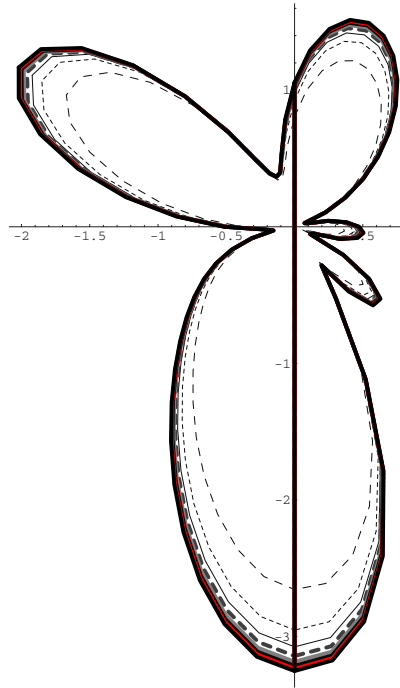


Figure 3: Convergence of the far field modulus (cuts of the 3D pattern for several h).

In Table 1 we present the results for several meshes, with h_n^Q representing the step size on each square Q_m that leads to a mesh discretization of Γ_m with diameter h_n (fourth column). The number N represents the number of interior nodes and therefore the dimension of the rigid matrix $N \times N$. In the fifth column we see the convergence of the far field values $\|F(h_n)\|_\infty = \max_{j=1,\dots,M} |\tilde{u}_\infty(d_j)|$, where d_j represent the $M = 36$ equally angular spaced observation directions, and $|\tilde{u}_\infty(d_j)|$ the far field modulus taken on a cut of the sphere (as presented in Fig. 2). In the next column we show the l^2 average of the the difference between two successive mesh sizes, ie. $\frac{1}{M} \|F(h_n) - F(h_{n+1})\|_{l^2}$ and in the other two columns we present the instant estimate of the rate of convergence p_n as given by eq.(4) and C_n as given by eq.(5).

It is worth noting that the convergence rate becomes close to 1 as predicted in the error estimate section. It starts closer to 1.5 but it decreases almost to 1, revealing the effect of the geometry approximation (piecewise triangular shape) in decreasing the convergence rate.

On the other hand, as we may see in Fig. 2, where we plotted the curves from $n = 1$ (dashed) to $n = 8$ (bold), the general aspect of the far field pattern is obtained even with considerably large h_n . In fact already with h_4 it becomes to difficult to see a difference with the results produced by the smaller h_8 . Since for h_8 we need to compute the integrals for a 866×866 matrix, against a 242×242 matrix with h_4 , there is no significant advantage in the given example to consider higher approximations. We should note however that the results became worst when the frequency is higher and also when we are dealing with more complex crack shapes. In those situations a smaller h must be considered.

In the next simulations, keeping the plane crack Γ_2 fixed, we show the influence on the far field of the growing area of the other two cracks, by increasing the parameter $\alpha_1 = \alpha_3 = \alpha$ from 0 to 1 (recall that this parameter defines the support of the graph). The case $\alpha = 0$ corresponds to consider only the flat crack Γ_2 .

In Fig.4 we show the far field patterns obtained for $\alpha = 0.01, 0.4, 0.6$. (from left to right). In this three simulations, the effect of the small cracks Γ_1 and Γ_3 becomes only clearly noticed with $\alpha = 0.6$, where a new lobe is starting to be formed.

The effect of the Γ_1 and Γ_3 becomes clear when we increase α to 0.8 or to 1.0, as we may see in Fig. 5 (center and right). In this situation the far field pattern can be seen as a mixture of the far field obtained for an oblique plane crack with $f_2(x) = x_1$, (Fig.5 - left) and the far field obtained for $f_2(x) = 0$ (Fig. 4 - left).

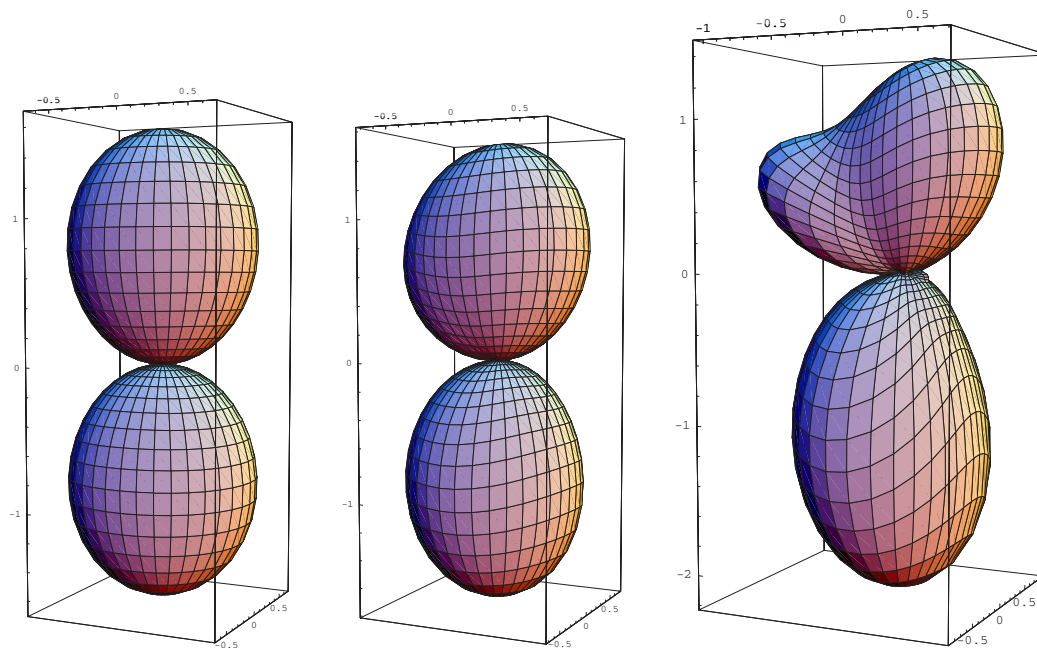


Figure 4: Far field modulus increasing $\alpha = 0.01, 0.4, 0.6$ (from left to right).

When α increases the overall shape of the three cracks can be roughly approximated by the oblique crack. This roughly justifies the increase of the contribution of the corresponding reflection lobes of the oblique crack and the decrease of the contribution given by the *horizontal* crack Γ_2 .

Conclusions

In this work we have shown that the boundary finite element method provides good approximations of the scattered field by several cracks. We have presented several numerical simulations confirming the expected rate of convergence, and aiming detection criteria, we started to investigate the effect on the far field generated by the presence of other cracks. It was also observed that this method is not adequate if we consider a significant number of cracks, since there will be a compromise between the precision and computational time required by an extensive meshing. However, it was noticed that the method presented good results even with a small number of interior nodes. A more careful study on the difference between the total scattering and the sum of independent scatterers may provide criteria for crack detection.

Acknowledgements. This work is partially supported by FCT through the program POCTI-FEDER and project POCTI/MAT/34735/2000.

References

- [1] C.J.S. Alves and T. Ha Duong, Numerical resolution of the boundary integral equations for elastic scattering by a plane crack, *Int J. Num. Meth. Eng.*, **38**, pp.2347–2371 (1995).
- [2] C.J.S. Alves and T. Ha Duong, On inverse scattering by screens, *Inverse Problems*, **13**, pp.1161–1176 (1997).
- [3] C.J.S. Alves, B. Pereira and P. Serranho, Scattering by cracks: Numerical simulations using a boundary finite element method, in *Boundary Elements XXIV* (Ed: C. A. Brebbia, A. Tadeu, V. Popov), WIT Press, pp. 35-44 (2002).

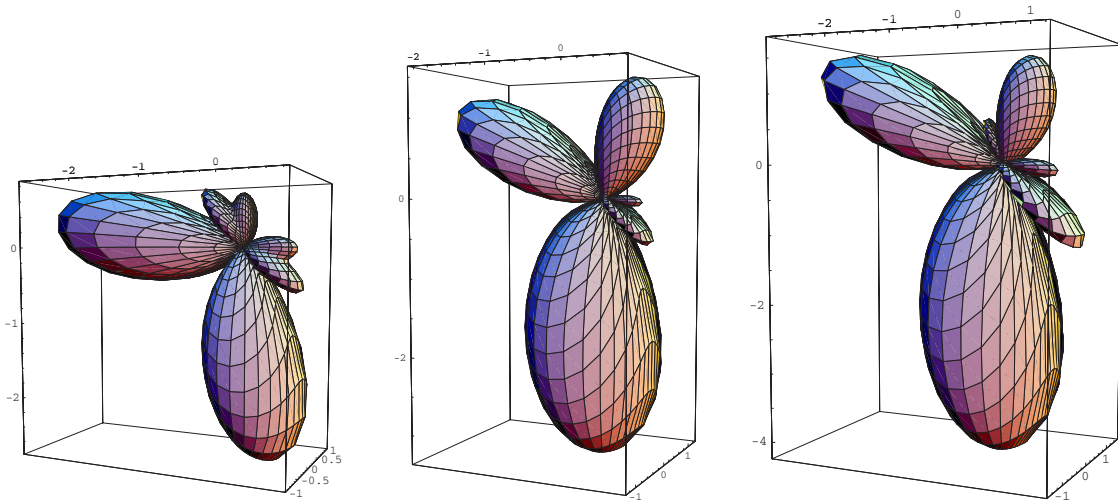


Figure 5: Far field modulus for an oblique plane crack (left) and with $\alpha = 0.8, 1.0$. (center and right)

- [4] H. Ammari and P. Ferreira, Numerical methods for the scattering by gratings at high frequencies. *Math. Meth. Appl. Sci.* **20**, pp. 1531-1549 (1997).
- [5] M. Bonnet, Regularized BIE formulations for first- and second-order shape sensitivity of elastic fields. *Comput. & Structures* **56**, pp.799–811 (1995).
- [6] C.J. Bouwkamp, Diffraction theory. *Reports on Progress in Physics* **17**, pp.35–100, (1954).
- [7] D. Colton and R. Kress, *Inverse acoustic and electromagnetic scattering theory*, Springer-Verlag, 2nd. ed. (1998).
- [8] T. Ha Duong, On the boundary integral equations for the crack opening displacement of flat cracks, *Int. Eq. Op. Th.*, pp.427-453 (1992).
- [9] M.A. Hamdi, Une formulation variationnelle par équations intégrales pour la résolution de l'équation de Helmholtz avec des conditions aux limites mixtes, *C.R.A.S.II* **292**, pp.17–20, (1981).
- [10] C. Johnson and J.C. Nédélec, On the coupling of boundary integral and finite element methods, *Math. Comp.* **35**, 1063 –1079 (1980).
- [11] D.S. Jones, A new method for calculating scattering with particular reference to the circular disc. *Comm. Pure Appl. Math.* **9**, pp.713–746, (1956).
- [12] P.A. Martin and G.R. Wickham, Diffraction of elastic waves by a penny-shaped crack: analytical and numerical results. *Proc. Roy. Soc. Lond.*, **A 390**, pp 91–129 (1983).
- [13] P.A. Martin and F.J. Rizzo, On boundary integral equations for crack problems. *Proc. Roy. Soc. Lond.*, **A 421**, pp.341–355, (1989).
- [14] J. C. Nédélec, Curved finite element methods for the solution of singular integral equations on surfaces in \mathbb{R}^3 . *Comput. Methods Appl. Mech. Engrg.* **9**, 191-216 (1977).
- [15] F. Penzel, Mixed Fourier boundary element methods for computing time-harmonic scattering fields on screens, *Math. Nachr.* **175**, pp.269–324, (1995).

On the Implementation of the Two Dimensional Dual Boundary Element Method for Crack Problems

L. P. C. P. F. Almeida¹, L. Palermo Jr.¹

¹Universidade Estadual de Campinas, Faculdade de Engenharia Civil, Brasil,
lpedro@fec.unicamp.br. leandro@fec.unicamp.br.

Keywords: Dual Boundary Element Method, Linear Elastic Fracture Mechanics, Stress Intensity Factor.

Abstract. The implementation of the two-dimensional dual boundary element method for crack problems is studied in the evaluation of stress intensity factors. The analysis employed continuous or discontinuous flat boundary elements on the crack surface. All nodal parameters were positioned at the ends of the elements and approximated with linear or quadratic shape functions. The collocation points were shifted to the element inside for discontinuous or continuous boundary elements. The near-tip displacement extrapolation was used to assess the stress intensity factors. The obtained results were compared with solutions available from the literature to evaluate this strategy.

Introduction

The dual boundary element method (DBEM) is an efficient technique to analyze crack problems when compared with other strategies like the displacement discontinuity method, the crack Green's function method and the subregions method. Bueckner [1] used the dual integral equations in the fracture mechanics, Watson [2] used them in the boundary element method (BEM), Hong and Chen [3] presented the theoretical bases of the DBEM and Aliabadi et alli [4, 5, 6] presented a lot of studies showing the efficiency of the DBEM for crack problems.

The dual equations of the method are the displacement and the traction boundary integral equations. When the displacement is applied on one of the crack surfaces and the traction equation on the other, general mixed-mode crack problems can be solved with a single region formulation. Although the integration path is still the same for coincident points on the crack surfaces, the respective boundary integral equations are now distinct. The collocation point to perform the traction boundary integral equation and the analytic evaluation of its singular integrals are the essential features of the formulation.

This study used the strategy of the treatment of the finite part integrals detailed in [4]. However, the use of boundary elements with parameters positioned at their ends carried to shift the collocation points to the element inside where the continuity condition required to the traction boundary integral equation is satisfied. This changing on the technique presented in [4] has allowed the use of continuous or discontinuous flat elements on the crack surface. Furthermore, the linear shape functions were employed to approach the boundary parameters beyond the well-known quadratic functions and the obtained results were compared with solutions available from the literature to evaluate this strategy.

The Dual Boundary Integral Equations

The DBEM uses the displacement and the traction boundary integral equations. The presentation of the boundary equation for displacement is well known. A general expression for the displacement at the collocation point p' is written next using Cartesian coordinates and without considering the body forces:

$$c_{ij}(p')u_j(p') + \int_{\Gamma} T_{ij}(p', p)u_j(p)d\Gamma(p) = \int_{\Gamma} U_{ij}(p', p)t_j(p)d\Gamma(p) \quad (1)$$

$U_{ij}(p', p)$ and $T_{ij}(p', p)$ correspond to the displacement and the traction, respectively, in the direction j at the boundary point p due to a singular load in the direction i at the collocation point p' according to the Kelvin solution for two dimensional problems; $u_j(p)$ and $p_j(p)$ are the displacement and the traction, respectively, at the boundary; the tensor c_{ij} is given by $\delta_{ij}/2$ when the collocation point is placed on a smooth boundary and equals to 1 for internal points (δ_{ij} is the Kronecker delta).

The integrals of eq (1) are regular for internal points. Nevertheless, the integrals exhibit singularities of order $1/r$ and $\ln(1/r)$ for points on the boundary and the Cauchy principal-value integral is used to compute the

boundary integral containing $1/r$. The condition to use the displacement equation for collocation points on the boundary is the continuity of the displacement at p' , which remains valid for collocation points placed on the boundary nodes or shifted to the element inside.

The integral equation for stress is obtained by differentiation of the displacement boundary integral equation for internal points. The existence of differentiation carries to need the continuity of the derivative of the displacement function at the collocation point (C^1 function). The stress BIE for the internal point p' is:

$$\sigma_{ij}(p') + \int_{\Gamma} S_{kij}(p', p) u_k(p) d\Gamma(p) = \int_{\Gamma} D_{kij}(p', p) t_k(p) d\Gamma(p) \quad (2)$$

$S_{kij}(p', p)$ and $D_{kij}(p', p)$ are linear combinations of derivatives of $T_{ij}(p', p)$ and $U_{ij}(p', p)$ according to the isotropic tensor of the constitutive relations. The integrals of the eq (2) are regular for internal points. However, S_{kij} exhibits a hypersingularity of the order $1/r^2$ and D_{kij} exhibits a strong singularity of the order $1/r$ when the internal point approaches to the boundary and the distance r tends to zero. Assuming continuity of both strains and tractions at p' , the limiting process produces improper integrals and jump terms in strains and tractions. The stress boundary integral at the boundary point p' on a smooth boundary is:

$$\frac{1}{2} \sigma_{ij}(p') + \int_{\Gamma} S_{kij}(p', p) u_k(p) d\Gamma(p) = \int_{\Gamma} D_{kij}(p', p) t_k(p) d\Gamma(p) \quad (3)$$

The Hadamard and the Cauchy principal-value integrals are used to compute integrals of eq (3) containing $1/r^2$ (left member) and $1/r$ (right member), respectively. The traction BIE is obtained from eq (3). The obtained stress tensor at the point p' is multiplied by direction cosines of the normal at this point to get tractions and the following equation is obtained considering a smooth boundary at the collocation point and $n_i(p')$ equal to the direction cosines of the unit normal to the boundary at p' .

$$\frac{1}{2} t_j(p') + n_i(p') \int_{\Gamma} S_{kij}(p', p) u_k(p) d\Gamma(p) = n_i(p') \int_{\Gamma} D_{kij}(p', p) t_k(p) d\Gamma(p) \quad (3b)$$

Treatment of Finite-Part Integrals

The improper integrals can be handled with the classical singularity-subtraction method and the natural definition of ordinary finite-part integrals is reached. The regular part of the integrand can be expressed as a Taylor's expansion in the vicinity of the collocation point. The singularity can be isolated if a sufficient number of terms of the expansion are subtracted from the regular part of the integrand and then added back. Analytical expressions can be used to evaluate the singular integral and Gauss-Legendre scheme can be employed for the regular integral. The flat boundary elements used in this study had their nodal parameters positioned at the ends. The existence of the fixed position for element nodes carried to consider shape functions with same expressions for continuous, discontinuous or mixed boundary elements. The local parametric co-ordinate ξ is defined in the range $(-1, 1)$ and the collocation point position is ξ' . The displacement components u_j are approximated in the local co-ordinate in terms of nodal values u_j^n . The first order finite-part integral of eq (1) expressed in the local co-ordinate ξ is:

$$\int_{\Gamma_e} T_{ij}(p', p) u_j(p) d\Gamma(p) = u_j^n \int_{-1}^{+1} \frac{f_{ij}^n(\xi)}{\xi - \xi'} d\xi \quad (4)$$

The regular function $f_{ij}^n(\xi)$ is given by the product of the fundamental solution, the shape function, the Jacobian of the co-ordinate transformation and the term $(\xi - \xi')$. The integral in the right-hand side of eq (4) can be transformed with the aid of the first term of Taylor's expansion of the function f_{ij}^n around the collocation point p' , which position is ξ' . The development is similar to that presented in [4] but using the collocation point position ξ' , which does not correspond to the node position in this study.

$$\int_{-1}^{+1} \frac{f_{ij}^n(\xi)}{\xi - \xi'} d\xi = \int_{-1}^{+1} \frac{f_{ij}^n(\xi) - f_{ij}^n(\xi')}{\xi - \xi'} d\xi + f_{ij}^n(\xi') \int_{-1}^{+1} \frac{d\xi}{\xi - \xi'} \quad (5)$$

A similar procedure to that presented in [4] was applied to the second order finite part integral but using the collocation point position ξ' in the Taylor's expansion.

Boundary Elements and Internal Collocation Points

The geometry and boundary field variables are described by a piece-wise continuously differentiable approximation when a general boundary element mesh is defined. The Cauchy and the Hadamard principal-value integrals are equivalent to finite-part integrals of first and second order, respectively. The necessary condition for existence of the finite-part integrals can be satisfied when internal points of the element are used as collocation points and without associating them to the element nodes. The strategy of the collocation points placed inside the boundary elements with fixed nodes at the ends is analyzed in this study. Furthermore, linear shape functions were tested beyond the quadratic functions. The collocation point positions adopted in the numerical implementation used the condition of the last node of the element. A discontinuous element was assumed by the computer code when the final node was defined as double and continuous in case of not. The collocation point positions for quadratic elements were: i) $\xi' = -0.67$ and $\xi' = +0.67$ for continuous elements; ii) $\xi' = -0.67$, $\xi' = 0$ and $\xi' = +0.67$ for discontinuous elements.

Two situations were considered in the analysis when linear shape functions were employed and the collocation point positions were: i) $\xi' = -0.67$ for continuous elements; ii) $\xi' = -0.67$ and $\xi' = +0.67$ for discontinuous elements. i) $\xi' = 0$ for continuous elements; ii) $\xi' = 0$ and $\xi' = +0.67$ for discontinuous elements.

It is necessary to note that the final node condition to define the collocation point position carried to the following situations: a) Mixed element with the final node defined as double has positions equal to the discontinuous element; b) Mixed element with the first node defined as double has positions equal to the continuous element. The strategy to place the collocation point can be extended to the boundary portion not related to the crack surface without additional care. Nevertheless, the integration procedure has to identify opposite elements on the crack surface where analytical expressions should be employed in the computation of the BIE. Furthermore, the rigid body condition was not used in the computation of the diagonal terms, which were obtained directly using the collocation point position on each element and the corresponding shape function adopted in the analysis.

The Stress Intensity Factor Evaluation

The elastic field is defined by an infinite series expansion in the neighborhood of the crack tip and it can be decoupled in the components: Mode I and Mode II. The first term of the stress series is singular and the remaining terms give zero stresses. Consider a polar coordinate system (r, θ) centered at the crack tip, such that the crack surfaces could be defined with $\theta = \pm\pi$. The displacement field on the crack surface is written next when only the first term of the William's expansion is considered:

$$u_2(\theta = \pi) - u_2(\theta = -\pi) = \frac{\kappa + 1}{\mu} K_I \sqrt{\frac{r}{2\pi}} \tag{10}$$

$$u_1(\theta = \pi) - u_1(\theta = -\pi) = \frac{\kappa + 1}{\mu} K_{II} \sqrt{\frac{r}{2\pi}} \tag{11}$$

The stress intensity factors for deformation modes II and I are K_{II} and K_I , respectively; the parameter κ is equal to $3-4\eta$; for plane strain problems $\eta = \nu$ and for plane stress problems $\eta = \nu/(1+\nu)$. The near-tip displacement extrapolation works with eqs (10) and (11) to obtain the stress intensity factors when the displacements are known. The Figure 2 shows two situations where two opposite elements (a linear and a quadratic) sharing the crack tip at nodes B and C. The linear and the quadratic elements have lengths equal to l and $2l$, respectively.

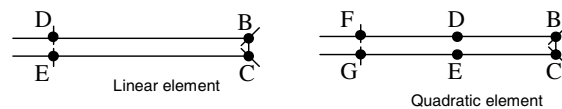


Figure 2: Crack tip at points B and C.

The stress intensity factors obtained from displacements is given by:

Linear element: using displacements at nodes D-E (end of the element) or quadratic elements: using displacements D-E (middle of the element):

$$K_I^{DE} = (u_2^D - u_2^E) \frac{\mu}{\kappa + 1} \cdot \sqrt{2} \cdot \sqrt{\frac{\pi}{l}} \tag{12}$$

$$K_{II}^{DE} = (u_1^D - u_1^E) \frac{\mu}{\kappa+1} \sqrt{2} \sqrt{\frac{\pi}{l}} \tag{13}$$

Quadratic elements: using F-G (end of the element):

$$K_I^{FG} = (u_2^F - u_2^G) \frac{\mu}{\kappa+1} \sqrt{2} \sqrt{\frac{\pi}{l}} \tag{14}$$

$$K_{II}^{FG} = (u_1^F - u_1^G) \frac{\mu}{\kappa+1} \sqrt{2} \sqrt{\frac{\pi}{l}} \tag{15}$$

A linear extrapolation was carried out from the nodes D-E and F-G to the crack tip yields

$$K_I = \left[4(u_2^D - u_2^E) - \sqrt{2}(u_2^F - u_2^G) \right] \frac{\mu}{\kappa+1} \sqrt{\frac{\pi}{l}} \tag{16}$$

$$K_{II} = \left[4(u_1^D - u_1^E) - \sqrt{2}(u_1^F - u_1^G) \right] \frac{\mu}{\kappa+1} \sqrt{\frac{\pi}{l}} \tag{17}$$

Numerical Examples

Three cases were studied using linear and quadratic boundary elements. The number of the linear elements was the double of the quadratic elements to consider a fixed position for nodes independently of the adopted shape function.

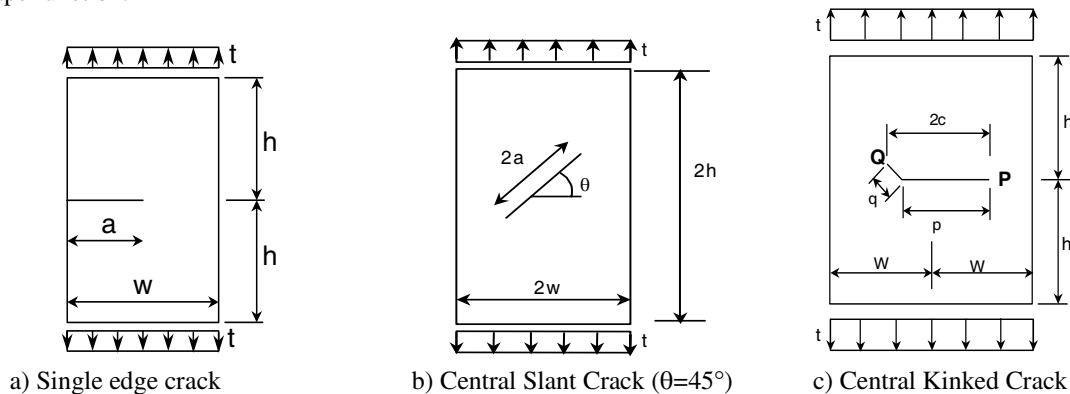


Figure 3: Analyzed cracks

A rectangular plate containing a single horizontal edge crack shown in Figure 3a was analyzed. The crack length is a, the plate width is w and the height is 2h. A uniform traction in the height direction was symmetrically applied at the ends. Results were obtained for the ratio h/w equals to 0.5. Five ratios a/w were considered: 0.2, 0.3, 0.4, 0.5 and 0.6. The used meshes were: 24 quadratic boundary element plus 4 quadratic elements on each crack surface (32 B.E.); 48 linear elements plus 8 elements on each crack surface (64 B.E.).

Table 1: Results for $K_I/(t\sqrt{\pi.a})$ with linear elements

a/w	Obtained results for Mode I						Civelek (1982)	Portela(1992)
	DE						DE	DE
	A		B		C			
	ksic=0.	ksic=-2./3.	ksic=0.	ksic=-2./3.	ksic=0.	ksic=-2./3.		
0,2	1,558	1,558	1,669	1,507	1,656	1,496	1,488	1,566
0,3	1,942	1,946	2,201	1,880	2,200	1,880	1,848	1,962
0,4	2,475	2,468	2,830	2,384	2,830	2,383	2,324	2,230
0,5	3,241	3,227	3,739	3,114	3,738	3,114	3,010	3,268
0,6	4,538	4,508	5,293	4,355	5,292	4,355	4,152	4,580

Tables 1 and 2 present results for linear and quadratic elements, respectively. The sets A, B and C correspond to following meshes: A) Discontinuous elements on each crack surface and a discontinuous element on each side of the external boundary reaching the crack; B) Continuous elements on each crack surface (a double node at the crack tip) and a discontinuous element on each side of the external boundary reaching the crack; C) Continuous elements on each crack surface (a double node at the crack tip) and on the external boundary (double nodes at the corners and including those where the external boundary reaches the crack). The column labeled in Table 1 by: “ksic=0.67” corresponds to internal positions ($\xi'=-0.67$ for

continuous elements) and ($\xi'=-0.67$ and $\xi'=+0.67$ for discontinuous elements); and that with $ksic=0$ corresponds to internal positions ($\xi'=0$ for continuous elements) and ($\xi'=0$ and $\xi'=+0.67$ for discontinuous elements). The stress intensity factors in the column labeled by DE were obtained with eq (12) and those labeled DE-FG with eq (16).

Table 2: Results for $K_I/(t\sqrt{\pi.a})$ with quadratic elements

a/w	Obtained results for Mode I						Civelek (1982)	Portela (1992)	
	A		B		C			DE	DE-FG
	DE	DE-FG	DE	DE-FG	DE	DE-FG			
0,2	1,520	1,582	1,522	1,594	1,557	1,631	1,488	1,566	1,618
0,3	1,959	2,024	1,957	2,035	1,957	2,035	1,848	1,962	2,014
0,4	2,495	2,555	2,503	2,579	2,496	2,571	2,324	2,230	2,537
0,5	3,268	3,313	3,300	3,364	3,292	3,357	3,010	3,268	3,292
0,6	4,586	4,591	4,675	4,705	4,671	4,701	4,152	4,580	4,558

A rectangular plate containing a central slant crack shown in Figure 3b was analyzed. The crack length is $2a$, the plate width is $2w$ and the height is $2h$. A uniform traction in the height direction was symmetrically applied at the ends. Results were obtained for the ratio h/w equals to 2. Five ratios a/w were considered: 0.2, 0.3, 0.4, 0.5 and 0.6. The boundary meshes were: 24 quadratic boundary element plus 6 quadratic elements on each crack surface (36 B.E.); 48 linear elements plus 12 elements on each crack surface (72 B.E.). Table 3 and 4 present the obtained results using linear and quadratic elements. The sets A and B correspond to following meshes: A) Discontinuous elements on each crack surface; B) Continuous elements on each crack surface (a double node at the crack tip). The obtained results with linear elements used “ $ksic=0.67$ ”, which corresponded to internal positions ($\xi'=-0.67$ for continuous elements) and ($\xi'=-0.67$ and $\xi'=+0.67$ for discontinuous elements). The obtained stress intensity factor K_I in Table 3 were obtained with eq (12) for linear elements and for quadratic elements. The obtained stress intensity factor K_{II} in Table 4 were obtained with eq (13) for linear elements and for quadratic elements.

Table 3: Results for $K_I/(t\sqrt{\pi.a})$

a/w	Obtained results for Mode I				Murakami (1987)	Portela (1992)	
	DE						DE
	linear element		quadratic element				
	A	B	A	B			
0,2	0,530	0,513	0,531	0,528	0,518	0,531	
0,3	0,553	0,535	0,555	0,551	0,541	0,554	
0,4	0,586	0,567	0,588	0,585	0,572	0,588	
0,5	0,628	0,608	0,632	0,628	0,612	0,632	
0,6	0,682	0,660	0,688	0,684	0,661	0,686	

Table 4: Results for $K_{II}/(t\sqrt{\pi.a})$

a/w	Obtained results for Mode II				Murakami (1987)	Portela (1992)	
	DE						DE
	linear element		quadratic element				
	A	B	A	B			
0,2	0,519	0,502	0,519	0,516	0,507	0,519	
0,3	0,528	0,511	0,528	0,525	0,516	0,528	
0,4	0,541	0,524	0,541	0,538	0,529	0,541	
0,5	0,558	0,540	0,588	0,554	0,546	0,558	
0,6	0,579	0,561	0,579	0,576	0,567	0,579	

Table 5: Results at P for $K_I/(t\sqrt{\pi.c})$

b/a	Obtained results for Mode I at P				Murakami (1987)	Portela (1992)	
	DE						DE
	linear element		quadratic element				
	A	B	A	B			
0,2	1,021	0,988	1,021	1,015	0,995	1,021	
0,4	1,018	0,985	1,018	1,012	0,990	1,018	
0,6	1,017	0,983	1,016	1,011	0,986	1,017	

A rectangular plate containing an internal kinked crack shown in Figure 3c was analyzed. One of the segments of the crack is horizontal with length p while the other segment makes an angle of 45 degrees with the horizontal and has length q ; the horizontal projection of the total crack is given by $2c=p+0.5(2q)^{0.5}$. The kink of the crack is at the center of the plate, the plate width is $2w$ and the height is $2h$. Three ratios b/a were considered: 0.2, 0.4 and 0.6 for $p/w=0.1$. The stress intensity factors were obtained for both tips. The used

meshes were: 30 quadratic boundary element plus 5 quadratic elements on each horizontal crack surface and 4 quadratic elements on each inclined crack surface (48 B.E.); 60 linear elements plus 10 quadratic elements on each horizontal crack surface and 8 quadratic elements on each inclined crack surface (96 B.E.). The sets A and B correspond to following meshes: A) Discontinuous elements on each crack surface; B) Continuous elements on each crack surface (a double node at the crack tip and at the center of the crack).

Table 6: Results at P for $K_{II}/(t\sqrt{\pi.c})$

b/a	Obtained results for Mode II at P				Murakami (1987)	Portela (1992)
	DE					
	linear element		quadratic element			
	A	B	A	B		
0,2	0,030	0,029	0,030	0,030	0,028	0,030
0,4	0,036	0,035	0,035	0,035	0,033	0,036
0,6	0,032	0,032	0,031	0,031	0,030	0,032

Table 7: Results at Q for $K_{I}/(t\sqrt{\pi.c})$

b/a	Obtained results for Mode I at Q				Murakami (1987)	Portela (1992)
	DE					
	linear element		quadratic element			
	A	B	A	B		
0,2	0,628	0,636	0,633	0,596	0,598	0,634
0,4	0,600	0,606	0,603	0,569	0,574	0,603
0,6	0,593	0,600	0,596	0,562	0,568	0,595

Table 8: Results at Q for $K_{II}/(t\sqrt{\pi.c})$

b/a	Obtained results for Mode II at Q				Murakami (1987)	Portela (1992)
	DE					
	linear element		quadratic element			
	A	B	A	B		
0,2	0,586	0,590	0,589	0,556	0,557	0,589
0,4	0,635	0,639	0,639	0,606	0,607	0,637
0,6	0,656	0,661	0,660	0,628	0,627	0,659

Conclusion

The obtained results using internal collocation points and fixed nodes at the ends of the elements were close to those presented in [4] which used discontinuous elements with internal nodes. The obtained results with quadratic shape functions were better when discontinuous elements. Nevertheless, the results obtained with continuous element were close to those with discontinuous elements. The collocation point position on linear elements had influence on the results. Better results could be obtained when the collocation point position was -0.67 and $+0.67$. Continuous elements improved the results with reference to discontinuous elements. Finally, the obtained numerical results were close to the obtained values from the literature [7, 8].

Acknowledgements - Authors are grateful to CAPES due to the support for the development of this study.

References

- [1] Bueckner, H.F., Field singularities and related integral representations, Mechanics of Fracture, Nordhoff, Leyden, The Netherlands, 1973
- [2] Watson, J.O., Hermitian cubic and singular elements for plane strain, Developments in Boundary Element Methods 4, Elsevier Applied Science Publishers, Barking, UK, 1986
- [3] Hong, H. & Chen, J., 1988, Derivations of integral equations of elasticity, Journal Engineering Mechanics ASCE, 114, pp. 1028-1044.
- [4] Portela, A., Aliabadi, M. H. e Rooke, D. P., 1992, The Dual Boundary Element Method: Effective implementation for crack problems, Int. Journ. Num. Meth. Eng., vol. 33, pp. 1269-1287.
- [5] Mi Y and Aliabadi MH, Dual boundary element method for three dimensional fracture mechanics analysis, Eng. Anal. with Boundary Element, 10, 161-171, 1992
- [6] Aliabadi MH, Brebbia, CA, (eds), Adv. in Bound. Elem. for Fract. Mech., Elsevier Publishers, 1993.
- [7] Civelek, M. B. & Erdogan, F., 1982, Crack problems for a rectangular sheet and an infinite strip, International Journal of Fracture, vol.19 , pp.139-159.
- [8] Murakami, Y., 1987, Stress Intensity Factors Handbook, Pergamon Press, Oxford.

Boundary element analysis of three-dimensional mixed-mode cracks via the interaction integral

A. Cisilino and J. Ortiz

Welding and Fracture Division, INTEMA, University of Mar del Plata – CONICET
Av. Juan B. Justo 4302 (7600) Mar del Plata, Argentina. cisilino@fi.mdp.edu.ar

Keywords: fracture mechanics, energy domain integral, interaction integral, boundary elements

Abstract. A three-dimensional Boundary Element Method (BEM) implementation of the interaction integral methodology for the numerical analysis of mixed-mode three-dimensional cracks is presented in this paper. The interaction integral is evaluated from a domain representation naturally compatible with the BEM, since stresses, strains and derivatives of displacements at internal points can be evaluated using the appropriate boundary integral equations. Special emphasis is put in the selection of the auxiliary function that represents the virtual crack advance in the domain integral. This is found to be a key feature to obtain reliable results at the intersection of the crack front with free surfaces. Several examples are analysed to demonstrate the efficiency and accuracy of the implementation.

1. Introduction

Evaluation of fracture parameters is usually the purpose of carrying out a numerical model of a crack problem. The J -integral as devised by Rice[1] characterizes the crack driving force for two-dimensional problems, therefore for general three-dimensional cases involving cracks of arbitrary shape; an alternative form for J is needed. Three basic schemes have evolved for the numerical computation of the J -integral in three dimensions: virtual crack extension methods, generalization of Rice's contour integral and domain integral methods [2,3,4].

The Energy Domain Integral (EDI) has shown well suited for three-dimensional BEM analysis [5]. The EDI is versatile and efficient and relatively simple to implement numerically. To develop the domain integral the EDI incorporates an auxiliary function q , which can be interpreted as a virtual crack front advance. On the other hand, the interaction or M_I -integral methodology originally proposed by Chen and Shield [6] has emerged as an efficient methodology for decoupling the J -integral for mixed-mode cracks. This is based on the superposition of two equilibrium states, given by the actual problem and a set of auxiliary known solutions. The M_I -integral methodology has been implemented using BEM for two-dimensional cracks by Miyazaki et al[7].

This work presents a BEM domain formulation of the M_I -integral for the computation of mixed-mode stress intensity factors along three-dimensional crack fronts. Special emphasis is put in the appropriate selection of the auxiliary function q , which was found to be a key feature to obtain reliable results at the intersection of the crack front with free surfaces.

2. The Interaction Integral

The interaction or M_I -integral is based on the principle of superposition. Let us consider two equilibrium states with field variables denoted by the superscripts (1) and (2), respectively. Superposition of the two equilibrium states leads to another one, (1+2). Then the stress intensity factors $K_j^{(1+2)}$ can be written as

$$K_j^{(1+2)} = K_j^{(1)} + K_j^{(2)} \quad (j = I, II, III). \quad (1)$$

The stress intensity factors can be related to the J -integral in a plain strain condition as follows:

$$J = J_I + J_{II} + J_{III} = \frac{1}{E} (K_I^2 + K_{II}^2) + \frac{K_{III}^2}{2\mu} \quad (2)$$

where E is the Young's and μ is the shear modulus. Using Eq.(2), the J -integral for the superimposed state (1+2) can be written as

$$\begin{aligned}
J^{(1+2)} &= \frac{1}{E} \left[(K_I^{(1+2)})^2 + (K_{II}^{(1+2)})^2 \right] + \frac{(K_{III}^{(1+2)})^2}{2\mu} \\
&= J^{(1)} + J^{(2)} + \frac{2}{E} (K_I^{(1)} K_I^{(2)} + K_{II}^{(1)} K_{II}^{(2)}) + \frac{K_{III}^{(1)} K_{III}^{(2)}}{\mu}.
\end{aligned} \tag{3}$$

Then, the M_I -integral is defined as

$$\frac{2}{E} (K_I^{(1)} K_I^{(2)} + K_{II}^{(1)} K_{II}^{(2)}) + \frac{K_{III}^{(1)} K_{III}^{(2)}}{\mu} = J^{(1+2)} - J^{(1)} - J^{(2)} = M_I. \tag{4}$$

The M_I -integral can be expressed using a domain representation using the energy domain integral approach [2]

$$M_I = \int_V (\sigma_{ij}^{*(1)} u_{j,k}^{*(2)} + \sigma_{ij}^{*(2)} u_{j,k}^{*(1)} - \sigma_{ij}^{*(1)} \varepsilon_{ij}^{*(2)} \delta_{ki}) q_{,i} dV. \tag{5}$$

where the auxiliary function q can be interpreted as a virtual crack front advance, and the integration volume V consists in a tubular domain surrounding a crack segment.

For the decoupling the mixed-mode stress intensity factors the problem under consideration is selected as equilibrium state (1), so that the field variables $\sigma_{ij}^{*(1)}$ and $u_{j,k}^{*(1)}$ will be obtained in this work from the results of a boundary element analysis. On the other hand, the well-known plain-strain solutions for the asymptotic crack-tip fields with prescribed stress intensity factors K_I , K_{II} and K_{III} , are selected as equilibrium state (2). Then the field variables related with the equilibrium state (2), $\sigma_{ij}^{*(2)}$, $u_{j,k}^{*(2)}$ and $\varepsilon_{ij}^{*(2)}$ are calculated from these asymptotic solutions. Finally the M_I -integral defined in Eq.(5) can be calculated, using the field variables related with the equilibrium states (1) and (2). By using three sets of asymptotic solutions, ($K_I^{(2)} = 1$, $K_{II}^{(2)} = 0$, $K_{III}^{(2)} = 0$), ($K_I^{(2)} = 0$, $K_{II}^{(2)} = 1$, $K_{III}^{(2)} = 0$) and ($K_I^{(2)} = 0$, $K_{II}^{(2)} = 0$, $K_{III}^{(2)} = 1$), it is possible to obtain the stress intensity factor solutions for individual modes from Eq.(4) as follows:

$$K_I^{(1)} = \frac{M_1^a \cdot E}{2} \quad K_{II}^{(1)} = \frac{M_1^b \cdot E}{2} \quad K_{III}^{(1)} = M_1^c \cdot \mu \tag{6}$$

where M_1^a , M_1^b and M_1^c are the values of the M_I -integral calculated using the three sets of asymptotic solutions.

3. Boundary Element Implementation

The computation of the M_I -integral requires the evaluation of a volume integral within closed domains that enclose a segment of the crack front L_c . A natural choice here is to make η coincident with the element nodes on the crack front, while L_c is taken as the element or element sides at which points η lies (see Figures 1 and 3). The portion of the model domain in which the volume integrals are evaluated is discretized using 27-noded isoparametric (brick) cells, over which stresses, strains and displacements derivatives are approximated by products of the cell interpolation functions Φ_i and the nodal values of σ_{ij} , ε_{ij} and $u_{i,j}$. Nodal values of these variables are computed from their boundary integral representations.

Function q is specified at all nodes within the integration volumes. Consistent with the isoparametric formulation, these q -values and its derivatives are given by

$$q = \sum_{i=1}^{27} \phi_i Q^i, \quad q_{,j} = \sum_{i=1}^{27} \sum_{k=1}^3 \frac{\partial \phi_i}{\partial \zeta_k} \frac{\partial \zeta_k}{\partial x_j} Q^i \tag{7}$$

where ζ_k are the coordinates in the cell isoparametric space, and Q^i are the nodal values of q for the i^{th} node. From the definition of q (see Refs.[2,5]), $Q^i = 0$ if the i^{th} node is on the surface of the integration volume V , while Q^i is different from null for the cell nodes lying on the arc crack front segment L_c . Different criteria for specifying Q^i are discussed in next section.

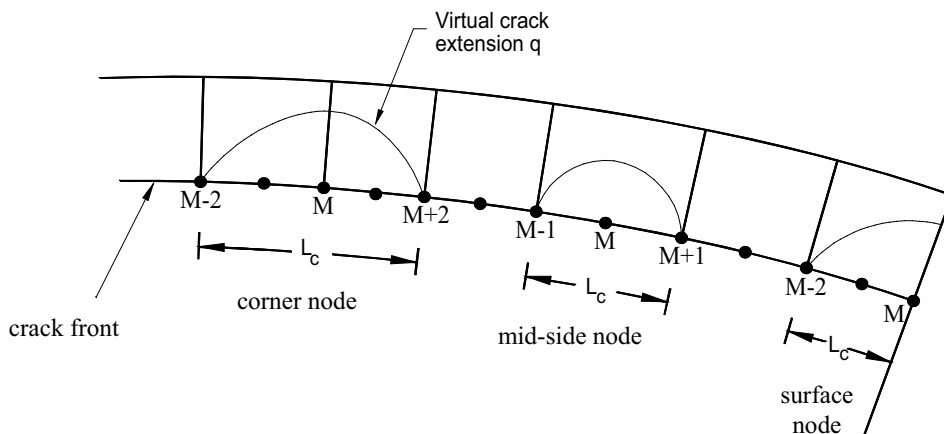


Figure 1: Schematic of the volume cells in the crack front region illustrating the virtual crack extensions for a corner node, a mid-node and a surface node.

4. The q -function

Since the virtual crack advance can adopt any arbitrary shape, the only requirement for function q is to be sufficiently smooth within the integration volume V as the evaluation of the EDI requires of its differentiation.

Shih et al[2] have shown that for the EDI the computed value of J is insensitive to the assumed shape of the q function. However, it has been found in this work that the shape of the function q is relevant for the performance of M_I -integral computations. In this sense two different approaches for the shape of function q are investigated.

Bi-quadratic q

This definition of q has been employed with excellent results in the computation of EDI in a previous work by one of the authors[5]. Within this approach q is defined to vary quadratically in the directions tangential and normal to the crack front. Considering that the evaluation point η is at the middle of the crack front segment L_c , and r_0 is the radius of the integration domain, the function q is written as:

$$q(x^*) = \left\| 1 - \left(\frac{x_3^*}{L_c/2} \right)^2 \right\| \cdot \left[1 - \left(\frac{r}{r_0} \right)^2 \right] \tag{8}$$

where r is the distance from the crack front in the plane of the crack $x_1^* - x_2^*$.

Optimised q

In a recent paper Saliva et al.[3] proposed an optimum shape for the function q which under certain considerations ensures the convergence of the EDI computations. The proposed function is

$$q(x^*) = \frac{w^p \|x^*\|^{-\beta}}{w^p \|x^*\|^{-\beta} + \sum_{i=1}^N w_j^{np} \|x^* - z_i\|^{-\beta}} \tag{9}$$

where w^p , w^{np} , and β are parameters to be chosen, and z_i are the positions of the N points with null prescribed values of q . These are given in this work by the N cell-nodes located on S_o , the outer surface of the integration volume V .

Using parameters w^p , w^{np} , and β , it is possible to control which parts of the domain significantly contribute to the integral (see Eq.(5)). In particular β is associated with the smoothness of q . Greater values induce approximately null gradients around the crack front, where non-null values of q are prescribed. In contrast, the field undergoes abrupt changes outside these regions. With w^p and w^{np} , the region with non-null

gradients can be translated near the crack front or near the boundary of the integration volume where null values of q are prescribed. Figure 2 illustrates the influence of the parameters as function of r/r_0 .

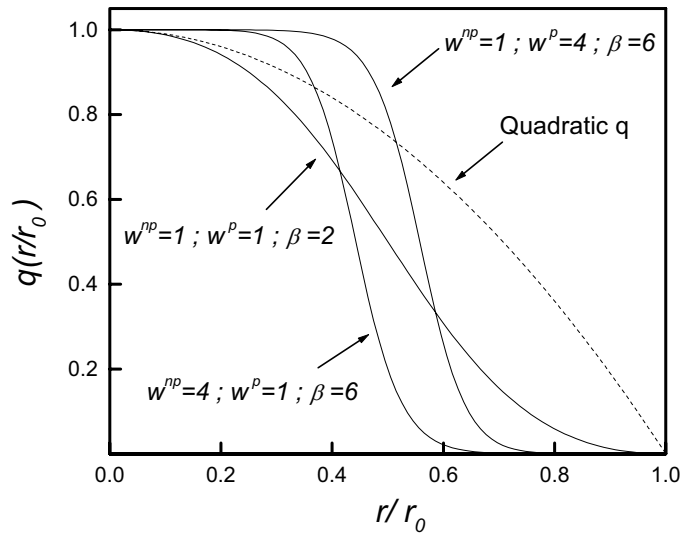


Figure 2: Influence of parameters w^p , w^{np} , and β on the shape of function q (one dimensional case).

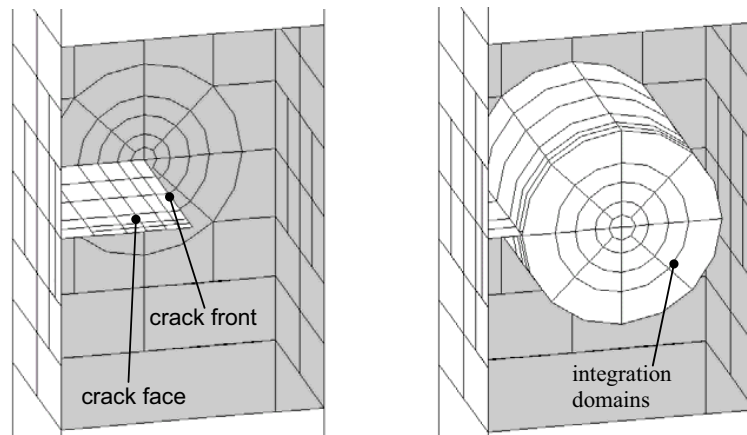


Figure 3: Boundary element discretization and integration cells.

5. Examples

5.1. The thick centre-cracked panel

The first example consists in a thick centre-cracked panel (CCP) subjected to a uniaxial remote tension σ . Model dimensions were chosen to coincide with those used by Raju and Newman[8] for the sake comparison. Material properties are Young's modulus $E=1000 \text{ N/mm}^2$ and Poisson ratio $\nu=0.33$. Model discretization consists of 193 elements and 1040 nodes. Six elements are placed along the crack front, and a total of 35 elements are used in the crack discretization (see Figure 3). Crack front element dimensions are graded towards the free surface, being the smallest equal to $t/32$. Four rings of cells with radii r/a equal to 0.2, 0.35, 0.5 and 0.75 are accommodated around the crack front for K computations. With this purpose 216 cells and 2262 nodes are employed.

Results using the bi-quadratic and the optimised q are plotted in Figure 4, together with the reference values from Ref.[8]. Following Saliva et al.[3] parameter values for the optimised q are chosen as $w^p=6$,

$w^{pp}=1$, and $\beta=6$. Error bars indicate the 5% accuracy of the reference values. Excellent agreement is found between the reported and computed results using both approaches for q , except for the point coincident with the free surface, $z/t=0.5$, where the optimised q performs markedly better. K_I -values computed at the free surface present a strong dependence with the integration volume. If in any way an average value is computed using these results, the resulting value presents almost 40% error with respect to the reference. On the other hand, the K_I -value obtained using the optimised q is almost independent of the integration volume, and it has only a 3% deviation with respect to the reference.

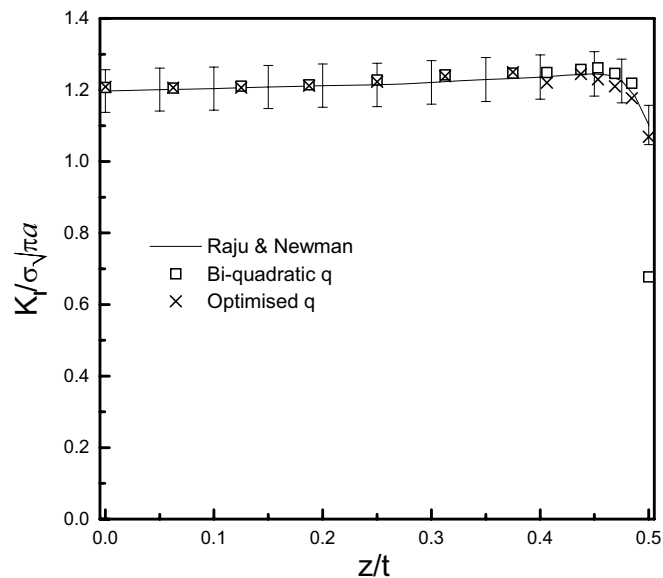


Figure 4: Variation of $K_I / \sigma \sqrt{\pi a}$ along the crack front for the CCP specimen.

5.2. Thick panel with a centre slant crack.

The second example includes a crack under mixed load conditions. It consists in a thick panel with a centre slant crack rotated $\theta=30^\circ$ with respect to the horizontal, and subjected to a uniaxial remote tension σ . The discretization strategy and material properties are the same than for the CCP. For this example 2193 nodes and 407 elements are employed for the domain discretization, while 3198 nodes and 312 cells are used to define the integration domains. Six rings of cells are placed around the crack front for the K computations.

Computed results for K_I and K_{II} are plotted in Fig. 5. The error bars in Fig. 5 indicate the dispersion of the computed results for the point coincident with the free surface when the bi-quadratic function q is used. Since results for comparison along the complete crack front are not available for this example, the only value included as a reference is the plain strain solution due to Kitagawa and Yuki [9] at the specimen mid-plane.

It can be observed that the results show the same behaviour as for the previous example: values obtained using both approaches for the function q are almost coincident along the complete crack front, except at the free surface where the optimised q performs markedly better. Once again K values computed using the bi-quadratic q present a strong dependence with the integration path on the free surface, while the optimised q does not. For the position coincident with the specimen mid-plane, obtained results are in both cases in excellent agreement with the reference value.

6. Conclusions

A three-dimensional BEM domain formulation of the M_I -integral methodology for the numerical computation of mixed-mode stress intensity factors has been presented in this paper. The proposed formulation has been implemented as a post-processing technique, and so it can be applied to the results from a particular model at a later stage. The implementation takes advantage of the efficiency of the boundary integral equation to directly obtain the required displacement derivatives, stress and strain fields.

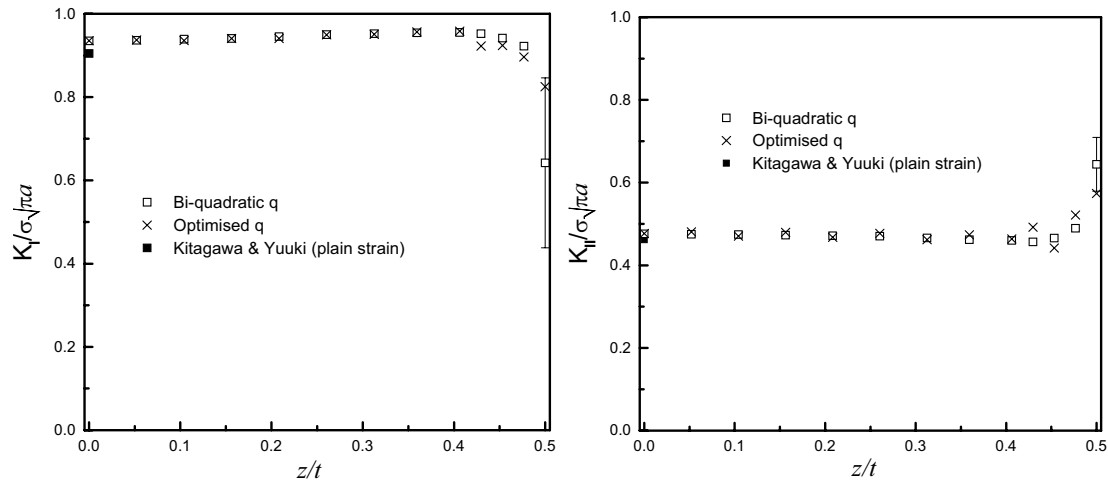


Figure 5: Variation of $K_I / \sigma \sqrt{\pi a}$ and $K_{II} / \sigma \sqrt{\pi a}$ along the crack front for the slant crack.

Special emphasis has been put in the appropriate selection of the auxiliary function q present in the domain integral formulation. In this sense two approaches have been considered: a bi-quadratic variation, and an optimised approach recently proposed in the paper by Saliva et al[3]. A number of examples demonstrate the efficiency and accuracy of the proposed formulation.

It has been found that the function q constitutes a key feature for the performance of the proposed methodology. Obtained results show that the optimised q performs markedly better for the point located at the intersection of the crack front with the free surface, allowing obtaining reliable K results where the bi-quadratic q fails. On the other hand, for crack front positions located in the interior of the specimen both approaches allow computing accurate K results, however the bi-quadratic q presents a more robust behaviour. It is observed that, in general, the bi-quadratic q performs better for the integration volumes defined closer to the crack front, and it is also not affected by the number of cells used to define the integration volume in the direction tangent to the crack front.

References

- [1] Rice J.R., A path independent integral and the approximate analysis of strain concentration by notches and cracks, *J. Appl. Mechanics*, Transactions of the ASME, 379-386, (1968)
- [2] Moran B. and Shih C.F. , A general treatment of crack tip contour integrals, *Int. J. Fracture*, 295-310, (1987)
- [3] Saliva R., Vénere M.J., Padra C., Taroco E. And Feijoo R.A., Shape sensitivity analysis and energy release rate of planar cracks embedded in three-dimensional bodies, *Computer Methods in Applied Mechanics and Engineering*, 188, 649-664, (2000)
- [4] Gosz M., Dolbow J. and Moran B., Domain integral formulation for stress intensity factor computation along curved three-dimensional interface cracks, *Int. J. of Solids & Structures*, 35/15, 1763-1783 (1998)
- [5] Cisilino A.P., *Linear and Non Linear Crack Growth using Boundary Elements*, Serie Topics in Engineering, Computational Mechanics Publications, Boston (USA) y Southampton (UK) (2000)
- [6] Chen F.H.K. and Shield R.T., Conservation laws in elasticity of the J -integral type, *J. Appl. Math. Phys.* (ZAMP) 28,1-22 (1977)
- [7] Miyazaki N., Ikeda T., Soda T. and Munakata T., Stress intensity factor analysis of interface crack using boundary element method –Application of contour-integral method, *Eng. Fract. Mech.*, 45/5,599-610, (1993)
- [8] Raju I.S. and Newman, *Three-dimensional finite element analysis of finite-thickness fracture mechanics*, Technical Report NASA TN D-8414 (1977)
- [9] Kitagawa H. and Yuuki R., Analysis of arbitrarily shaped crack in a finite plate using conformal mapping, 1st Report – Construction of analysis procedure and its applicability, *Trans. Japan Soc. Mech. Engrs.*, 43, 4354 (1977)

2-D Elastodynamic Crack Analysis in FGMs by a Time-Domain BIEM

Ch. Zhang¹, J. Sladek² and V. Sladek²

¹ Department of Civil Engineering, University of Applied Sciences Zittau/Görlitz, D-02763 Zittau, Germany

² Institute of Construction and Architecture, Slovak Academy of Sciences, 84503 Bratislava, Slovakia

Keywords: Time-domain boundary integral equation method (BIEM), Functionally graded materials (FGMs), Dynamic crack analysis, Dynamic stress intensity factors.

Abstract. A time-domain boundary integral equation method (BIEM) is presented for two-dimensional (2-D) elastodynamic crack analysis in functionally graded materials (FGMs). An exponential spatial variation is assumed for the shear modulus and the mass density. To solve the hypersingular time-domain traction boundary integral equations (BIEs), a time-stepping method based on a convolution quadrature and a spatial Galerkin-method is developed. Numerical examples are given to show the accuracy and the efficiency of the present time-domain BIEM.

1. Introduction

Functionally graded materials (FGMs) are advantageous over the conventional engineering materials and composites due to their superior thermal and mechanical properties as well as their improved wear- and corrosion resistances. FGMs are continuously non-homogeneous due to the gradual change of material properties. The initial-boundary value problem arising in transient elastodynamic crack analysis of FGMs is governed by a system of partial differential equations with variable coefficients. Since the corresponding fundamental solutions or Green's functions for general FGMs in two-dimensional (2-D) plane strain or plane stress are yet not known, the application of the boundary integral equation method (BIEM) or boundary element method (BEM) to cracked FGMs is till now very limited. In this paper, we extend the time-domain BIEM for transient elastodynamic analysis of an anti-plane crack in FGMs as presented in [1] to dynamic crack analysis of FGMs in 2-D plane strain or plane stress. A finite crack in an infinite functionally graded solid subjected to an impact crack-face loading is investigated. The material gradation is described by an exponential law for the Young's modulus and the mass density of the FGMs. To solve the corresponding initial-boundary value problem, hypersingular time-domain traction boundary integral equations (BIEs) are applied. Since no time-domain Green's functions are available for this class of FGMs, the convolution quadrature formula of Lubich [2] is used for approximating the temporal convolution integrals. For the spatial discretization of the time-domain traction BIEs, a Galerkin-method is applied. A special feature of the present time-domain BIEM is that it avoids the use of time-domain Green's functions and requires only the Laplace-domain Green's functions, which are expressed as Fourier-integrals. The spatial variation of the unknown crack-opening-displacements (CODs) is approximated by a series of Chebyshev-polynomials of second kind. An application of the convolution quadrature formula of Lubich [2] for temporal and a Galerkin-method for spatial discretizations of the BIEs yields a system of linear algebraic equations which are solved numerically time-step by time-step. Another important advantage of the method is that it requires no special regularization technique for computing the arising hypersingular integrals. Numerical examples are presented to show the accuracy of the time-domain BIEM, and the effects of the material gradation on the transient elastodynamic stress intensity factors.

2. Time-Domain Boundary Integral Equations

Let us consider an isotropic and linear elastic solid with a continuous spatial gradation in material properties as shown in Fig. 1. The Young's modulus $E(\mathbf{x})$ is assumed to be dependent on spatial coordinates while the Poisson's ratio ν is taken as constant. In this case, the generalized Hooke's law can be written as

$$\sigma_{\alpha\beta} = \mu(\mathbf{x}) E_{\alpha\beta\delta\gamma}^0 \mu_{\delta,\gamma}, \quad (1)$$

where $\sigma_{\alpha\beta}$ is the stress tensor, u_δ is the displacement vector, $\mu(\mathbf{x})$ is the shear modulus, a comma denotes partial derivatives, and

$$E_{\alpha\beta\delta\gamma}^0 = \frac{3-\kappa}{\kappa-1} \delta_{\alpha\beta} \delta_{\delta\gamma} + \delta_{\alpha\delta} \delta_{\beta\gamma} + \delta_{\alpha\gamma} \delta_{\beta\delta}. \quad (2)$$

The shear modulus $\mu(\mathbf{x})$ and the constant κ are given by

$$\mu(\mathbf{x}) = \frac{E(\mathbf{x})}{2(1+\nu)}, \quad \kappa = \begin{cases} 3-4\nu, & \text{plane strain,} \\ \frac{3-\nu}{1+\nu}, & \text{plane stress.} \end{cases} \quad (3)$$

The spatial variation of the shear modulus is approximated by an exponential law of the form

$$\mu(\mathbf{x}) = \mu_0 e^{\alpha x_1 + \beta x_2}, \quad (4)$$

where α and β are gradient parameters of the FGMs.

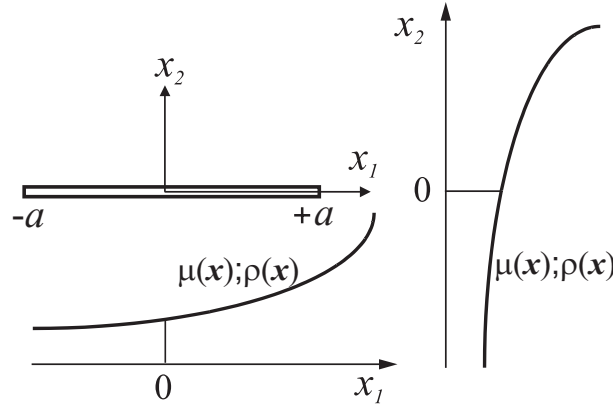


Fig. 1: A finite crack in an infinite FGM

Without body forces, the cracked FGM satisfies the equations of motion

$$\sigma_{\alpha\beta,\beta} = \rho(\mathbf{x}) \ddot{u}_\alpha, \quad (5)$$

the initial conditions

$$u_\alpha(\mathbf{x}, t) = \dot{u}_\alpha(\mathbf{x}, t) = 0, \quad t = 0, \quad (6)$$

and the stress boundary conditions on the crack-faces

$$\sigma_{\alpha 2}(\mathbf{x}, t) = \sigma_{\alpha 2}^*(\mathbf{x}) H(t), \quad |x_1| \leq a. \quad (7)$$

Here, $\sigma_{\alpha\beta}$ and u_α denote the stress and the displacement components, $\rho(\mathbf{x})$ is the mass density, a is the half crack-length, $\sigma_{\alpha 2}^*(\mathbf{x})$ is the amplitude of the stress loading, and $H(t)$ is the Heaviside step function, respectively. Throughout the analysis, a comma after a quantity stands for partial derivatives with respect to spatial variables, superscript dots represent temporal derivatives with respect to time, the conventional summation rule over double indices is implied, and Greek indices take the values 1 and 2.

To make the analysis tractable, we assume that the mass density has the same spatial variation as the shear modulus, i.e.,

$$\rho(\mathbf{x}) = \rho_0 e^{\alpha x_1 + \beta x_2}. \quad (8)$$

The displacement components $u_\gamma(\mathbf{x}, t)$ can be represented by the following boundary integral

$$u_\gamma(\mathbf{x}, t) = \int_{-a}^{+a} \sigma_{\alpha 2\gamma}^G(\mathbf{x}, \mathbf{y}; t) * \Delta u_\alpha(y_1, t) dy_1, \quad (9)$$

where $\sigma_{\alpha\beta\gamma}^G(\mathbf{x}, \mathbf{y}; t)$ are the time-domain stress Green's functions, $\Delta u_\alpha(x_1, t)$ are the crack-opening-displacements (CODs) defined by

$$\Delta u_\alpha(x_1, t) = u_\alpha(x_1, 0^+; t) - u_\alpha(x_1, 0^-; t), \quad |x_1| < a, \quad (10)$$

and an $*$ stands for Riemann convolution

$$g(\mathbf{x}, t) * h(\mathbf{x}, t) = \int_0^t g(\mathbf{x}, t - \tau) h(\mathbf{x}, \tau) d\tau. \quad (11)$$

Substitution of eq (9) into Hooke's law (1) yields a representation integral for the stress components $\sigma_{\alpha\beta}(\mathbf{x}, t)$ as

$$\sigma_{\alpha\beta}(\mathbf{x}, t) = \int_{-a}^{+a} T_{\gamma\alpha\beta}^G(\mathbf{x}, y_1; t) * \Delta u_\gamma(y_1, t) dy_1, \quad (12)$$

in which $T_{\gamma\alpha\beta}^G(\mathbf{x}, \mathbf{y}; t)$ represents the time-domain traction Green's functions. By taking the limit process $\mathbf{x} \rightarrow \Gamma_c^+ \in \{y_1 \leq |a|, y_2 = 0^+\}$ and using the boundary conditions (7), hypersingular time-domain stress or traction BIEs are obtained as

$$\int_{-a}^{+a} [T_{\gamma\alpha 2}^G(x_1, y_1; t) / \mu(x_1, 0)] * \Delta u_\gamma(y_1, t) dy_1 = \sigma_{\alpha 2}^*(x_1, 0) H(t) / \mu(x_1, 0). \quad (13)$$

It should be noted here that the required time-domain Green's functions in eqs (9) and (13) are not available for the FGMs considered here. To circumvent this difficulty, a numerical solution procedure based on a convolution quadrature of Lubich [2] is presented in the next section, which needs only the Laplace-transform of the time-domain Green's functions. The Laplace transformed stress Green's functions $\bar{\sigma}_{\alpha 2 \gamma}^G(\mathbf{x}, \mathbf{y}; p)$ for the considered FGMs can be expressed as the following Fourier-integral

$$\bar{\sigma}_{\alpha 2 \gamma}^G(\mathbf{x}, \mathbf{y}; p) = \frac{1}{2\pi} \int_{-\infty}^{\infty} \sum_{j=1}^2 S_{\alpha\gamma; j}^\pm e^{i\xi(x_1 - y_1) \mp \gamma_j^\pm(x_2 - y_2)} d\xi, \quad (14)$$

where

$$\begin{aligned} S_{11;1}^+ &= \frac{c_{22}}{\Delta_c}, & S_{11;2}^+ &= -\frac{c_{21}}{\Delta_c}, \\ S_{11;1}^- &= \frac{1}{\Delta_c} (A_1 c_{22} - A_2 c_{21}), & S_{11;2}^- &= \frac{1}{\Delta_c} (A_3 c_{22} - A_4 c_{21}), \\ S_{21;1}^+ &= -\frac{c_{12}}{\Delta_c}, & S_{21;2}^+ &= \frac{c_{11}}{\Delta_c}, \\ S_{21;1}^- &= \frac{1}{\Delta_c} (A_2 c_{11} - A_1 c_{12}), & S_{21;2}^- &= \frac{1}{\Delta_c} (A_4 c_{11} - A_3 c_{12}), \\ S_{\alpha 2; j}^\pm &= \lambda_j^\pm S_{\alpha 1; j}^\pm \quad (\text{no sum over } j), \end{aligned} \quad (15)$$

in which

$$\begin{aligned} A_1 &= \frac{1}{\Delta} (a_1^+ b_2^- - a_2^- b_1^+), & A_2 &= \frac{1}{\Delta} (a_2^+ b_2^- - a_2^- b_2^+), \\ A_3 &= \frac{1}{\Delta} (-a_1^+ b_1^- + a_1^- b_1^+), & A_4 &= \frac{1}{\Delta} (-a_2^+ b_1^- + a_1^- b_2^+), \end{aligned} \quad (16)$$

$$\Delta = a_1^- b_2^- - a_2^- b_1^-.$$

$$\begin{aligned} c_{11} &= 1 - A_1 - A_3, & c_{12} &= 1 - A_2 - A_4, \\ c_{21} &= \lambda_1^+ - \lambda_1^- A_1 - \lambda_2^- A_3, & c_{22} &= \lambda_2^+ - \lambda_1^- A_2 - \lambda_2^- A_4, \end{aligned} \quad (17)$$

$$\Delta_c = c_{11} c_{22} - c_{12} c_{21}.$$

$$\lambda_j^\pm = -\frac{-\frac{\kappa+1}{\kappa-1}\xi^2 + (\gamma_j^\pm)^2 + \frac{\kappa+1}{\kappa-1}i\xi\alpha \mp \beta\gamma_j^\pm - \rho_0 p^2}{\mp \frac{2}{\kappa-1}i\xi\gamma_j^\pm + i\beta\xi \mp \frac{3-\kappa}{\kappa-1}\alpha\gamma_j^\pm}, \quad (18)$$

$$a_j^\pm = i\xi\lambda_j^\pm \mp \gamma_j^\pm, \quad b_j^\pm = \frac{3-\kappa}{\kappa-1}i\xi \mp \frac{\kappa+1}{\kappa-1}\gamma_j^\pm\lambda_j^\pm, \quad (\text{no sum over } j). \quad (19)$$

In eqs (14) and (18), p is the Laplace-transform parameter, and $\gamma_{1,2}^\pm$ satisfy the following characteristic equation

$$\left(-\frac{\kappa+1}{\kappa-1}\xi^2 + (\gamma^\pm)^2 + \frac{\kappa+1}{\kappa-1}i\xi\alpha \mp \beta\gamma^\pm - \rho_0 p^2\right) \cdot \left(-\xi^2 + \frac{\kappa+1}{\kappa-1}(\gamma^\pm)^2 + i\xi\alpha \mp \frac{\kappa+1}{\kappa-1}\beta\gamma^\pm - \rho_0 p^2\right) \\ - \left(\mp \frac{2}{\kappa-1}i\xi\gamma^\pm + i\beta\xi \mp \frac{3-\kappa}{\kappa-1}\alpha\gamma^\pm\right) \cdot \left(\mp \frac{2}{\kappa-1}i\xi\gamma^\pm + \frac{3-\kappa}{\kappa-1}i\beta\xi \mp \alpha\gamma^\pm\right) = 0. \quad (20)$$

The regularity condition of the solution at infinity requires that $\text{Re}(\gamma_{1,2}^\pm) \geq 0$.

Similarly, the Laplace transformed traction Green's functions can be expressed as

$$\bar{T}_{\gamma\alpha\beta}^G(\mathbf{x}, \mathbf{y}) = \frac{1}{2\pi} \int_{-\infty}^{\infty} \sum_{j=1}^2 \hat{T}_{\gamma\alpha\beta;j}^\pm e^{i\xi(x_1-y_1) \mp \gamma_j^\pm(x_2-y_2)} d\xi, \quad (21)$$

where $\hat{T}_{\gamma\alpha\beta;j}^\pm = \hat{T}_{\gamma\beta\alpha;j}^\pm$, and

$$\begin{Bmatrix} \hat{T}_{\alpha 11;j}^\pm \\ \hat{T}_{\alpha 22;j}^\pm \\ \hat{T}_{\alpha 12;j}^\pm \end{Bmatrix} = \mu(\mathbf{x}) S_{\alpha 1;j}^\pm \begin{bmatrix} \frac{\kappa+1}{\kappa-1} & \frac{3-\kappa}{\kappa-1} & 0 \\ \frac{3-\kappa}{\kappa-1} & \frac{\kappa+1}{\kappa-1} & 0 \\ 0 & 0 & 1 \end{bmatrix} \begin{Bmatrix} i\xi \\ (\mp \gamma_j^\pm)\lambda_j^\pm \\ a_j^\pm \end{Bmatrix}. \quad (22)$$

3. Numerical Solution Procedure

To solve the hypersingular time-domain traction BIEs (13), the convolution quadrature of Lubich [2] in conjunction with a Galerkin-method is applied in this paper. The unknown CODs $\Delta u_\gamma(y_1, \tau)$ are expanded into a series of the form

$$\Delta u_\gamma(y_1, \tau) = \sqrt{a^2 - y_1^2} \sum_{k=1}^K c_{\gamma;k}(\tau) U_{k-1}\left(\frac{y_1}{a}\right), \quad (23)$$

where K is the total number of used terms, $c_{\gamma;k}(\tau)$ are unknown time-dependent expansion coefficients and $U_{k-1}(y_1/a)$ are Chebyshev polynomials of second kind. Substituting eq (23) into eq (13), multiplying both sides by $\sqrt{a^2 - x_1^2} U_{l-1}(x_1/a)$, integrating them with respect to x_1 from $-a$ to $+a$, and applying the convolution quadrature formula of Lubich [2]

$$f(t) = g(t) * h(t) = \int_0^t g(t-\tau)h(\tau)d\tau \implies f(n\Delta t) = \sum_{j=0}^n \omega_{n-j}(\Delta t)h(j\Delta t), \quad (24)$$

a system of linear algebraic equations for the expansion coefficients is obtained as

$$\sum_{k=1}^n \sum_{l=1}^K A_{\gamma\alpha;kl}^{n-j} c_{\gamma;k}^j = f_{\alpha;l}^n, \quad (n = 1, 2, \dots, N; \quad l = 1, 2, \dots, K), \quad (25)$$

where the time-variable t is divided into N equal time-steps Δt , and the superscript indices stand for the time-steps. The system matrix in eq (25) corresponds to the integration weights $\omega_{n-j}(\Delta t)$ of the convolution quadrature formula (24). The system matrix $A_{\gamma\alpha;kl}^{n-j}$ and the right-hand side $f_{\alpha;l}^n$ of eq (25) are given by

$$A_{\gamma\alpha;kl}^{n-j} = \frac{r^{-(n-j)} M^{-1}}{M} \sum_{m=0}^{M-1} A_{\gamma\alpha;kl}(p_m) e^{-2\pi i(n-j)m/M}, \quad (26)$$

$$f_{\alpha;l}^n = (-1)^{l+1} \int_{-a}^{+a} [\sigma_{\alpha 2}(x_1, 0; n\Delta t) / \mu(x_1, 0)] \sqrt{a^2 - x_1^2} U_{l-1} \left(\frac{x_1}{a} \right) dx_1, \tag{27}$$

where

$$p_m = \frac{\delta(\zeta_m)}{\Delta t}, \quad \delta(\zeta_m) = \sum_{j=1}^2 \frac{(1 - \zeta_m)^j}{j}, \quad \zeta_m = re^{2\pi i m/M}. \tag{28}$$

In this analysis, $M=N$ and $r^N = \sqrt{\varepsilon}$ are chosen with ε being the numerical error in the computation of the Laplace-domain system matrix $\bar{A}_{\gamma\alpha;kl}(p_m)$. The Laplace-domain system matrix $\bar{A}_{\gamma\alpha;kl}(p_m)$ can be obtained by using

$$\bar{A}_{\gamma\alpha;kl}(p_m) = (-1)^l \int_{-a}^{+a} \sqrt{a^2 - x_1^2} U_{l-1} \left(\frac{x_1}{a} \right) \int_{-a}^{+a} [\bar{T}_{\gamma\alpha 2}^G(x_1, y_1; p_m) / \mu(x_1, 0)] \times \sqrt{a^2 - y_1^2} U_{k-1} \left(\frac{y_1}{a} \right) dy_1 dx_1. \tag{29}$$

Substituting eq (21) into eqs (27) and (29) and using the following relations ([3], [4])

$$\int_{-1}^1 \sqrt{1 - \eta^2} U_{k-1}(\eta) e^{i\alpha\eta} d\eta = \frac{\pi k}{\alpha} i^{k-1} J_k(\alpha), \tag{30}$$

$$J_k(-\xi) = (-1)^k J_k(\xi), \quad J_k(i\xi) = i^k I_k(\xi), \tag{31}$$

the Laplace-domain system matrix $\bar{A}_{\gamma\alpha;kl}(p_m)$ and the right-hand side can be rewritten as

$$\bar{A}_{\gamma\alpha;kl}(p_m) = (\pi a)^2 (kl) i^{3(k+l)} \int_0^\infty G_{\gamma\alpha}(\xi, p_m) \frac{1}{\xi^2} J_k(\xi a) J_l(\xi a) d\xi, \tag{32}$$

$$f_{\alpha;l}^n = -\sigma_{\alpha 2}^* (\pi a) l \frac{1}{\alpha} I_l(\alpha a), \tag{33}$$

where $J_k(\cdot)$ is the Bessel function of first kind and k -th order, $I_l(\cdot)$ is the modified Bessel function of first kind and l -th order, and

$$G_{\gamma\alpha}(\xi, p_m) = F_{\gamma\alpha}(\xi, p_m) + (-1)^{k+l} F_{\gamma\alpha}(-\xi, p_m), \tag{34}$$

$$F_{\gamma\alpha}(\xi, p_m) = \frac{1}{2\pi\Delta c} \begin{bmatrix} a_1^+ c_{22} - a_2^+ c_{21} & -a_1^+ c_{12} + a_2^+ c_{11} \\ b_1^+ c_{22} - b_2^+ c_{21} & -b_1^+ c_{12} + b_2^+ c_{11} \end{bmatrix}. \tag{35}$$

Note here that a uniform stress crack-face loading is assumed in deriving eq (33).

For $\xi \rightarrow \infty$, the integrand in eq (32) behaves as $1/\xi^2$. The slow convergency rate $1/\xi^2$ of the integrand in eq (32) is inconvenient for numerically computing the system matrix. To get a better convergency, eq (32) is recast into

$$\bar{A}_{\gamma\alpha;kl}(p_m) = (\pi a)^2 (kl) i^{3(k+l)} \left\{ \int_0^\infty \left[\frac{G_{\gamma\alpha}(\xi, p_m)}{\xi^2} - \frac{G_{\gamma\alpha}^\infty}{\xi} \right] J_k(\xi a) J_l(\xi a) d\xi + G_{\gamma\alpha}^\infty \frac{\delta_{kl}}{k+l} \right\}, \tag{36}$$

where use is made of the following integral relation of the Bessel function [4]

$$\int_0^\infty \frac{1}{\xi} J_k(\xi) J_l(\xi) d\xi = \frac{\delta_{kl}}{k+l}, \tag{37}$$

and the constants $G_{\gamma\alpha}^\infty$ in eq (36) are given by

$$G_{\gamma\alpha}^\infty = -\frac{2}{\kappa+1} \left[1 + (-1)^{k+l} \right] \delta_{\gamma\alpha}. \tag{38}$$

The Laplace-domain system matrix $\bar{A}_{\gamma\alpha;kl}(p_m)$ is symmetric and complex-valued, while the time-domain system matrix $A_{\gamma\alpha;kl}^n$ is also symmetric but real-valued. Note here that the present method requires only a numerical integration of a single integral, which makes the numerical scheme especially efficient and attractive. The infinite integral of (36) can be computed numerically by using an adaptive Romberg quadrature method in conjunction with the truncation method. Unlike the conventional time-domain BEM, the present time-domain BIEM applies Laplace-domain instead of time-domain Green's functions. Hence, no explicit expressions of the time-domain Green's functions are needed here. The evaluation of eq (26) can be performed very efficiently by using the Fast Fourier Transform (FFT). The expansion coefficients $c_{\gamma,k}^n$ can be computed numerically from eq (25) time-step by time-step.

4. Numerical Examples

The dynamic stress intensity factors are related to the CODs by

$$\begin{Bmatrix} K_I^\pm(t) \\ K_{II}^\pm(t) \end{Bmatrix} = \frac{\sqrt{2\pi}}{\kappa+1} \mu(\pm a, 0) \lim_{x_1 \rightarrow \pm a} \frac{1}{\sqrt{a \mp x_1}} \begin{Bmatrix} \Delta u_2(x_1, t) \\ \Delta u_1(x_1, t) \end{Bmatrix}, \quad (39)$$

where “ \pm ” indicates the crack-tips at $x_1 = +a$ and $x_1 = -a$. Substituting eq (23) into eq (39) and using the identity [3]

$$U_{k-1}(\pm 1) = (\pm 1)^{k-1} k \quad (40)$$

a relation between the dynamic stress intensity factors and the expansion coefficients $c_{\gamma,k}(t)$ is obtained as

$$\begin{Bmatrix} K_I^\pm(t) \\ K_{II}^\pm(t) \end{Bmatrix} = \frac{2}{\kappa+1} \sqrt{\pi a} \mu(\pm a, 0) \begin{Bmatrix} \sum_{k=1}^K (\pm 1)^{k-1} k c_{2;k}(t) \\ \sum_{k=1}^K (\pm 1)^{k-1} k c_{1;k}(t) \end{Bmatrix}. \quad (41)$$

To check the accuracy of the present time-domain BIEM, let us consider an infinite unidirectional FGM with a crack parallel to the material gradient as depicted in Fig. 2. The crack is subjected to an impact tensile crack-face loading of the amplitude σ . Numerical calculations have been carried out for plane strain and a Poisson's ratio $\nu=0.3$. The error parameter used in the computation of the time-domain system matrix $A_{\gamma\alpha;kl}^n$ defined by eq (26) is selected as $\varepsilon=10^{-12}$.

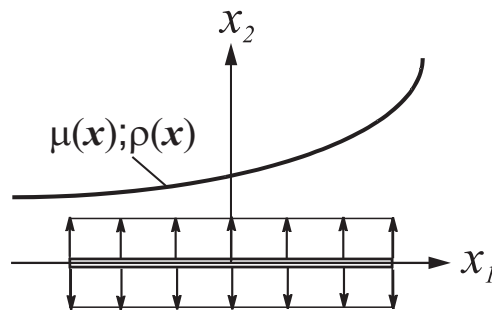


Fig. 2: A crack parallel to the material gradient

For three different values of K , i.e., terms used in the Galerkin-ansatz (23), the normalized mode-I dynamic stress intensity factors

$$\bar{K}_I^\pm(t) = K_I^\pm(t) / (\sigma \sqrt{\pi a}) \quad (42)$$

are presented in Fig. 3 versus the dimensionless time $c_T t/a$, where $c_T = \sqrt{\mu_0/\rho_0}$. Here, the time-step is selected as $c_T \Delta t/a = 0.1$, and the dimensionless gradient parameter is chosen as $\alpha a = 0.5$. Figure 3 shows that $K=10$, i.e.,

10 terms in the Galerkin-ansatz (23), are sufficient to obtain accurate results for the normalized dynamic stress intensity factors. It should be noted here that the mode-II dynamic stress intensity factors $K_{II}^{\pm}(t)$ are identically zero for this specific crack configuration.

The influence of the time-step on the normalized mode-I dynamic stress intensity factors is shown in Fig. 4, where $K=10$ and $\alpha a=0.5$ have been chosen. It can be seen from Fig. 4 that the present time-domain BIEM is quite insensitive to the used time-steps.

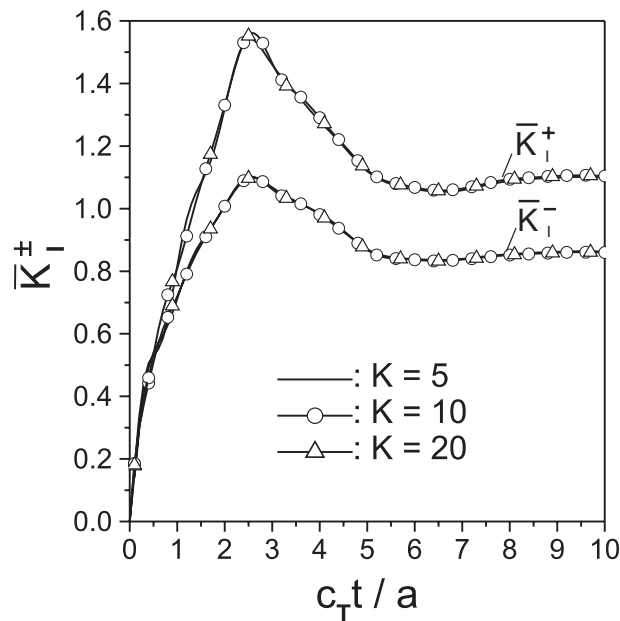


Fig. 3: Effects of used terms

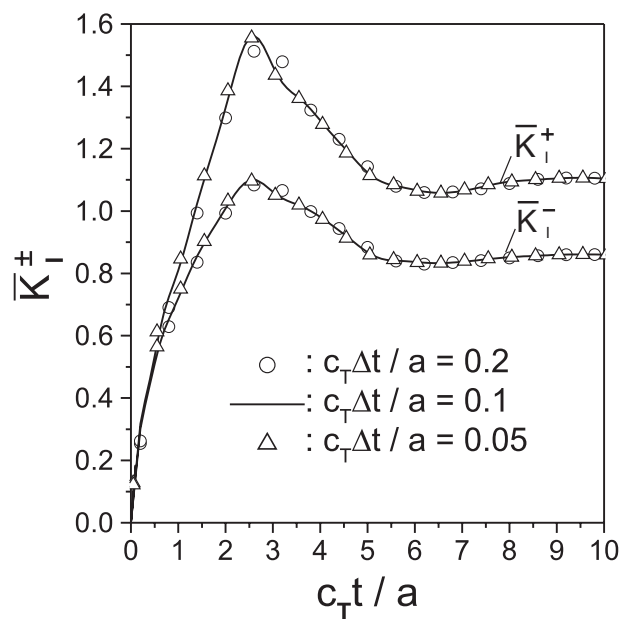


Fig. 4: Effects of used time-steps

For a crack in a homogeneous material (i.e., $\alpha a = \beta a = 0$) subjected to an impact tensile crack-face loading, a comparison of the present numerical results for the dynamic stress intensity factors with the analytical results

of Thau and Lu [5] and the numerical ones of [6] via a time-domain BEM is made in Fig. 5. A good agreement is obtained here. This confirms the accuracy of the present time-domain BIEM. In this numerical example, the Poisson's ratio is taken as $\nu=0.25$.

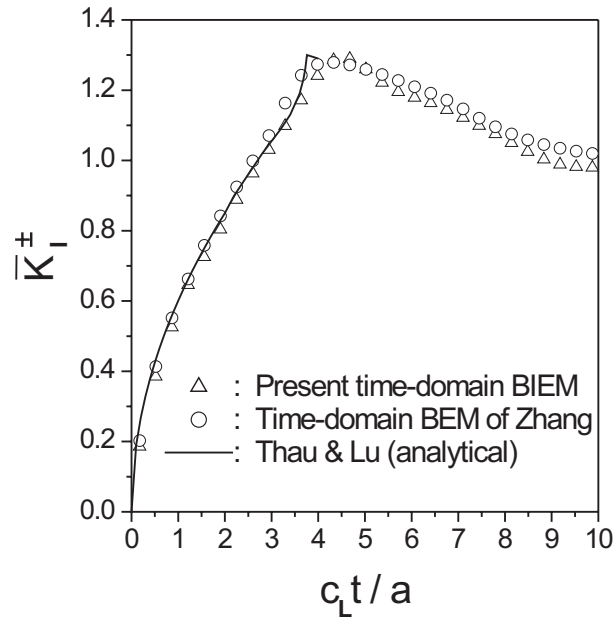


Fig. 5: A comparison of numerical and analytical results

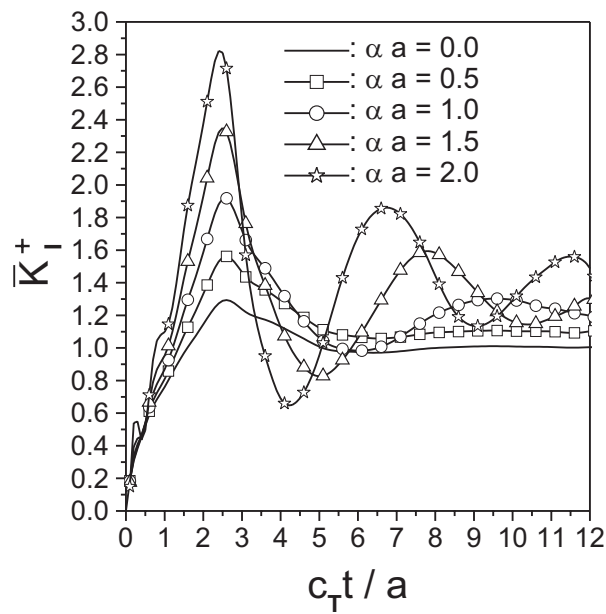


Fig. 6: $\bar{K}_I^+(t)$ versus dimensionless time

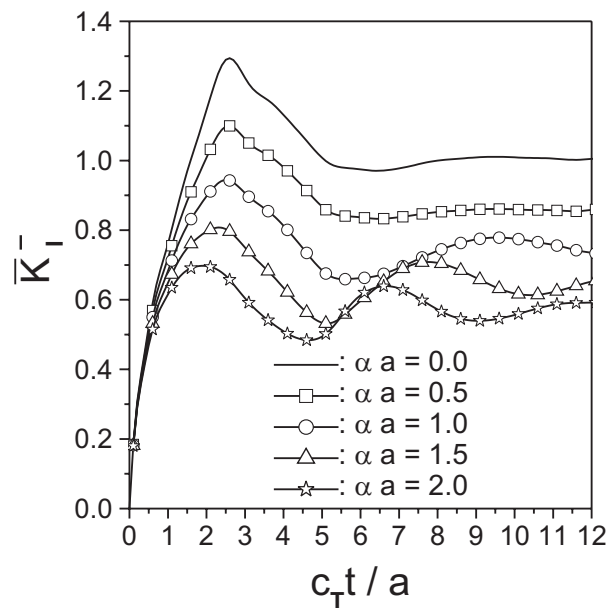


Fig. 7: $\bar{K}_I^-(t)$ versus dimensionless time

For five values of the gradient parameter αa , the normalized mode-I dynamic stress intensity factors are given in Figs. 6-7. Numerical results are obtained by using $K=10$ and $c_T \Delta t/a=0.1$. Figures 6-7 show that the maximum normalized dynamic stress intensity factors at the crack-tip $x_1=+a$ increase, while those at the crack-tip $x_1=-a$ decrease with increasing gradient parameter αa . The maximum normalized mode-I dynamic stress intensity factors at the crack-tip $x_1=+a$ are larger than that at the crack-tip $x_1=-a$, i.e., $\max \bar{K}_I^+ > \max \bar{K}_I^-$. Compared to the homogeneous case, i.e., $\alpha a=0$, the maximum mode-I dynamic stress intensity factor at the crack-tip $x_1=+a$ is amplified, while that at the crack-tip $x_1=-a$ is reduced. In all cases considered here, the normalized dynamic stress intensity factors first increase with increasing dimensionless time, after reaching their peak values they then decrease, and thereafter they oscillate about their corresponding static values in the large-time limit.

5. Summary

A time-domain BIEM is presented in this paper for transient elastodynamic crack analysis in isotropic, linear elastic and continuously nonhomogeneous FGMs subjected to an impact crack-face loading. A hypersingular time-domain traction BIE formulation is used for this purpose. The temporal convolution of the time-domain BIEs is approximated by the convolution quadrature formula of Lubich [2], which requires only the Laplace-domain instead of the unknown time-domain Green's functions. Fourier-integral representations are applied for the Laplace-domain Green's functions. A Galerkin-method is adopted for the spatial discretization of the time-domain BIEs, which avoids any regularization or special integration techniques to deal with the hypersingular integrals. The accuracy and the efficiency of the present time-domain BIEM are verified by numerical results of the elastodynamic stress intensity factors for a crack parallel to the material gradient subjected to an impact tensile crack-face loading.

Acknowledgement: This work is supported by the Project for Bilateral Cooperation in Science and Technology granted jointly by the International Bureau of the German BMBF and the Ministry of Education of Slovak Republic under the project number SVK 01/020.

References

- [1] Ch. Zhang, J. Sladek and V. Sladek *Int. J. Solids Struct.*, **40**, 5251-5270 (2003).
- [2] C. Lubich *Numerische Mathematik*, **52**, 129-145 (1988).
- [3] M. Abramowitz and I.A. Stegun *Handbook of Mathematical Functions*, Dover Publications, New York (1972).
- [4] I.S. Gradshteyn and I.M. Ryzhik *Table of Integrals, Series, and Products*, Academic Press, Inc., London (1980).
- [5] S.A. Thau and T.H. Lu *Int. J. Solids Struct.*, **7**, 731-750 (1971).
- [6] Ch. Zhang *Wave Motion*, **35**, 17-40 (2002).

Application of the BEM for determining singular stress fields for the conditions of failing mode-II cracks

A. Blázquez¹, J.F. Kalthoff², I. Palomino³ and A. Fernández-Canteli⁴

¹ Dept. of Mechanical Engineering, University of La Rioja. C/ Luis de Ulloa, 20. 26004 Logroño (Spain). email: antonio.blazquez@dim.unirioja.es

² Dept. of Experimental Mechanics. Ruhr-University Bochum. Universitätsstr. 150 44780 Bochum (Germany). email: Joerg.F.Kalthoff@ruhr-uni-bochum.de

³ School of Engineering. University of Sevilla. Camino de los Descubrimientos s/n. 41092 Sevilla (Spain).

⁴ Dept. of Const. and Manufacturing Engng. University of Oviedo. Campus de Viesques, 33203 Gijón (Spain). email: afc@uniovi.es

Keywords: Linear-elastic fracture mechanics, Arcan-Richard specimen, mode-II, kinked cracks, stress intensity factors, energy release rates, virtual crack closure integral, multibody approach.

Abstract. The instability condition for the initiation of a kinked crack starting from a crack subjected to mode-II loading conditions is investigated. Special emphasis is given to the changes the stress fields experience in the transition phase from before to after the kinked crack is initiated. In addition, the situation is considered for growing crack lengths, from very small values approaching zero till medium sized crack lengths. The stress field that builds up at the corner notch after the kinked crack initiated is also studied for comparison. The BEM with its inherent high spatial resolution is used as the adequate technique for this kind of investigations.

Introduction

A crack subjected to shear (mode-II) conditions of loading (denoted mother crack) in brittle materials fails by initiating a tensile (mode-I) kinked crack (denoted daughter crack) propagating at an angle of about -70° with respect to the direction of the original mother crack. Between the mother crack and the daughter crack a notch is formed.

This paper is aimed to investigate the transition of the mode-II crack tip stress singularity of the mother crack before instability to the two singularities after instability, i.e. the mode-I singularity at the daughter crack and the additional stress singularity at the notch that is formed. The investigations consider lengths of the daughter crack from very small to considerably larger values.

Due to the very high spatial resolution needed for solving this problem, the BEM was chosen, primarily because of the small lengths considered for the daughter crack, but also because of the precision required for determining the stress fields in the immediate vicinity of the crack tip. The feasibility of the BEM-model for such fracture mechanics applications is checked by comparing stress intensity factors calculated directly by extrapolation techniques with strain energy release rates determined using the virtual crack closure integral.

Numerical calculations

The boundary element calculations are performed for an Arcan-Richard-type specimen of width $W = 50$ mm prepared with a pre-existing crack of length of half the width. The specimen size is chosen to be in accordance with practical test data that apply for measuring the fracture toughness of the aluminium alloy Al 7075 ($E = 71000$ MPa, $\nu = 0.34$, $R_{p0.2} = 533$ MPa, $K_{Ic} = 30$ MPa m^{1/2}, $K_{IIc} = 44.4$ MPa m^{1/2}).

For the solution of the elastic problem, a plane model under plane strain conditions was considered using a multibody approach. Six bodies were considered initially as shown in Fig. 1: Two solids represent the field of interest of the specimen where the cracks are located. Two other solids constitute the fixing zones (dark grey); for these reinforced zones a Young modulus 10 times higher than that of the base material was used.

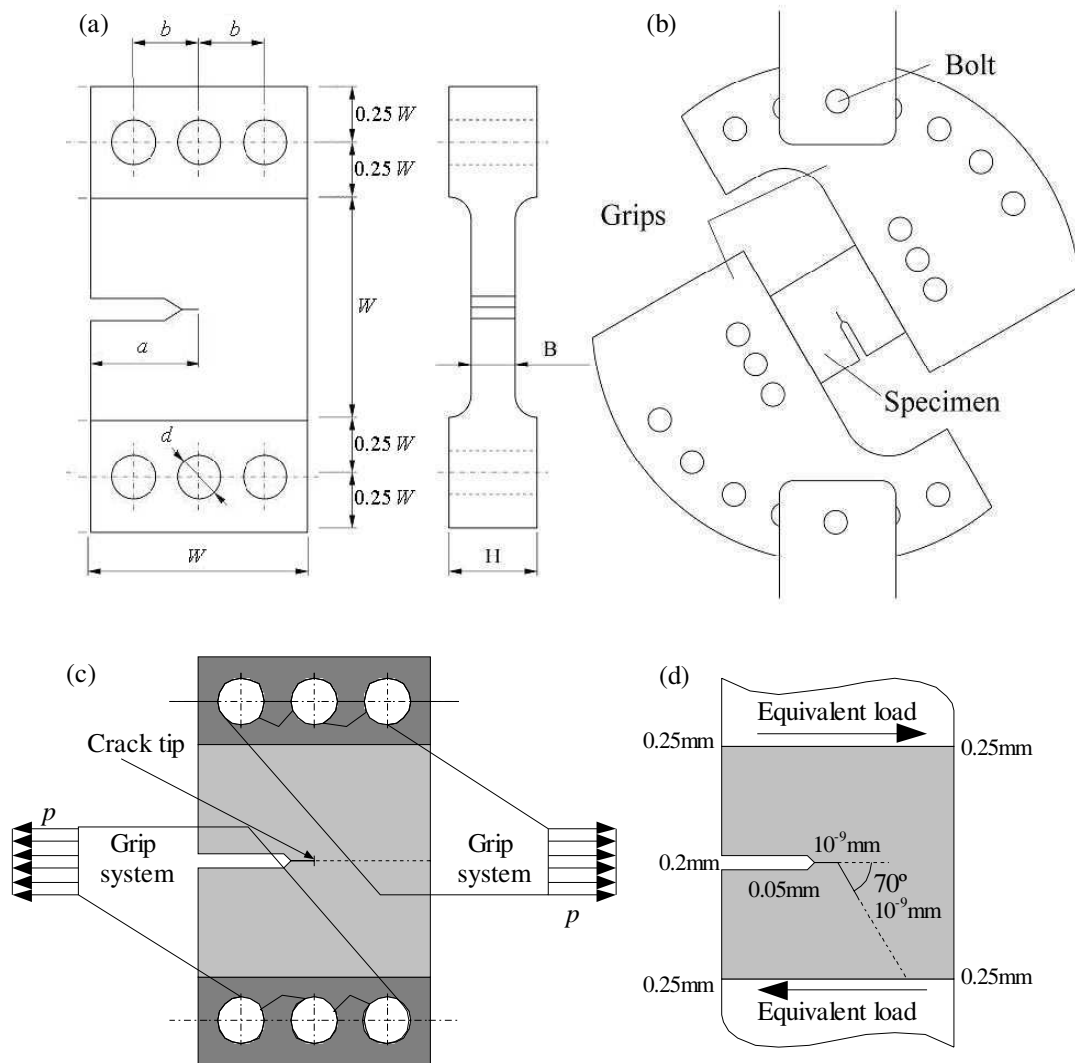


Fig. 1: Arcan-Richard set-up: a) specimen, b) grips, c) complete model used in the numerical calculation, d) simplified model and mesh size.

For the last two solids representing the grips a stiffness 1000 times higher than that of the base material was assumed [1].

All the calculations were performed with the aid of a boundary element code, based on linear elements [2], assuming weak solutions for the boundary and interface conditions [3] with limitations of the rigid solid motion according to the formulation proposed by [4]. Figure 1b shows the approximate size of the elements in the significant regions of the boundary element model. The sizes have been maintained for all the calculations carried out.

Solving the foregoing problem allows one to establish the interactions among the different solids, particularly among the solids defining the thickened parts of the specimens and the ones concerning the field of study. Assuming these interactions not being changed during the process, the stress field in the vicinity of the crack can be analyzed for different crack lengths, see Fig. 1b. The interface among the solids was defined as having an inclination of -70° , with respect to the crack plane of the original mode-II mother crack.

Numerical results in the internal points of the domain

The results are presented with respect to three coordinate systems with origins at the tip of the corresponding stress singularities (see Fig. 2). The indices M , D , and N are used for characterizing the mother crack, the daughter crack, and the notch, respectively. The stress field results are shown in Figs. 3 and 4. The stress field singularities at the tip of the mother crack and the daughter cracks are found to show a $r^{-0.5}$ dependence (as expected in fracture mechanics), the singularity coefficient of the notch results to -0.41 in accordance with the results in [5], for a notch of an opening angle of 250° . In Figs. 3 and 4 the stresses multiplied by the singularity dependence are plotted, in all cases normalized by the stress intensity factor of the mother crack K_{IIIM} . For two different lengths of the daughter crack, the stresses around the singularity are given at different radial distances r . The corresponding analytical results of the near tip stress fields for mode-II or for mode-I loading are also given (continuous line) for comparison.

Figure 3 shows the numerical results for the original mother crack before the daughter crack arises ($a_D = 0$, reference angle θ_M). Along very close circles to the crack tip ($r = 0.0005$ or 0.05 mm) the numerical results practically coincide with the analytical ones for a typical mode-II stress field [6]. For increasing distances ($r = 5$ mm) discrepancies result because of the influence of far field effects.

Figures 4a and 4b show the normalized stress distributions around the tip of the daughter crack for two different lengths of the daughter crack ($a_D = 0.01$ and 1 mm). Radial distances r of the same ratio r/a_D are used. For both cases of crack lengths, the stress field for very small values r (compared to the crack length) approaches notably a typical mode-I stress field. For distances far away from the crack tip (compared to the crack length), a mode-II stress field, i.e. the stress field of the mother crack, results. Please note, the angle θ_D is shifted in relation to θ_M (used in Fig. 3) due to the different reference axes. Practically the same results were found for the intermediate crack length, $a_D = 0.1$ mm, not given here due to space limitations. The conclusions are practically independent from crack length.

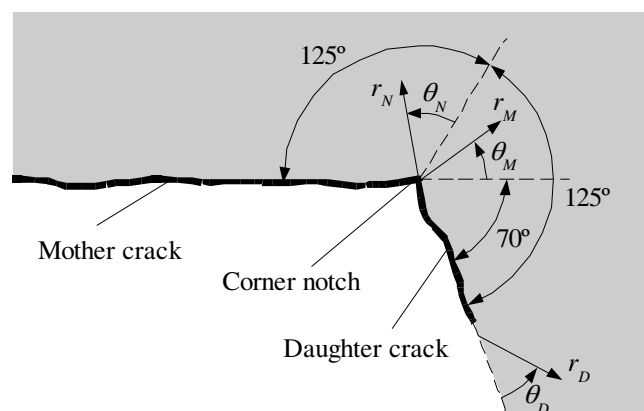


Fig. 2: Coordinate systems considered in the present study for the original mother crack, for the kinked daughter crack and for the corner notch, built between the two.

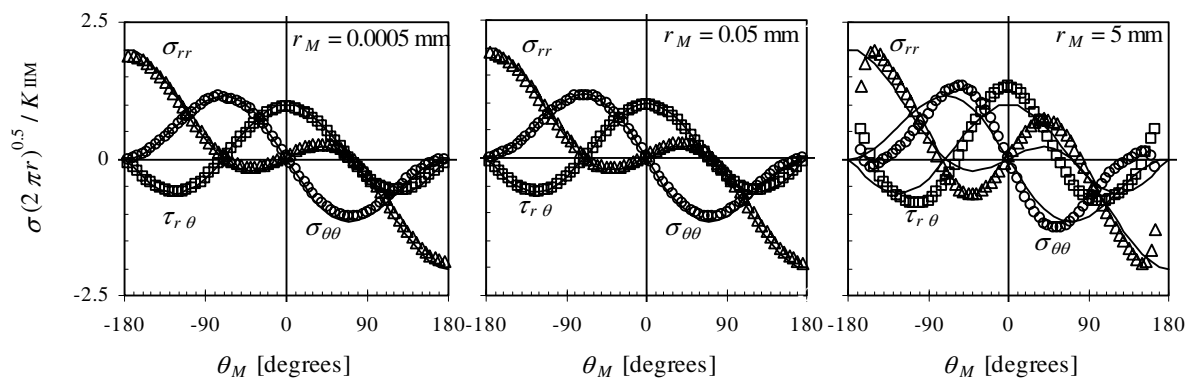


Fig. 3: Normalized stresses for different distances, r , as functions of the angular orientation, θ_M , around the tip of the mother crack.

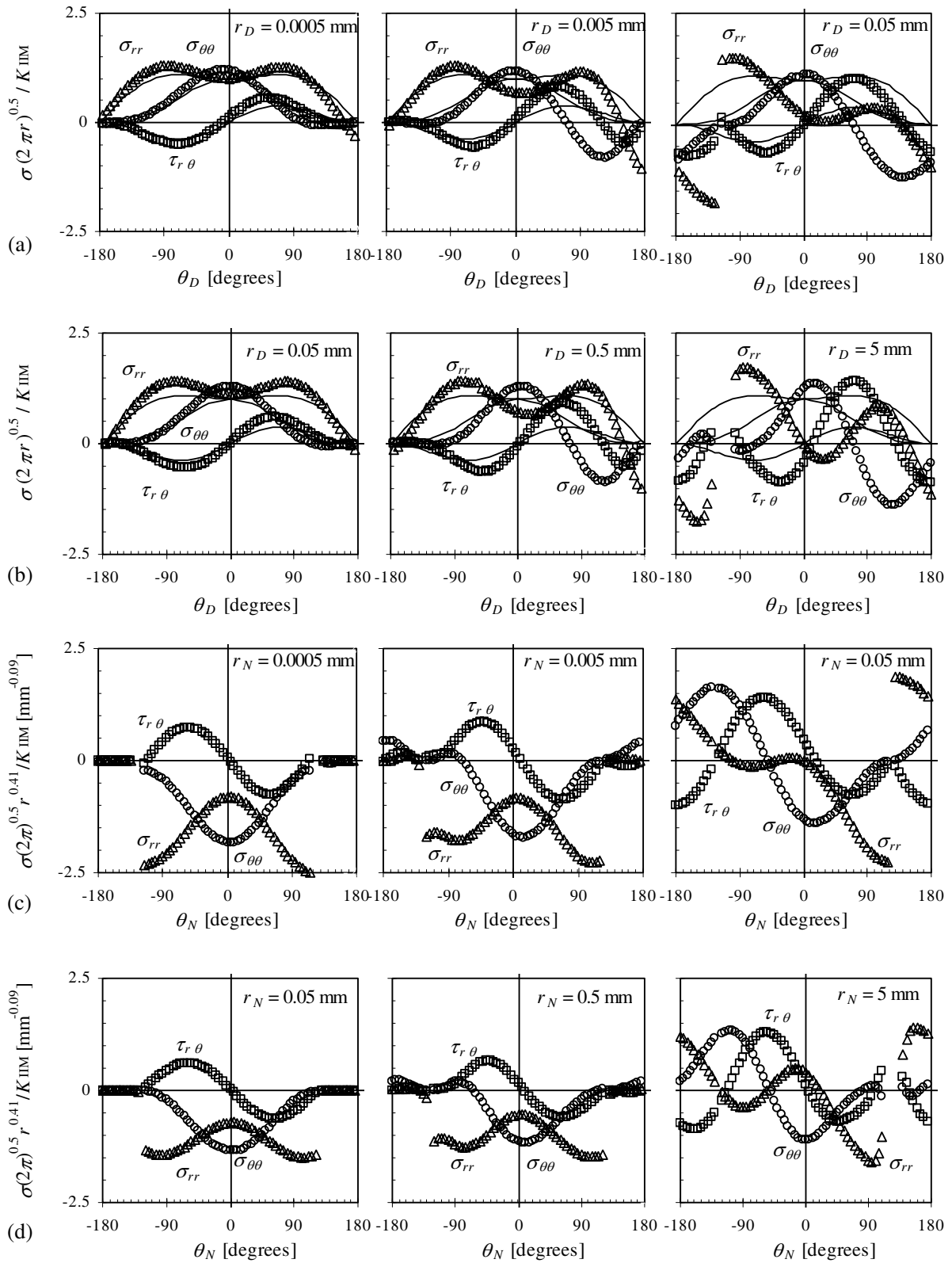


Fig. 4: Normalized stresses for different distances, r , as functions of the angular orientation around the tip of the daughter crack for length a) $a_D = 0.01$ mm, b) $a_D = 1$ mm and around the corner notch for length c) $a_D = 0.01$ mm, d) $a_D = 1$ mm.

Figures 4c and 4d give the singular stress fields that were found around the corner notch for the two lengths of the daughter crack. These stress fields for small radial distances agree well with the results for the stress distribution around a notch (250° opening angle) derived analytically in [5]. Please, recognize the compressive character of the field, which was also found in experimental investigations in [7]. At large distances (compared to the length of the daughter crack), when the corner notch is circumscribed, the mode-II stress field around the mother crack results (see Fig. 3 for comparison, again note the shift due to the differently defined angles used).

It can be concluded from the results reported that the presence of the daughter crack, but not its absolute length, is the significant factor influencing the stress fields at the crack tip and at the corner notch. The length of the daughter crack merely determinates at which radial distance the mode-II stress field is obtained. For the small lengths of the daughter crack, the validity region of the determined crack tip stress fields is very small, of course, and certainly also smaller than the process zone, that would result for practical situations. Conclusions for application relevant problems can, therefore, hardly be derived. The data are nevertheless of interest and significance on fundamental grounds.

Calculation of stress intensity factors and energy release rates

From the stress fields, the stress intensity factors are determined by extrapolation procedures. The results are given in Table 1. Furthermore, the energy release rate is calculated for different lengths of the daughter crack by means of the virtual crack closure integral approach, see [8]. These data are also given in the table and additionally graphically displayed in Fig. 5. The two components of K and G for the daughter crack in mode-I and mode-II are reported. For the strain energy release rate, additionally, the total energy release rate, $G_{Tot,D}$ is given. Since G_{ID} is practically zero, $G_{IID} \approx G_{Tot,D}$. Figure 5b shows a detailed representation of Fig. 5a in the region of very small crack lengths.

Table 1: Stress intensity factors, K , and energy release rates, G , for different lengths of the daughter crack normalized to the corresponding data of the mother crack.

	MOTHER CRACK	DAUGHTER CRACK of length a_D [mm]				
		10^{-6}	10^{-3}	10^{-2}	10^{-1}	1
K_I/K_{IIM}	0.1301	1.1508	1.1603	1.1607	1.1701	1.2673
K_{II}/K_{IIM}	1.	0.1073	0.1084	0.1032	0.0932	0.0161
G_I/G_{IIM}	0.01691	1.3150	1.3248	1.3262	1.3466	1.5805
G_{II}/G_{IIM}	1.	0.0117	0.0114	0.0106	8.755 E-3	3.513 E-4
G_{Tot}/G_{IIM}	1.0169	1.3267	1.3362	1.3368	1.3553	1.6174

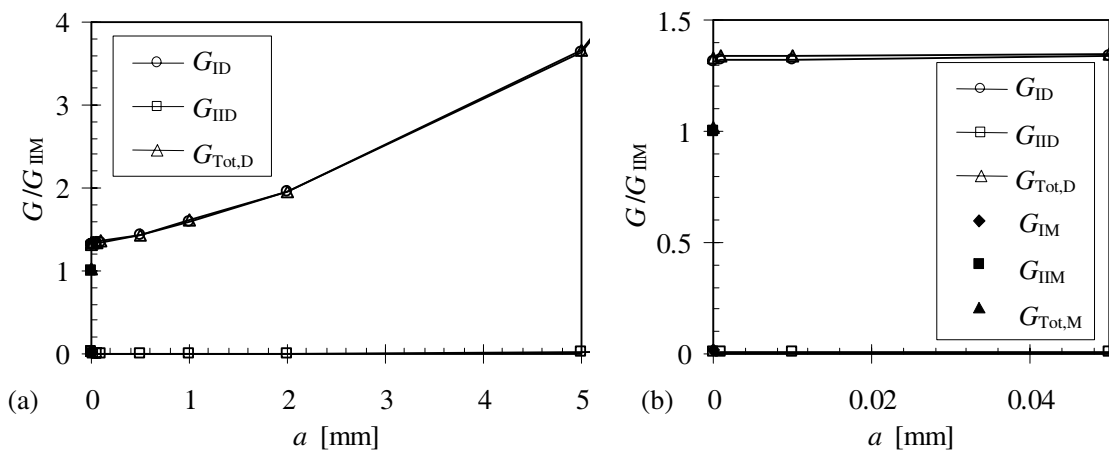


Fig. 5: Energy release rate as a function of the length of the daughter crack: a) general results, b) detail for very small crack lengths.

The results for K and G show a jump in the transition from the mother crack to the daughter crack (for small crack lengths directly after initiation). Thus, excess energy will be at disposal after the daughter crack has initiated. This excess energy results in a faster propagation of the daughter crack compared to a crack that had been initiated from a mode-I loaded mother crack with $(K_I = K_{II})_M$. Such a behaviour has experimentally been observed in [7]. The stress intensity factors and the energy release rates calculated for the daughter crack of different lengths do not show large variations in their value as soon as the daughter crack exists and the crack length is small. For larger cracks, larger strain energy release rates are obtained as a consequence of the increasing effective crack length.

Conclusions

From the reported results it can be concluded:

The BEM is a suitable method to perform numerical calculations for complex problems in fracture mechanics as those related to mode-II or mixed mode loaded cracks for which failure is associated with both a change in the type of the stress singularity and an increase in the number of the stress singularities involved. This is demonstrated for the transition of a shear mode-II singularity of a mother crack into the mode-I singularity around the daughter crack tip and a compression singularity around the corner notch. Both stress fields are of symmetric nature although loading and crack geometry are not symmetric.

The calculations have shown that the mode-I stress field around the tip of the daughter crack builds up as a consequence of the existence of the daughter crack, independently of its length. It must be recognized, though, that the K_I dominated region is arbitrarily small.

The high spatial resolution of the BEM was the essential prerequisite for performing the study as reported.

References

- [1] P.Morales, A.Blázquez, D.Fernández., J.F.Kalthoff *Investigation of the suitability of a test method for determining mode-II fracture toughnesses using boundary element analysis*, Advances in Boundary Element Techniques IV, Gallego and Aliabadi Eds. (2003).
- [2] F.París and J.Cañas *Boundary Element Method*, Oxford Univ. Press (1997).
- [3] A.Blázquez, V.Mantič, F.París and J.Cañas *On the removal of rigid body motions in the solution of elastostatic problems by direct BEM*, Int. J. for Numerical Methods in Engng., **39**, 23, 4021-4038 (1996).
- [4] A.Blázquez, V.Mantič, F.París and J.Cañas *BEM solutions of contact problems by weak application of contact conditions with non-conforming discretizations*, Int. J. of Solids and Structures, **35**, 24, 3259-3278 (1998).
- [5] M.L.Williams *Stress singularities resulting from various boundary conditions in angular corners of plates in extension*, Journal of Applied Mechanics, Trans. ASME, Dec., 526-528 (1952).
- [6] M.F.Kanninen and C.H.Popelar *Advanced Fracture Mechanics*, Oxford University Press (1985).
- [7] R.Podleschny and J.F.Kalthoff *A novel mode-II fracture criterion*, 10th Biennial Conference on Fracture, ECF 10, Berlin, pp. 211-221 (1994).
- [8] E.F.Rybicki and M.F.Kanninen *A finite element calculation of stress intensity factors by a modified crack closure integral*, Engineering Fracture Mechanics, **9**, 931-938 (1977).

A BEM formulation for damage by the Dual Reciprocity approach

V. Mallardo¹, M.H. Aliabadi²

¹ Department of Architecture, via Quartieri 8, 44100 Italy – mlv@unife.it

² Department of Engineering, Queen Mary, University of London, Mile End, London, E14NS, UK – M.H.Aliabadi@qmul.ac.uk

Keywords: Damage, DRBEM.

Abstract. The Dual Reciprocity Method was introduced to avoid the time consuming evaluation of the domain integrals involved for elastostatics with body forces and for elastodynamic problems. The procedure was then extended to diffusion problems and plasticity. The method is essentially a generalised way of constructing particular solutions that can give rise to integral formulations without involving domain integrals. In the present paper, the Dual Reciprocity approach is used to solve the boundary integral equations involved in damage mechanics. The paper is divided mainly into two parts. The first part introduces the damage model examined. An analytical solution is obtained in order to check the numerical procedure. The second part presents the application of the Dual Reciprocity Boundary Element Method (DRBEM) to the damage model previously described. The expression of the particular displacement, strain and stress are obtained by the Galerkin vector approach and by introducing a suitable global shape function. Finally, some numerical results are presented in order to assess the efficiency of the method.

Introduction

The need for only surface discretisation is a significant advantage of the BEM over other methods requiring full domain discretisation. However, this advantage is partially reduced in the nonlinear problems where the nonlinearity is related to the behaviour of the material. In such situations a volume integration is required. In this paper, a Dual Reciprocity approach is proposed in damage analysis in order to incorporate the nonlinear effects without the need for volume integration. The method is based on the determination of a particular solution which allows the domain integral to be transformed into the sum of boundary integrals.

The state of the art up to 1990 of the DRBEM is summarised in [1] where the method is fully investigated both for the partial differential equations in which the derivative term is of Laplace type and for elasticity with different type of body forces. In [2] the use of particular integrals in the BEM (strictly equivalent to the DRBEM) is developed for two- and three-dimensional elastoplastic stress analysis. The formulation is implemented in a multi-region system by using quadratic isoparametric boundary elements to model the geometry and the field variables of the surface. A particular integral for displacements, strain and stress rates is obtained in terms of a suitable representation of the initial stress. A boundary-only integral representation is obtained and used in a classical iterative procedure. In [3] some radial basis functions for the BEM and related algorithms, such as the method of fundamental solutions, are investigated. Convergence and efficiency are discussed with reference to some new particular solutions for Poisson and Helmholtz-type operators and some suggestions for future applications are given. No analyses are given for physically nonlinear problems.

The present paper intends to deal with the application of the DRBEM to the damage model initially proposed by Kachanov and then developed by [4]. The governing relations, the state laws and the flaw laws of the model are shortly described; then, the boundary-only integral equations are written by obtaining a particular solution of the elasto-damaged problem. Numerical results are shown both in the presence of an analytical solution and in a more general situation.

The damage model

Damage may be interpreted as a progressive physical process by which some history – dependent materials irreversibly degenerate under mechanical loads. The mechanics of damage is the study, through mechanical variables, of the mechanisms involved in this deterioration when the materials are subjected to loading. Damage process may be interpreted as the creation of microspheres of discontinuities which grow, coalesce and eventually lead to the rupture.

An additional damage variable d is introduced into the constitutive equations in order to describe that portion of partly damaged body which is still able to carry some load. Such a variable can be interpreted as the ratio between the effective area including cracks and the area of the undamaged solid. The damage is assumed to be isotropic. The formulation is confined to the case of small induced strains.

A thermodynamically consistent damage formulation can be easily obtained following [5]:

$$\boldsymbol{\sigma} = f(d)\mathbf{C}^e : \boldsymbol{\varepsilon} \quad (1a)$$

$$Y := -\frac{1}{2} \frac{\partial f(d)}{\partial d} \boldsymbol{\varepsilon} : \mathbf{C}^e : \boldsymbol{\varepsilon} \quad (1b)$$

$$\chi := h\xi \quad (1c)$$

$f(d)$ is a scalar function (linear or quadratic) of the damage, \mathbf{C}^e is the elastic tensor, ξ is a scalar kinematic internal variable which describes the damage hardening state, Y and χ are the thermodynamic forces conjugate to d and ξ respectively.

The existence of a damage activation function $\phi(Y, \chi)$ can be assumed:

$$\phi(Y, \chi) = Y - Y_0 - \chi = Y - Y_0 - h\xi \leq 0 \quad \dot{\lambda} \geq 0 \quad \dot{\lambda} \phi = 0 \quad \text{in } \Omega \quad (2)$$

where $\dot{\lambda}$ is the damage multiplier and h represents a damage hardening modulus. Under the hypothesis of generalised associative damage behaviour the flaw laws read:

$$\dot{d} = \frac{\partial \phi}{\partial Y} \dot{\lambda} = \dot{\lambda}, \quad \dot{\xi} = -\frac{\partial \phi}{\partial \chi} \dot{\lambda} = \dot{\lambda} \quad \text{in } \Omega \quad (3)$$

Let an assigned strain rate field $\dot{\boldsymbol{\varepsilon}}(\mathbf{x})$ be given. If Ω_d is the part of the body which is damaged, the response at \mathbf{x} is locally elastic if $\mathbf{x} \notin \Omega_d$, whereas at the points $\mathbf{x} \in \Omega_d$ the response is elastic-damaging and the following relations must hold:

$$\dot{\phi}(Y, \chi) \leq 0 \quad \dot{d} = \dot{\xi} = \dot{\lambda} \geq 0 \quad \dot{\phi} \dot{\lambda}_d = 0 \quad \text{in } \Omega_d \quad (4)$$

After expanding both the rate form of the damage activation function and the rate form of Y , the complete incremental damage problem can be stated as follows:

$$\dot{\phi}(Y, \chi) = -\frac{1}{2} \frac{\partial^2 f(d)}{\partial d^2} \boldsymbol{\varepsilon} : \mathbf{C}^e : \boldsymbol{\varepsilon} \dot{d} - \frac{\partial f(d)}{\partial d} \boldsymbol{\varepsilon} : \mathbf{C}^e : \dot{\boldsymbol{\varepsilon}} - h\dot{\xi} \leq 0 \quad (5a)$$

$$\dot{\lambda} = \dot{d} = \dot{\xi} \quad \dot{\phi} \dot{\lambda} = 0 \quad \text{in } \Omega_d \quad (5b)$$

An analytical solution can be obtained in the plane stress case of rectangular (base B and height H) plate subjected to a uniform vertical displacement on the top line and constrained to zero vertical displacement on the base. The horizontal displacement is free. Due to the simplicity of the load, the solution depends only on the longitudinal variables. The imposed displacement can be incremented in linear way:

$$u(t) = \frac{\bar{u}}{t} t \quad t \in [0, \bar{t}] \quad (6)$$

Consequently, the longitudinal strain and the strain energy can be written as:

$$\varepsilon(t) = \frac{\bar{u}}{Ht} t \quad Y(t) = \frac{1}{2} E \left(\frac{\bar{u}}{Ht} \right)^2 t^2 \quad t \in [0, \bar{t}] \quad (7)$$

where E indicates Young's modulus. The value of $t = t_0$ in which the nonlinear process starts can be easily obtained:

$$\varepsilon(t_0) = \sqrt{\frac{2Y_0}{E}} \Rightarrow t_0 = \frac{H\bar{t}}{u} \sqrt{\frac{2Y_0}{E}} \quad (8)$$

Finally, the expression of the damage parameter in the generic "instant" t can be obtained by imposing the rate form (5a) of the damage activation function to be zero:

$$\dot{d}(t) = \frac{\dot{Y}}{h} \Rightarrow d(t) = \frac{1}{h} \int_{t_0}^t \dot{Y} dt = \frac{E}{2h} \left(\frac{\bar{u}}{Ht} \right)^2 (t^2 - t_0^2) \quad (9)$$

The stress rate is consequently given by:

$$\dot{\sigma}(t) = \left[1 - \frac{E}{2h} \left(\frac{\bar{u}}{Ht} \right)^2 (t^2 - t_0^2) \right] E \frac{\bar{u}}{Ht} t \quad (10)$$

The DRBEM in damage

The application of the DRBEM to the above elasto-damaged problem can be performed by following a procedure similar to [2]. The displacement boundary integral equation and the expression of the stress in any internal point can be written as in plasticity but using for the nonlinear stress the following expression:

$$\sigma = f(d) \mathbf{C}^e : \varepsilon = \mathbf{C}^e : \varepsilon - \sigma^d = \sigma^{el} - \sigma^d \quad (11)$$

where the ij^{th} term of σ^d is given by :

$$\sigma_{ij}^d = 2\mu \left[(1 - f(d)) \varepsilon_{ij} + \frac{\nu}{1 - 2\nu} \varepsilon_{kk} \delta_{ij} \right] \quad (12)$$

Therefore, the governing inhomogeneous differential equation for incremental elasto-damage can be expressed in terms of incremental displacement as:

$$\mu \dot{u}_{i,jj} + \frac{\mu}{1 - 2\nu} \dot{u}_{j,ji} = \dot{\sigma}_{ij,j}^d \quad (13)$$

If a particular solution \dot{u}_j^p of the above differential equation is found, then both the displacement integral equation and the stress in any interior point can be expressed only in terms of boundary quantities:

$$\begin{aligned} c_{ij}(\xi) \dot{u}_j(\xi) + \int_{\Gamma} t_{ij}^*(\xi, \mathbf{x}) \dot{u}_j(\mathbf{x}) d\Gamma(\mathbf{x}) - \int_{\Gamma} u_{ij}^*(\xi, \mathbf{x}) \dot{t}_j(\mathbf{x}) d\Gamma(\mathbf{x}) = \\ = c_{ij}(\xi) \dot{u}_j^p(\xi) + \int_{\Gamma} t_{ij}^*(\xi, \mathbf{x}) \dot{u}_j^p(\mathbf{x}) d\Gamma(\mathbf{x}) - \int_{\Gamma} u_{ij}^*(\xi, \mathbf{x}) \dot{t}_j^p(\mathbf{x}) d\Gamma(\mathbf{x}) \end{aligned} \quad (14)$$

$$\begin{aligned} \dot{\sigma}_{ij}(\mathbf{X}) + \int_{\Gamma} T_{ijk}^*(\mathbf{X}, \mathbf{x}) \dot{u}_k(\mathbf{x}) d\Gamma(\mathbf{x}) - \int_{\Gamma} U_{ijk}^*(\mathbf{X}, \mathbf{x}) \dot{i}_k(\mathbf{x}) d\Gamma(\mathbf{x}) = \\ \dot{\sigma}_{ij}^p(\mathbf{X}) + \int_{\Gamma} T_{ijk}^*(\mathbf{X}, \mathbf{x}) \dot{u}_k^p(\mathbf{x}) d\Gamma(\mathbf{x}) - \int_{\Gamma} U_{ijk}^*(\mathbf{X}, \mathbf{x}) \dot{i}_k^p(\mathbf{x}) d\Gamma(\mathbf{x}) \end{aligned} \quad (15)$$

The fundamental solutions can be read for instance in [6].

The problem is now the determination of a particular integral of (13). Its expression is obtained by the Galerkin vector approach:

$$\dot{u}_j^p = \frac{1-\nu}{\mu} \dot{F}_{i,kk} - \frac{1}{2\mu} \dot{F}_{k,ki} \quad \dot{F}_{i,jkk} = \frac{\sigma_{ij,j}^d}{1-\nu}, \quad (16)$$

by introducing a second order tensor such that:

$$\dot{h}_{ij,mmmm} = \dot{\sigma}_{ij}^d \quad (17)$$

and by representing this tensor by means of an infinite series in terms of a suitable global shape function $C(\mathbf{x}, \xi_n)$ and a fictitious density tensor $\dot{\phi}_{lm}(\xi)$:

$$\dot{h}_{lm}(x) = \sum_{n=1}^{\infty} C(\mathbf{x}, \xi_n) \dot{\phi}_{lm}(\xi_n) \quad \text{where } C(\mathbf{x}, \xi_n) = r^4 - r^5 \quad (18)$$

Substituting (18) into (17) and the resulting relation into (16), the final expression of the particular displacement is obtained:

$$\dot{u}_i^p = \sum_{n=1}^{\infty} \left[\frac{1}{\mu} C_{,mkk} \delta_{il} - \frac{1}{2\mu(1-\nu)} C_{,ilm} \right] \dot{\phi}_{lm} = \sum_{n=1}^{\infty} D_{ilm}(x, \xi_n) \dot{\phi}_{lm}(\xi_n) \quad (19)$$

and, consequently, the related strain, stress and traction can be written as:

$$\dot{\varepsilon}_{ij}^p = \sum_{n=1}^{\infty} E_{ijlm}(x, \xi_n) \dot{\phi}_{lm}(\xi_n) \quad (20)$$

$$\dot{\sigma}_{ij}^p = \sum_{n=1}^{\infty} S_{ijlm}(x, \xi_n) \dot{\phi}_{lm}(\xi_n) \quad \dot{i}_{ij}^p = \dot{\sigma}_{ij}^p n_j \quad (21)$$

The kernes are given in [2].

For the numerical purpose, the infinite series representations are truncated at a finite number of N terms. The choice of N is dictated by the complexity of the problem. In the proposed numerical applications fictitious points ξ_n are introduced at all boundary collocation nodes and additional points are possibly added in the interior. At every iteration, the vector $\dot{\phi}_{lm}$ is evaluated by solving the following system of equations:

$$\dot{\sigma}_{ij}^d(x) = \sum_{n=1}^N C_{,ppqq}(\mathbf{x}, \xi_n) \dot{\phi}_{ij}(\xi_n) \quad (22)$$

and by computing the damaged stress in the N boundary/internal points.

The final system of equations is solved by coupling the DRBEM with the arclength methods in order to pass critical limit points. The procedure is performed by following the steps given in [7]. If the classical nonlinear procedure is applied, the spatial discretisation of the equations (14-15) is performed by discretising the boundary of the body with continuous quadratic elements and the part of the domain in which the damage is expected with quadratic internal cells,.

Numerical analyses

All the numerical examples presented refer to a rectangular plate $1000 \times 1250 \text{ mm}^2$ in plane stress and loaded on the horizontal top line by a uniform load p . The following values are used for the material properties: $E = 20000 \text{ N/mm}^2$, $\nu = 0.30$, $Y_0 = 1.0E - 04 \text{ N/mm}^2$ and $h = 8.0E - 04 \text{ N/mm}^2$. The initial internal mesh necessary to evaluate the domain integral involved in the classical iterative nonlinear analysis consists of 6×8 cells. Figure 1 shows the boundary conditions and the three different distributions of internal points possibly required by the DRBEM procedure.

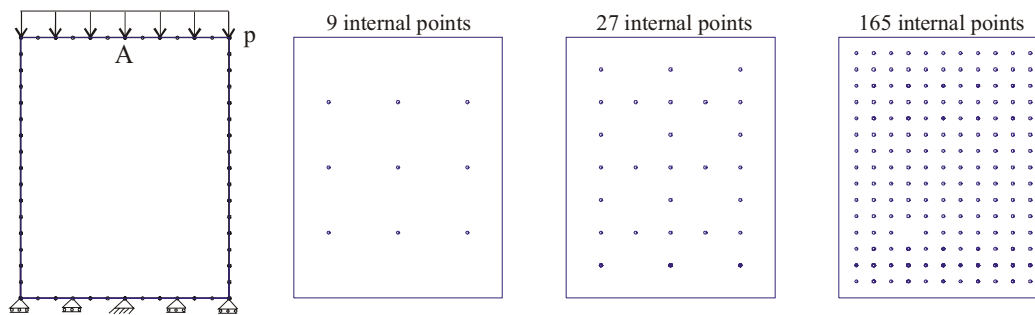


Fig. 1 – Boundary conditions, boundary discretisation and internal points for the DRBEM

The load-displacement diagrams presented describe graphically the relationship between the vertical displacement of the point A of figure 1 and the load factor λ given by the ratio between the load reached at the instant t and $p = 2.0 \text{ N/mm}^2$.

The first example has the purpose to check the accuracy of the proposed procedure by comparing the numerical results with the analytical ones previously obtained in the case of linear damage. Figure 2 shows that the DRBEM employed with only boundary points is able to follow the analytical solution with an error less than 3%.

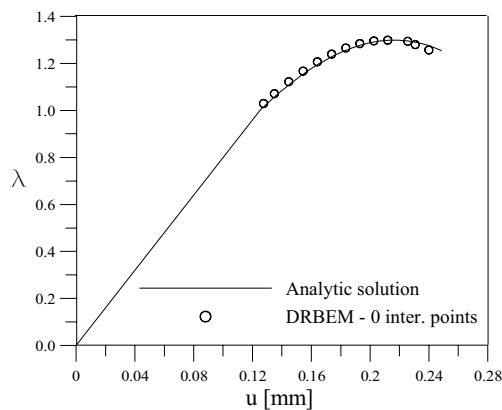


Fig. 2 – Comparison of the DRBEM with the analytical solution

The second example considers the rectangular plate shown in figure 1 in the case of quadratic damage; the initial value of Y_0 in the domain cell of the bottom-left corner of the plate is taken 10% lower than the corresponding value in the remaining domain cells. The comparison between the DRBEM and the conventional Boundary Element procedure for physically nonlinear problems involving domain integrals is shown in figure 3. The boundary points are always 56, whereas the internal points added can be 0, 9 and 165.

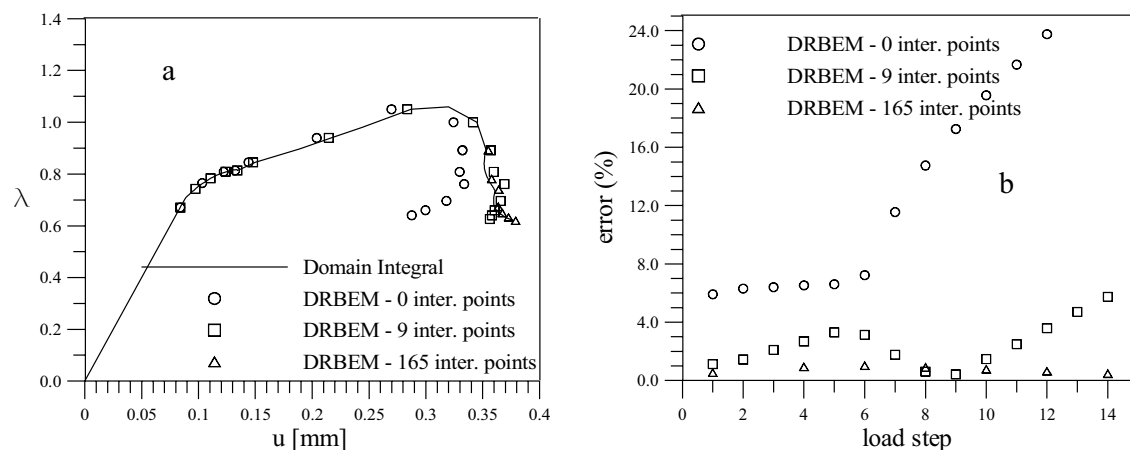


Fig. 3 – DRBEM and domain integrals procedure. Comparison and error analysis

Figure 3a shows that some internal points are necessary in order to improve the solution in the softening branch. Figure 3b analyses the error obtained by comparing the DRBEM solution with the domain integral procedure for the load steps involved in the softening branch (load step=1 corresponds to the peak point). It must be underlined that the numerical results in the softening path may be influenced by the constitutive instability of the model and they could be improved if a regularisation technique were used.

Summary

A nonlinear Dual Reciprocity Boundary Element procedure has been proposed for a damage model. It is based on the determination of a particular integral of the elasto-damaged differential equation. An analytical solution is also obtained in a simple case in order to check the numerical results. The numerical examples show that the procedure is efficient and robust. Future work will be aimed at implementing the Dual Reciprocity approach for a nonlocal damage model. The nonlocal regularisation technique is one of the possibilities to avoid the theoretical and numerical difficulties originated by constitutive instability matters related to the model.

References

- [1] P.W. Partridge, C.A. Brebbia, L.C. Wrobel *The dual reciprocity boundary element method*, CMP (1992).
- [2] D.P. Henry, P.K. Banerjee *International Journal for Numerical Methods in Engineering*, **26**, 2079-2096, (1988).
- [3] M.A. Golberg, C.S. Chen, H. Bowman *Engineering Analysis with Boundary Elements*, **23**, 285-296, (1999).
- [4] J.A. Lemaitre *A Course on Damage Mechanics*, Springer-Verlag (1992).
- [5] G. Borino, B. Failla, F. Parrinello *International Journal of Solids and Structures* **40**, 3621-3645, (2003)
- [6] M.H. Aliabadi *The Boundary Element Method, Vol2: Applications in Solids and Structures*, Wiley (2002).
- [7] V. Mallardo, C. Alessandri *Engineering Analysis with Boundary Elements*, **28**(6), 547-559, (2004).

Analysis of localization and regularization techniques using boundary elements

Alexandre S. Botta¹, Wilson S. Venturini¹ and Ahmed Benallal²

¹São Carlos School of Engineering, University of São Paulo, Av. Trabalhador São-carlense, 400, 13566-590 – São Carlos, Brazil, venturin@sc.usp.br

²Laboratoire de Mécanique et Technologie, ENS de Cachan/CNRS/Un. Paris 6, 61 Avenue du President Wilson, 94235, Cachan, France, ahmed.benallal@lmt.ens-cachan.fr

Keywords: boundary elements, damage mechanics, tangent operator, implicit formulation, regularization techniques.

Abstract. In this work, a BEM formulation is proposed to deal with solids with reduced rigidity due to a damage process. The formulation is similar to the one developed in the context of plasticity analysis. The BEM algebraic equations are obtained either using displacement or traction equations, for the boundary nodes, and stress (or strain) equations for the internal nodes. The regularization model adopted is based on weighting the strain field over the domain or part of it. Arc-length strategy is adapted to deal with this case of strong non-linear problems, particularly to analyse problems exhibiting the snap-back effects. The consistent tangent operators have been derived for local and non-local BEM approaches.

Introduction

The Boundary Element Method (BEM) is nowadays a useful and reliable numerical tool to solve many practical engineering applications. As a rule the BEM procedures formulated so far lead to accurate and stable solutions. Analysis of non-linear problems by means of BEM can be found since the end of seventies (see Brebbia et. al., 1984). The non-linear formulations used during a quite long time were all based on the initial stress and strain procedures, for which constant matrix schemes are employed.

More recently, the concept of Consistent Tangent Operator – CTO, due to Simó [2] has been adapted to BEM non-linear formulations as shown in some recent works [3,4,5]. The same concept has also been adopted to deal with gradient plasticity problems via BEM [6], where an implicit formulation has been successfully implemented to obtain quite accurate plastic regularized solutions.

Modelling the mechanical behaviour of brittle material structures is nowadays another important and interesting theme that has attracted the attentions of several well-known laboratories. Damage mechanics is a very interesting model to represent very well materials in this context, particularly materials that exhibit behaviour characterized by the formation of micro-cracks resulting into losses of strength and rigidity of the structural members [7,8].

Although material models based on damage mechanics is nowadays a reliable and very appropriate to express the proper material behaviour particularly to represent the serviceability conditions, for which the actual definition to the deteriorated stiffness is very important, only few works based on non-linear BEM formulations have already appeared in this context so far [9,10,11,12].

In this work, the implicit non-linear BEM formulation is extended to solids governed by damage models. First, the boundary algebraic equations are derived and then transformed appropriately to give an incremental solution scheme with tangent predictor. A non-local BEM formulation, based on the non-local integral concept [13]Pijaudier-Cabot & Bazant] is also adopted to avoid mesh dependency. The arc-length technique to deal with this highly non-linear problems, characterized by exhibiting zone with almost no rigidity is also implemented together with the implicit BEM formulation to capture solutions exhibiting snap-back effects. Numerical examples are solved to demonstrate the accuracy and stability of the developed model particularly when dealing with that complex problem.

Damage Mechanics Models

The damage mechanics model chosen to be incorporated in the non-linear BEM formulation is isotropic and particularly proposed to deal with concrete materials [14]. The behaviours in tension and

in compression are assumed to be represented by damage scalar variables D_t and D_c , respectively, leading to two functions f_t and f_c , to specify the elastic zone limit.

The free energy potential is considered for this model is:

$$\psi = \frac{1}{2} \{ 2\mu_0(1-D_t)(1-D_c)\mathbf{e} : \mathbf{e} + K_0(1-D_t)(tr^+\boldsymbol{\varepsilon})^2 + K_0(1-D_c)(tr^-\boldsymbol{\varepsilon})^2 \} \quad (1)$$

where $\boldsymbol{\varepsilon}$ and \mathbf{e} are the strain tensor and its deviatoric part, respectively, while μ_0 and K_0 are the shear and bulk moduli; $tr^+\boldsymbol{\varepsilon} = \langle tr\boldsymbol{\varepsilon} \rangle$ and $tr^-\boldsymbol{\varepsilon} = -\langle -tr\boldsymbol{\varepsilon} \rangle$ are positive and negative parts of the volumetric strain.

The stress tensor, derived from eq (1), reads

$$\boldsymbol{\sigma} = \partial\psi / \partial\boldsymbol{\varepsilon} = 2\mu\mathbf{e} + K_+tr^+\boldsymbol{\varepsilon}\mathbf{I} + K_-tr^-\boldsymbol{\varepsilon}\mathbf{I} \quad (2)$$

being \mathbf{I} the second order identity tensor, $\mu = \mu_0(1-D_t)(1-D_c)$, $K_+ = K_0(1-D_t)$ and $K_- = K_0(1-D_c)$.

Then, loading functions f_t and f_c can be defined as follows:

$$f_t = J_2 - a_t I_1^2 + b_t r_t(D_t) I_1 - k_t r_t^2(D_t) (1 - \alpha D_c) \quad (3a)$$

$$f_c = J_2 + a_c I_1^2 + b_c r_c(D_c) I_1 - k_c r_c^2(D_c) \quad (3b)$$

where $r_i(D_i)$, for $i = t, c$, is given by:

$$r_i(D_i) = 1 - [1 - (\sigma_c / \sigma_0)_i] [D_{0i} - D_i]^2 / D_{0i}^2 \quad \text{for } D_i < D_{0i} \quad (4a)$$

$$r_i(D_i) = [1 - ((D_{0i} - D_i)^2 / (1 - D_{0i}^2))^{0.75}] \quad \text{for } D_i \geq D_{0i} \quad (4a)$$

and the Kuhn-Tucker conditions and consistency condition, written for the tensile and compressive parts are given by:

$$f_t \leq 0, \quad \dot{D}_t \geq 0, \quad f_t \dot{D}_t = 0 \quad \text{and} \quad f_c \leq 0, \quad \dot{D}_c \geq 0, \quad f_c \dot{D}_c = 0 \quad (5a)$$

$$\dot{f}_t = 0 \quad \text{and} \quad \dot{f}_c = 0 \quad (5b)$$

For the non-local model the following values have to be weighted over the domain [13]:

$$\langle J_\varepsilon \rangle = \int_\Omega W J_\varepsilon d\Omega \quad \langle tr^+\boldsymbol{\varepsilon} \rangle = \int_\Omega W tr^+\boldsymbol{\varepsilon} d\Omega \quad \langle tr^-\boldsymbol{\varepsilon} \rangle = \int_\Omega W tr^-\boldsymbol{\varepsilon} d\Omega \quad (6a,b,c)$$

where J_ε is the second invariant of deviatoric tensor obtained from \mathbf{e} and W The weighting function which is given by: $W = \exp(-r^2/2\ell^2)/W_0$, with $W_0 = \int_\Omega \exp(-r^2/2\ell^2) d\Omega$; r is the field points distance and ℓ is the characteristic length of the material.

The non-local model is then obtained by using the weighted values in eqs (3).

Integral and algebraic representations for non-linear BEM

The well-known displacement, stress and tractions integral representations for non-linear problems are given by:

$$c_{ik} \dot{u}_k = \int_\Gamma u_{ik}^* \dot{p}_k d\Gamma - \int_\Gamma p_{ik}^* \dot{u}_k d\Gamma + \int_\Omega u_{ik}^* \dot{b}_k d\Omega + \int_\Omega \varepsilon_{ijk}^* \dot{\sigma}_{im}^D d\Omega \quad (7a)$$

$$\dot{\sigma}_{ij} = \int_\Gamma u_{ijk}^* \dot{p}_k d\Gamma - \int_\Gamma p_{ijk}^* \dot{u}_k d\Gamma + \int_\Omega u_{ijk}^* \dot{b}_k d\Omega + \int_\Omega \varepsilon_{ijmk}^* \dot{\sigma}_{km}^D d\Omega + g_{ij}(\dot{\sigma}_{mk}^D) \quad (7b)$$

$$1/2 \dot{p}_i = \int_\Gamma D_{ik}^* \dot{p}_k d\Gamma - \int_\Gamma S_{ik}^* \dot{u}_k d\Gamma + \int_\Omega D_{ik}^* \dot{b}_k d\Omega + \int_\Omega \varepsilon_{imk}^* \dot{\sigma}_{mk}^D d\Omega + g_k(\dot{\sigma}_{ik}^D) \quad (7c)$$

where u_k and p_k are displacements and the tractions at boundary points, b_k gives the body forces, σ_{ij} and σ_{mk}^D represent true and damaged stress fields, c_{ik} , g_{ij} and g_k are standard free terms, the symbol * indicates Kelvin fundamental values and Ω is the solid domain with boundary Γ ; the dots are used to indicate rates.

The above integral equations are transformed into their algebraic forms. For this, the domain integrals containing the damaged stress field, σ_{mk}^D , was approximated by using linear triangular cells

defined only using domain nodes, avoiding therefore stress values at the boundary. The boundary integrals were approximated by using continuous and discontinuous liner elements. After integrating properly boundary and internal cells, one may find the following algebraic set of equations:

$$[H]\{\dot{u}\} - [G]\{\dot{p}\} - [Q]\{\dot{\sigma}^D\} = 0 \quad (8a)$$

$$\{\dot{\sigma}\} + [H']\{\dot{u}\} - [G']\{\dot{p}\} - [Q']\{\dot{\sigma}^D\} = 0 \quad (8b)$$

$$[\beta]\{\dot{p}\} + [H'']\{\dot{u}\} - [G'']\{\dot{p}\} - [Q'']\{\dot{\sigma}^D\} = 0 \quad (8c)$$

For non-linear problems, Integrating boundary elements and internal cells as accurate as possible is very convenient. For problems, where very large strain components are expected and consequently many iterations are required, the accuracy of the above matrices is an necessary conditions to obtain stable solutions, mainly when the material is quite deteriorated with the stiffness going to nearly zero. The analytical integration along boundary elements and cells is maybe the best alternative to guarantee the accuracy of the algebraic representations. Nevertheless, so far we have implemented a numerical scheme based on variable sub-element definition that has shown for other problems to be as accurate as the analytical scheme [15].

Equations (8) can be written in finite increments, Δu_n , Δp_n and, $\Delta \sigma_n^D$ as usual and then solved. First one has to solve either eq (8a), the singular formulation, or eq (8c), the hyper-singular formulation to have the boundary unknowns written in terms of the correcting vector $\Delta \sigma_n^D$ or in terms of strain increments $\Delta \varepsilon_n$, as follows:

$$\{\Delta X_n\} = \{\Delta M_n\} + [R]\{\Delta \sigma_n^D\} \quad (9)$$

where $\{\Delta X_n\}$ and $\{\Delta M_n\}$ the boundary unknowns and the elastic solution for the time increment Δt_n and $[R]$ gives the correcting vector contributions.

Equation (8b) is also modified properly to express the final stress field in terms of the correcting vector values, as follows,

$$\{\Delta \sigma_n\} - \{\Delta N_n\} - [S]\{\Delta \sigma_n^D\} = 0 \quad (10)$$

where $\{\Delta N_n\}$ is the elastic solution and $[S]$ gives the correcting vector contributions.

Equation (10) contains all required relations to solve the damage problem. Basically, one has to choose a time-marching scheme will be used. As for other numerical approaches there are alternatives possible.

After performing simple values transforms, equilibrium equation (10) can be conveniently written in terms of strain increments given by:

$$\{Y(\Delta \varepsilon_n)\} = -[E]\{\Delta \varepsilon_n\} + \{\Delta N_n\} + [\bar{S}]\{[E]\{\Delta \varepsilon_n\} - \{\Delta \sigma(\Delta \varepsilon_n)\}\} = 0 \quad (11)$$

where $[\bar{S}] = [S] + [I]$ and E is the elastic tensor.

This equation is very accurately solved by applying the Newton-Raphson scheme with consistent tangent operator [16].

BEM arc-length algorithm

Brittle materials often exhibit reduction of rigidity over small and localized regions. In this situation the structure is strongly size dependent and often snap-back effects will appear. The dissipation zone is so reduced that both referenced displacement and the total applied load reduce simultaneously when strains over the dissipation area increasing. In order to capture solution along the snap back branch neither load nor displacement can be adopted as a guide variable for the incremental process. For this case one must use as a guide variable a value based on displacement gradients or equivalent ones. In despite of several possibilities, we have extended the non-linear scheme presented in the previous sections to incorporate the arc-length procedure that is a very elegant way to model the cases of solids exhibiting snap-back effects.

The strategy for this class of methods is to assume as guide variable a certain length (arc) that plays the role of a load increment. It means that the specified increment of the arc is the distance, defined *a priori*, to go along the curve load x displacement from the time t_n to time t_{n+1} . Thus, for a node or a group of nodes both displacements and tractions are unknown values. One has therefore to add to the equilibrium equations the arc-length relation, specifying the arc increment, which is the distance to the next equilibrated position.

For simplicity, but without loosing the generality let us consider eq (9), a given traction, or the resultant of a group of tractions, Δp_{cn} is assumed as a single unknown boundary values, therefore increasing the number of unknown from N to N+1.

$$\{\Delta X_n\} = \{\Delta M_n\} + \{G_c\} \Delta p_{cn} + [R] \{ [E] \{\Delta \varepsilon_n\} - \{\Delta \sigma(\Delta \varepsilon_n)\} \} \quad (12)$$

where $\{G_c\}$ is the vector that gives the Δp_{cn} contributions.

The counterpart value of Δp_{cn} , the displacement Δu_{cn} , belongs to the vector $\{\Delta X_n\}$ and may also represent displacement or group of displacements taken anywhere along the boundary. The single equation taken from eq (12) and representing this boundary value may be expressed by:

$$F_{\Delta u}(\Delta u_{cn}, \Delta p_{cn}, \Delta \varepsilon_n) = -\Delta u_{cn} + \Delta M_n + G_c \Delta p_{cn} + \{R\} \{ [E] \{\Delta \varepsilon_n\} - \{\Delta \sigma(\Delta \varepsilon_n)\} \} = 0 \quad (13)$$

The equilibrium equation (11), now to be modified accordingly, reads:

$$F_{\Delta \varepsilon}(\Delta \varepsilon_n, \Delta p_{cn}) = -[E] \{\Delta \varepsilon_n\} + \{\Delta N_n\} + \{N_c\} \Delta p_{cn} + [\bar{S}] \{ [E] \{\Delta \varepsilon_n\} - \{\Delta \sigma(\Delta \varepsilon_n)\} \} = 0 \quad (14)$$

once again $\{N_c\}$ gives the Δp_{cn} contributions for this equilibrium equation.

An extra value has been assumed unknown, therefore to enforce the increments Δp_{cn} and Δu_{cn} to advance the fixed amount of Δs_n , which is the chord of the arc measure in the space $(\Delta p_{cn}, \Delta u_{cn})$ the following geometric relation is assumed and incorporated into algebraic system of non-linear equations.

$$F_{\Delta s}(\Delta u_{cn}, \Delta p_{cn}) = (\Delta p_{cn})^2 + (\Delta u_{cn})^2 - \Delta s_n^2 = 0 \quad (15)$$

The final non-linear system of equations for the increment Δt_n is now given by coupling non-linear eqs (14), (15) and (16) written in terms of the variables Δu_{cn} , Δp_{cn} and $\Delta \varepsilon_n$, and now can be solved by applying the Newton-Raphson's scheme. An iterative process may be required to achieve the equilibrium. For an time increment, Δt_n , the strain increment is computed by cumulating additive corrections $\delta \varepsilon_n^i$ from an interaction i to the next $i+1$, i.e.,

$$\{\Delta \varepsilon_n^{i+1}\} = \{\Delta \varepsilon_n^i\} + \{\delta \varepsilon_n^i\} \quad (16)$$

Similarly, the controlled displacement and resultant reaction are computed by cumulating additive corrections, as follows,

$$\Delta u_{cn}^{i+1} = \Delta u_{cn}^i + \delta u_{cn}^i \quad (17a)$$

$$\Delta p_{cn}^{i+1} = \Delta p_{cn}^i + \delta p_{cn}^i \quad (17b)$$

The determination of $\delta \varepsilon_n^i$, δu_{cn}^i and δp_{cn}^i is obtained from the linearized form of eqs (13), (14) and (15), considering only the first term of the Taylor's expansion:

$$\begin{bmatrix} [\bar{S}] [E - E_n^{CTO}] - [E] & 0 & N_c \\ \{R\} [E - E_n^{CTO}] & -1 & G_c \\ 0 & 2(\Delta u_c^i) & 2(\Delta p_c^i) \end{bmatrix} \begin{Bmatrix} \delta \Delta \varepsilon_n^i \\ \delta \Delta u_{cn}^i \\ \delta \Delta p_{cn}^i \end{Bmatrix} = \begin{Bmatrix} -F_{\Delta \varepsilon}(\Delta p_{cn}^i, \Delta \varepsilon_n^i) \\ -F_{\Delta u}(\Delta u_{cn}^i, \Delta p_{cn}^i, \Delta \varepsilon_n^i) \\ -F_{\Delta s}(\Delta u_{cn}^i, \Delta p_{cn}^i) \end{Bmatrix} \quad (18)$$

where the algorithmic consistent tangent operator, $E_n^{CTO} = \partial \Delta \sigma_n^i / \partial \Delta \varepsilon_n^i$ is explicited. For the model adopted for this work the consistent tangent operator is obtained from the model expressions given in the section 2. They are also given in the Comi's work [14].

Numerical example

The example presented here consists of carrying out numerically the Brazilian concrete tensile strength test (Figure 1). The compressive damage has been neglected for simplicity. Thus, D_t was the only damage parameter assumed for this analysis. Local and non-local models were adopted to simulate this classical test.

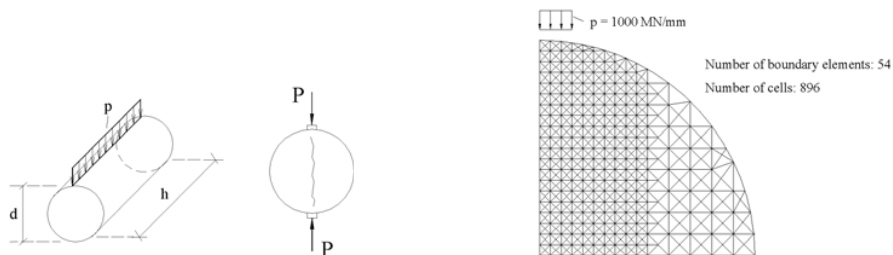


Figure 1. Concrete tensile strength test. Figure 2. discretization of a quarter of the cylinder cross-section.

The parameters chosen to conduct the analysis are: The Young's modulus $E = 31000 \text{ Mpa}$; the Poisson's ratio 0.1 ; cylinder length $h = 30 \text{ cm}$; diameter $d = 15 \text{ cm}$; $a_t = 0.333$; $b_t = 4.0 \text{ Mpa}$; $k_t = 20 \text{ Mpa}^2$; $c_t = 5.0$; $D_{0t} = 0.1$; $(\sigma_c / \sigma_0) = 0.8$; and $\ell_t = 0.1 \text{ cm}$.

The problem is analysed by discretizing only a quarter of the cylindrical cross-section shown in Figure 2. Consequently, vertical and horizontal displacements along the symmetrical axes are assumed equal zero. The guide traction is applied along three upper elements as shown in Figure 1.

The results in terms of vertical displacement-traction resultant computed for the top node are illustrated in Figure 3, while the stresses along the cylinder diameter are depicted in Figure 4.

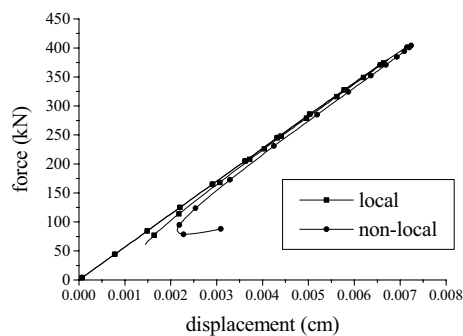


Figure 3. Force-displacement curves for local and non-local models.

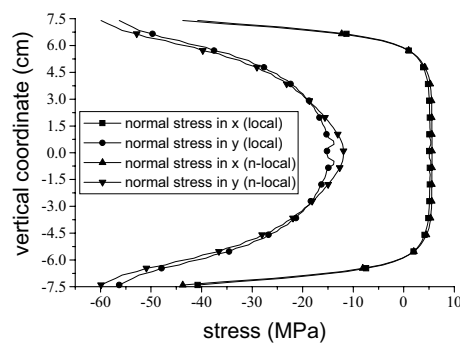


Figure 4. Computed stresses along the cylinder diameter.

Conclusions

The non-linear boundary element formulation has been extended to analyse damage mechanics problems. Accurate integration scheme, the use of consistent tangent matrix and also the implementation of the arc-length scheme for this non-linear BEM formulation was the main points that have guaranteed a stable and accurate solutions for very complex analysis. Several other problems with damage going to nearly the unit have also demonstrated the excellent performance of the algorithm. The damage models used together BEM is particularly appropriate to represent concrete behaviour and able to indicate the crack initiation as verified in the shown numerical experiment.

Acknowledgements:

To FAPESP – São Paulo State Research Foundation for the support given to this work.

References

- [1] C.A.Brebbia, J.C.F.Telles and L.C.Wrobel *Boundary element techniques. Theory and applications in engineering*, Springer-Verlag (1984).
- [2] J.C.Simó and R.L.Taylor *Consistent tangent operators for rate-independent elastoplasticity*. *Comp. Meth. Appl. Mech. Engng*, 48, 101-118 (1985).
- [3] M.Bonnet and S.Mukherjee *Implicit BEM formulation for usual and sensitivity problems in elasto-plasticity using the consistent tangent operator concept*, *International Journal of Solids and Structures*, 33: 4461-4480 (1996).
- [4] H.Poon, S.Mukherjee and M.Bonnet *Numerical implementation of a CTO-based implicit approach for the BEM solution of usual and sensitivity problems in elasto-plasticity*, *Engineering Analysis with Boundary Elements*, 22:257-269 (1998).
- [5] C.A.Fudoli, W.S.Venturini and A.Benallal *BEM Formulations Applied to Gradient Plasticity, Boundary Elements 22, Eds.C.A.Brebbia, & H.Power*, WIT Publ. Southampton (2000).
- [6] A.Benallal, C.A.Fudoli and W.S.Venturini *An Implicit BEM Formulation for Gradient Plasticity and Localization Phenomena*. *Int. J. Numer. Meth. Engng*, 53: 1853-1869 (2002).
- [7] J.Lemaitre, and J.L.Chaboche *Mécanique des matériaux solides*, Dunod, Paris (1985).
- [8] J.Lemaitre *A course on damage mechanics*, Springer-Verlag, Berlin (1992).
- [9] U.Herding and G.Kuhn *A field boundary element formulation for damage mechanics*, *Engineering Analysis with Boundary Elements*, 18: 137-147 (1996).
- [10] R.Garcia, J.Florez-Lopez and M.Cerrolaza *A boundary element formulation for a class of non-local damage models*, *Int. J. Sol. Struct.*, 36: 3617-3638 (1999).
- [11] A.S.Botta and W.S.Venturini and A.Benallal *A BEM implicit formulation applied to damage mechanics models*, Twenty-fourth International Conference on the Boundary Element Method, Sintra – Portugal (2002).
- [12] F.Lin, G.Yan Z.P.Bazant and F.Ding *Nonlocal Strain-softening model of quasi-brittle materials using boundary element method*. *Engineering Analysis with Boundary Elements*, 26: 417-424 (2002).
- [13] G.Pijaudier-Cabot and Z.P.Bazant *Nonlocal damage theory*, *Journal of Engineering Mechanics*, 113: 1512-1533 (1987).
- [14] C.Comi and U.Perego *A bi-dissipative damage model for concrete with applications to dam engineering, Proc. of Eur. Congr. Comp. Meth Appl. Sc Engng - ECCOMAS 2000*, Barcelona, 2000.
- [15] L.G.S.Leite, H.B.Coda and W.S.Venturini *Two-dimensional solids reinforced by thin bars using the boundary element method*, *Eng. An. Bound. Elements*, 27:193-201 (2003).
- [16] A.S. Botta, W.S.Venturini and A.Benallal *BEM applied to damage models with emphasis on the localization and regularization techniques*, 2nd Symposium and fracture and damage mechanics, Foz do Iguaçu, Br, 2003.